Molecular level control of nanoscale composition and morphology: Toward photocatalytic nanocomposites for solar-to-chemical energy conversion of biomass

by

Thanthirige Purnima Anuththara Ruberu

A dissertation submitted to the graduate faculty

in partial fulfillment of the requirements for the degree of

DOCTOR OF PHILOSOPHY

Major: Chemistry

Program of Study Committee:
Javier Vela, Major Professor
Gordon Miller
Keith Woo
Aaron Sadow
Ning Fang

Iowa State University
Ames, Iowa
2013

ProQuest LLC.
789 East Eisenhower Parkway
P.O. Box 1346
Ann Arbor, MI 48106 - 1346

TABLE OF CONTENTS

ACKNOWLEDGEMENTS

First, I would like thank my advisor Javier Vela for his encouragement, guidance, and support during the past four years. He has been an outstanding mentor and positive influence on both my professional and personal life. I would also like to thank Professor Gordon Miller not only for serving on my committee, but also for being my mentor for Preparing Future Faculty (PFF) program and giving me invaluable advice. Thank you to Professors Keith Woo, Aaron Sadow, and Ning Fang for serving on my Program of Study Committee and being wonderful teachers in and out of the classroom.

I would also like to thank my incredible group members. My time in the lab would not have been such a joyful one if not for my supportive and kind team mates. I owe a special thank you to Yijun Guo for being a wonderful travel partner for conferences and also for not complaining about accompanying me for excruciating exercise sessions. Also, I owe a big thank you to Michelle Thompson, Malinda Reichert and Pat Dilsaver for helping me with language issues. I also had opportunity of working with many undergraduate students. Especially, I would like to thank Rachel Abraham for her hard work in the lab.

I consider myself very fortunate to work with a number of wonderful collaborators during my research. I would like to thank Professor Ning Fang for giving me the opportunity of working with his group on CdS-Au hybrid nanostructures and Dr. Hua-jun Fan for doing computational calculation for molecular control project.

Finally, I would like to thank my family for their limitless love and support. A special thank you goes to my husband Chamara for releasing me from housewife's duties and sacrificing four years of his career for my education. My parents are the best supporters of

my career and I am very grateful to them for believing in me and supporting me in this entire journey.

ABSTRACT

Understanding the factors influencing nanocrystal formation is a challenge yet to be realized. In comparison to the large number of studies on nanocrystal synthesis and their applications, the number of studies on the effect of the precursor chemistry on nanocrystal composition and shape remains low. Although photochemical fabrication of metal-semiconductor nano-heterostructures is reported in literature, control over the free particle formation and the site of metal deposition have not been achieved. Moreover, utilization of metal- semiconductor nano-heterostructures in photocatalytic reactions other than water splitting is hardly explored. In this thesis, we studied the effect of chalcogenide precursor reactivity on the composition, morphology and the axial anisotropy of cadmium-chalcogenide nanocrystals. We also investigated the influence of the irradiation wavelength in synthesizing metal-semiconductor nano-heterostructures. Finally, we showed that metal semiconductor nano-heterostructures can be used as a photocatalyst for alcohol dehydrogenation reactions.

We explored the pathways for the formation of Pt and Pd nanoparticles on CdS and $CdS_{0.4}Se_{0.6}$ nanorods. This study revealed that the wavelength of irradiation is critical to control free-standing vs. bound metal (Pt and Pd) nanoparticles to semiconductor. Additionally, we observed that metal photodeposition occurs on specific segments of axially anisotropic, compositionally graded $CdS_{0.4}Se_{0.6}$ nanorods due to the band-gap differential between their nano-domains. We used semiconductor-metal heterostructures for sunlight-driven dehydrogenation and hydrogenolysis of benzyl alcohol. Heterostructure composition dictates activity (turnovers) and product distribution. A few metal (Pt, Pd) islands on the

semiconductor surface significantly enhance activity and selectivity and also greatly stabilize the semiconductor against photoinduced etching and degradation.

CHAPTER 1

INTRODUCTION

General introduction

This thesis describes progress toward building modular, photocatalytic nanocomposites capable of converting cheap and abundant solar energy into more useful chemical energy. The proposed nanocomposites consist of: a metal nanoparticle fused to a light-harvesting semiconductor nanorod, immobilized in a mesoporous support (figure 1). The semiconductor nanorod absorbs sunlight, including the visible and near-infrared region of the solar spectrum, thus producing electron-hole pairs (excitons). The charge-collecting metal particles extract free electrons from the photoexcited semiconductor, thus achieving charge separation and preventing recombination. The potential energy created by this charge separation is then employed to perform redox reactions in solution-phase. Internalization of the photoactive element inside controlled-polarity pores within mesoporous silica nanoparticles (MSNs) assures that charge transfer (redox) is facile, and prevents self-quenching of charge carriers of the otherwise freely diffusing photoactive elements.

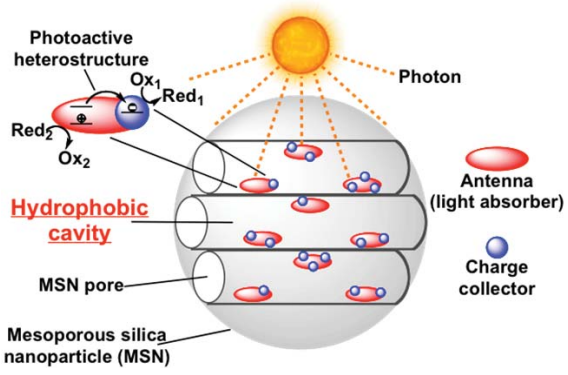

Figure 1. Photocatalytic nano-assembly design.

This thesis specifically describes the two first components of the afore-mentioned photocatalytic design, namely: semiconductor nanorods and surface bound metal nanoparticles.

Semiconductor nanorods

Semiconductor nanocrystals are ideal sunlight harvesters that benefit from: size- and composition-tunable band gaps (300-4000 nm; 4.1-0.3 eV),[1,2,3] broad and intense absorption ($\varepsilon \approx 10^6$ $L \cdot mol^{-1} \cdot cm^{-1}$),[4, 5] long-lived excitons (up to 40 ns for CdSe,[6] 500 ns for $CuInS_2$,[7] 1.8 μs for PbS[8]), good solubility and colloidal stability, and chemical and photo stability.[9] Large aspect ratio semiconductor nanocrystals, often referred to as semiconductor nanorods, are of particular interest in solar energy harvesting because of their ability to form multiple electron-hole pairs (excitons) following photo-excitation.[10, 11] Multiple exciton generation can potentially lead to higher photocatalytic efficiencies than for other morphologies. Therefore, we chose rod-shaped semiconductor nanocrystals as the light harvesting material.

Although spheres are the thermodynamically favored product in many colloidal reactions, highly anisotropic shapes such as rods and wires can be obtained through judicious control of reaction conditions. One way of achieving unidirectional growth is by adjusting precursor (monomer) concentrations. The growth rate of different crystallographic facets also plays a role in determining the final (observed) nanocrystal shape. The growth rate of crystal facets can be influenced by adjusting the types and ratios of organic ligands. [12, 13] For example, in the case of CdSe, it was proposed that alkyl phosphonic acid ligands promote the unidirectional growth along the (001) face of wurtzite crystal structure. However, the effect of chemical structure of the precursor on the final shape of the nanocrystal was not explored prior to our work in this area.

Nanorods lie in between zero-dimensional quantum dots and one-dimentional quantum wires. As a result, the ability to control both the diameter and length of a nanorod is critical in exploring this intermediate shape region. In solar energy conversion devices, unlike with quantum dots, nanorod length can be adjusted to match the device dimensions to facilitate the maximum solar energy absorption.[14] Also, compared to nanowires, nanorods have a greater solubility and are therefore more convenient to utilize for catalysis applications in solution phase.

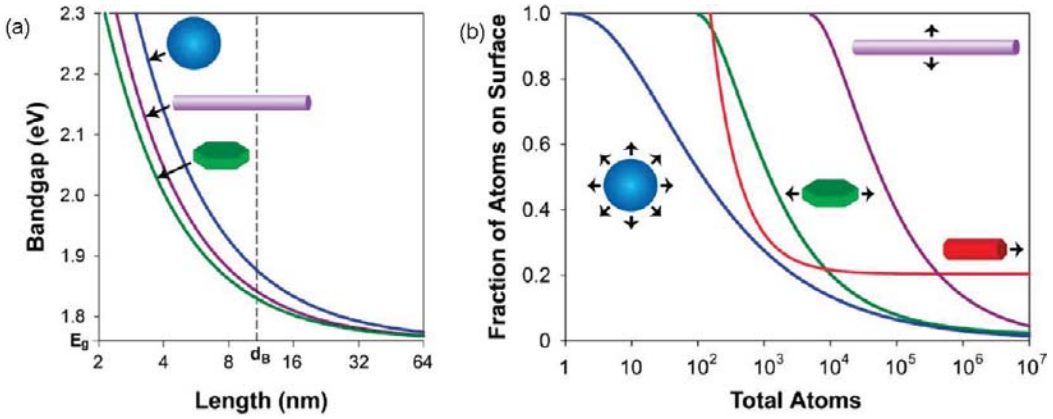

Figure 2: (a) Band gap vs. length in quantum confined dot, wire, and well-shaped nanocrystals (b) The fraction of atoms on the surface for different shapes vs. total number of atoms in a nanocrystal. Reprinted with permission from reference 1. Copyright 2010 American Chemical Society.

In photocatalyst design, properties such as increased solubility, multiple exciton generation, and high surface to volume ratio (figure 2) make semiconductor nanorods superior and more desirable over nanodots or wires. Our initial focus was on CdS nanorods, which have a bulk band gap of 2.4 eV (520 nm). They are easy to prepare by known procedures but their very high aspect ratios leads to poor colloidal stability. In contrast, CdSe nanorods, with a bulk band gap of 1.7 eV (730 nm), are difficult to synthesize in pure form. CdSe nanorods are usually very short (11 nm ± 2 nm) and have low aspect ratios (≈

1.3), although they are very soluble. In this thesis work, we report an intermediate solution to form $CdS_{1-x}Se_x$ nanorods using a mixture of chalcogen precursors.

Recombination of photogenerated charge carriers in the semiconductor directly compete with the photocatalysis process. Among many systems designed to reduce recombination, coupling the semiconductor with a noble-metal nanoparticle has been the most well studied approach. Noble metals facilitate photo-induced charge separation in the semiconductor and help create a low overpotential redox pathway to discharge electrons to the reactants across the particle interface.[15] Therefore, the next part of this thesis work explores the controlled fabrication of metal deposited semiconductor heterostructures.

Metal- Semiconductor heterostructures

Semiconductor heterostructures consist of two or more different materials permanently joined through chemically bonded interfaces. Examples include core/shell and phase segregated multi-component heterostructures made of discrete shaped particles fused via small connecting areas at specific locations.[16]

When a secondary material deposits over a pre-existing substrate of a different material, several factors will decide the growth mode of the heterostructure. If the secondary material exposes lower energy crystal surfaces and/or the lattice mismatch between the two materials is minimum, then the secondary material will deposit in a layer-by-layer fashion, attaining a uniform coverage on the primary substrate, *i.e.* core/shell nanoparticles. Conversely, if the secondary material exposes higher energy crystal surfaces and/or lattice mismatch is high, the secondary material will deposit as separate islands on the primary substrate to minimize the interfacial strain between them, *i.e.* metal-semiconductor heterostructures. The most widely used method to synthesize nanoheterostructures is seeded growth, where ‘seeds’ serve

as the primary substrate centers for accommodating the secondary material upon reaction with the respective molecular precursors. This method agrees with the classical nucleation theory which states that activation energy barrier for heterogeneous nucleation is much lower than that for homogenous nucleation. Moreover, in anisotropic wurtzite cadmium chalcogenide nanorods, polar facets on the tip region are much reactive compared to non-polar facets in the lateral region. This reactivity difference results in nucleation of the second material selectively on the tip region.

Metal-semiconductor nanorod heterostructures are considered one of the important classes of heterostructures due to their interesting photocatalytic properties.[17, 18] Specifically, II-VI semiconductor nanorods decorated with noble metals are investigated as photocatalysts because of their distinctive properties such as visible region absorption, high extinction coefficients, convenient processability, fast electron transfer rates, and slow electron-hole recombination rates.

Metal semiconductor nanorods are synthesized using thermal as well as photochemical methods. Banin and co-workers demonstrated the first example of thermal deposition of Au on CdS and CdSe nanorods.[19] The general synthesis involves mixing of organic capped II-VI semiconductor nanorods with $AuCl_3$, organic amine and dodecyldimethylammonium bromide (DDAB) in toluene. This method deposit small Au nanoparticles along the nanorod length and gold nucleation sites are believed to be the defect-sites induced by missing surface ligands.

Photochemical deposition of noble metals on semiconductor nanorods generally involves three reactants: a semiconductor as the light absorber, a M^{n+} molecular complex as the metal precursor, and an amine or an alcohol as the sacrificial electron donor. Here, the

semiconductor absorbs photons to generate photoexcited electrons and these electrons reduce and deposit metal on the surface of the semiconductor. Photogenerated-holes are quenched

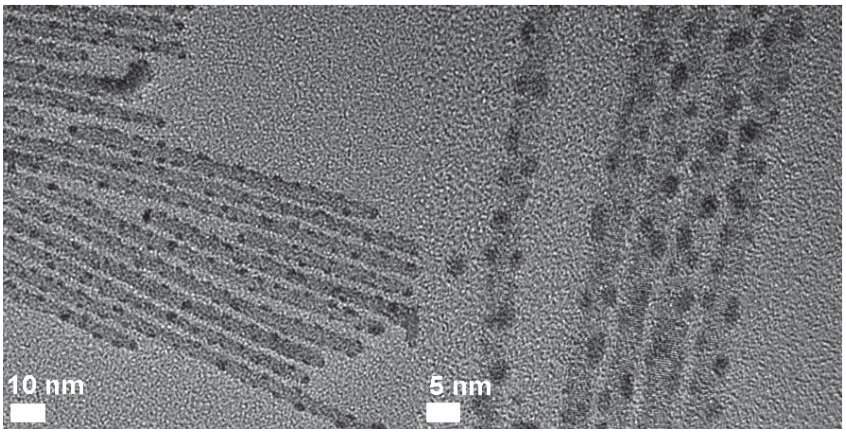

Figure 2. Transmission electron microscopy (TEM) images of CdS-Au heterostructures prepared by thermal method.

by the sacrificial electron donor to prevent the semiconductor etching. This method was first reported by Alivisatos and co-workers for synthesizing Pt-CdS and Pt-CdS/CdSe nanorods. [20]

Photocatalysis by metal-semiconductor heterostructures

In recent years, metal semiconductor heterostructures have been used as a photocatalysts for water splitting and CO_2 reduction.[21] Photocatalytic reactions by metal semiconductor heterostructures can be described in three main steps. First, the semiconductor nanorod absorbs a photon with an energy value lager than the band gap of the semiconductor material and generates a photoexcited electron-hole pair. Second, photoexcited electrons get transferred to the metal nanoparticles on the surface where they are utilized in reduction of H+ or CO_2. Finally, holes are scavenged by a sacrificial agent to prevent nanocrystal degradation by oxidizing holes.

One of the key challenges in designing semiconductor based photocatalysts is the prevention of electron-hole recombination. It is shown that metal nanoparticles on the

semiconductor surface help to increase the rate of electron transfer to the reactants and therefore decelerate the electron-hole recombination.[21 (a)] In addition, the amount of metal loading plays an important role in photocatalytic properties of metal semiconductor nanorods. For instance, increasing Pt nanoparticle size or number of nanoparticles on the surface did not increase the production of H_2 by Pt-CdS nanorods.[22] The efficiency of hole-scavenging also influences the rate of photocatalysis by metal semiconductor nanorods. According to a study by Feldmann *et al*, the driving force for hole scavenging increased in the order of: methanol > disodium ethylenediaminetetraacetic acid > triethanolamine > sodium sulfite. They showed that a high driving force for hole scavenging increased the generation of H_2 by metal semiconductor nanorods.[2]

Thesis Organization

This thesis is comprised mainly of synthesis of II-VI semiconductor based nano-heterostructures and investigating their photocatalytic properties in alcohol dehydrogenation. Chapters 2 through 5 contain material that has already been published.

As the thesis encompasses a diverse range of topics, relevant literature is reviewed in the introduction of each chapter to provide an adequate understanding of the background and significance of the results.

Chapter 2 describes the synthesis of $CdS_{1-x}Se_x$ axially anisotropic nanorods using a single injection method. Chapter 3 discusses the controlled photochemical fabrication of CdS-Pt and CdS-Pd heterostructures as well as site-selective photodeposition of Pd on axially anisotropic CdSSe nanorods. Preliminary experiments on Pt deposition on CdS nanorods were performed by Dr. Mussie Alemsighed and remaining key experiments were performed by Purnima Ruberu. Chapter 4 shows the effect of chalcogenide precursor reactivity on

composition and morphology of II-VI semiconductor nanodots and nanorods. Haley R. Albright, Brandon Callis, Brittney Ward, and Joana Cisneros were undergraduate students who worked in Vela laboratory and helped in running some experiments and characterization of nanodots under the guidance of Purnima Ruberu. Other key experiments and characterizations were carried out by Purnima Ruberu, while initial DFT calculations for phosphine-chalcogenide bond dissociation energy were calculated by Dr. Hua-Jun Fan from Texas Prairie View University. Chapter 6 investigates the photocatalytic properties of CdS-M and $CdS_{1-x}Se_x$- M (M=Pt, Pd) nano-heterostructures in benzyl alcohol dehydrogenation. Nicholas Nelson helped in running gas chromatography experiments and other key experimental work was performed by Purnima Ruberu.

References

[1] Smith, A. M.; Nie, S. *Acc. Chem. Res.* **2010**, *43*, 190-200.

[2] Talapin, D. V.; Lee, J. S.; Kovalenko, M. V.; Shevchenko, E. V. *Chem Rev* **2010**, *110*, 389-458.

[3] Brus, L. E. *J. Chem. Phys.* **1983**, *79*, 5566-5571.

[4] Yu, W. W.; Qu, L. H.; Guo, W. Z.; Peng, X. G. *Chem Mater* **2003**, *15*, 2854-2860.

[5] Mulvaney, P.; Jasieniak, J.; Smith, L.; van Embden, J.; Califano, M. *J Phys Chem C* **2009**, *113*, 19468-19474.

[6] Garcia-Santamaria, F.; Chen, Y.; Vela, J.; Schaller, R. D.; Hollingsworth, J. A.; Klimov, V. I. *Nano Lett.* **2009**, *9*, 3482-3488.

[7] Klimov, V. I.; Li, L. A.; Pandey, A.; Werder, D. J.; Khanal, B. P.; Pietryga, J. M. *J. Am. Chem. Soc.* **2011**, *133*, 1176-1179.

[8] Cademartiri, L.; Bertolotti, J.; Sapienza, R.; Wiersma, D. S.; von Freymann, G.; Ozin, G. A. *J Phys Chem B* **2006**, *110*, 671-673.

[9] Dubertret, B.; Spinicelli, P.; Mahler, B.; Buil, S.; Quelin, X.; Hermier, J. P. Chemphyschem **2009**, *10*, 879-882.

[10] Nozik, A. J. *Chem. Phys. Lett.* **2008**, *457*, 3-11.

[11] Klimov, V. I. *J. Phys. Chem. B* **2006**, *110*, 16827-16845.

[12] Buhro, W. E.; Colvin, V. L. *Nature Mater.* **2003**, *2*, 138-139.

[13] Peng, Z. A.; Peng, X. *J. Am. Chem. Soc.***2001**, *123*, 1389-1395.

[14] Wang, Z. L. *Adv. Mater.* **2000**, *12*, 1295-1298

[15] Kamat, P. V. *J. Phys. Chem. Lett.* **2012**, *3*, 663-672.

[16] Carbonea, L.; Cozzolia, P. D. *Nano Today* **2010**, *5*, 449-493.

[17] Maeda, K.; Domen, K. *J. Phys. Chem. Lett.* **2010**, *1*, 2655-2661.

[18] Vaneski, A.; Susha, A. S.; Rodríguez-Fernández, J.; Berr, M.; Jäckel, F.; Feldmann, J.; Rogach, A. L. *Adv. Funct. Mater.* **2011**, *21*, 1547–1556.

[19] (a) A. E. Saunders , I. Popov , U. Banin , *J. Phys. Chem. B* **2006**, *110*, 25421-25429. (b) Menagen, G.; Macdonald, J. E.; Shemesh, Y.; Popov, I.; Banin, U. *J. Am. Chem. Soc.* **2009**, *131*, 17406-17411. (c) Mokari, T.; Rothenberg, E.; Popov, I.; Costi, R.; Banin, U. *Science* **2004**, *304*, 1787-1790.

[20] Dukovic, G.; Merkle, M. G.; Nelson, J. H.; Hughes, S. M.; Alivisatos, A. P. *Adv. Mater.* **2008**, *20*, 4306-4311.

[21] (a) Berr, M. J.; Vaneski, A.; Mauser, C.; Fischbach, S.; Susha, A. S.; Rogach, A. L.; Jackel, F.; Feldmann, J. *Small* **2012**, *8*, 291-297. (b) Amirav, L.; Alivisatos, A. P. *J. Phys. Chem. Lett.* **2010**, *1*, 1051-1054. (c) Shemesh, Y.; Macdonald, J. E.; Menagen, G.; Banin, U. *Angew. Chem. Int. Ed.* **2011**, *50*, 1185-1189. (d) Maeda, K.; Domen, K. *J. Phys. Chem. C* **2007**, *111*, 7851- 7861.

[22] Beer, M.; Vaneski, A.; Susha, A. S.; Rodiguez-Fernandez, J.; Dçblinger, M.; Jackel, F.; Rogach, A. L.; Feldmann, J. *J. Appl. Phys. Lett.* **2010**, *97*, 093108.

[23] Berr, M. J.; Wagner, P.; Fischbach, S.; Vaneski, A.; Schneider, J.; Susha, A. S.; Rogach, A. L.; Jackel, F.; Feldmann, J. *J. Appl. Phys. Lett.* **2012**, *100*, 223903.

CHAPTER 2

EXPANDING THE ONE-DIMENSIONAL CdS-CdSe COMPOSITION LANDSCAPE: AXIALLY ANISOTROPIC $CdS_{1-x}Se_x$ NANORODS

Reprinted with permission from *ACS Nano,* **2011**, *5,* 5775.

T. Purnima A. Ruberu, Javier Vela

Abstract

We report the synthesis and characterization of $CdS_{1-x}Se_x$ nanorods with axial anisotropy. These nanorods were synthesized via single injection of a mixture of trioctylphosphine sulfur and selenium precursors to a cadmium-phosphonate complex at high temperature. Transmission electron microscopy shows nanoparticle morphology changes with relative sulfur and selenium loading. When the synthetic selenium loading is between 5% and 10% of total chalcogenides, the nanorods exhibit pronounced axial anisotropy characterized by a thick ‘head’ and a thin ‘tail.’ The nanorods' band gap red shifts with increasing selenium loading. X-Ray diffraction reveals $CdS_{1-x}Se_x$ nanorods have a wurtzite crystal structure with a certain degree of alloying. High resolution and energy filtered transmission electron microscopy, and energy dispersive X-ray spectroscopy confirms the head of the anisotropic nanorods is rich in selenium, whereas the tail is rich in sulfur. Time evolution and mechanistic studies confirm the nanorods form by quick growth of the CdSe-rich head, followed by slow growth of the CdS-rich tail. Metal photodeposition reactions with 575 nm irradiation, which is mostly absorbed by the CdSe-rich segment, show effective electronic communication between the nanorods head and tail segments.

Introduction

One-dimensional ('1D') colloidal semiconductors (nanorods, nanowires) have been subject of much recent interest.[1-7] For the particular case of cadmium chalcogenide nanorods, seminal papers have addressed their general synthesis,[8-14] nucleation and growth,[15] diameter and length control,[13,16] and morphology variants such as arrow-, teardrop-, and branched (tetra- and multi-pod)-shaped nanocrystals.[17,18] Significant attention has been paid to the microscopic mechanism of uncatalyzed anisotropic growth of cadmium chalcogenide nanorods made *via* hot injection methods. At low precursor concentrations, surface area minimization *via* Ostwald ripening favors formation of spherically shaped ('0D') colloidal nanocrystals (dots). However, typical nanorod preparations use cadmium oxide (CdO) and a bulky phosphonic acid such as octadecyl phosphonic acid (ODPA). The resulting cadmium-phosphonic acid complex is very stable and serves as a slow, controlled source of cadmium ions helps maintain a high precursor concentration.[19] At high precursor concentrations, the relative growth rates of different crystallographic facets play a major role in determining the final shape of the nanocrystals.[17,20] This is particularly important for wurtzite-type cadmium chalcogenides, which are intrinsically anisotropic materials with a unique *c* axis.[15,21] Two possible facets perpendicular to wurtzite *c* axis are 001 and $00\bar{1}$ facets, which terminate respectively on positively-charged Cd and negatively-charged Se ions. Various studies have proven the $00\bar{1}$ facet has the highest growth rate of all facets.[17,21] These Se-rich $00\bar{1}$ facets are relatively uncoated because ligands in solution are usually electron donating. In addition, the permanent dipole moment along the unique *c* axis enhances the chemical potential of the $00\bar{1}$ facet.[22,23] The unique structural features of the $00\bar{1}$ facet favor unidirectional growth on this facet, that is, along the *c* axis.[24]

Continued research on synthesis of colloidal nanocrystals is quickly moving towards new preparative methods of increased power and complexity. Of particular interest is finding new ways to produce heterostructured and highly anisotropic nanocrystals –those made up by two or more distinct phases and containing very large aspect ratios and/or different shapes– that could be assembled into functional materials and devices. In the case of cadmium chalcogenide nanocrystals, different groups have reported syntheses for spherical (0D) alloyed $CdS_{1-x}Se_x$,[25-28] $CdSe_xTe_{1-x}$[29] and $Cd_{1-x}Hg_xTe$[30] quantum dots, core/shell CdSe/CdS,[31-34] CdTe/CdS,[35,36] CdSe/ZnS,[37-40] and CdSe/ZnSe[41] quantum dots, multishell $CdS/Zn_{0.5}Cd_{0.5}S/ZnS$ quantum dots,[42] as well as one-dimensional (1D) core/shell CdSe/CdS and CdSe/ZnS nanorods,[43-46] CdSe-CdTe segmented nanorods,[47-49] alloyed CdHgTe nanorods,[50] alloyed $CdS_{1-x}Se_x$ nanowires,[51] co-axial core/shell Si/CdSSe nanowires,[52] segmented CdS-CdSe[53] and CdSe-ZnSe[54] nanowires, seeded CdSe-CdS,[45] CdTe-CdSe[55] and $CdSe_xTe_{1-x}$ rods[56] and tetrapods,[57] CdS-Ag_2S nanorod superlattices,[9] and CdSSe nanoribbons.[58,59] There is also increasing interest in cadmium chalcogenide-metal hybrid nanomaterials,[60-63] including CdS, CdSe and CdSe/CdS nanorods bound to PbSe,[64] Fe_2O_3,[65,66] Bi,[54] Fe-Pt,[67] Au,[68,69] Pt,[70-73] Pd,[74] and Co nanoparticles.[75,76]

In this paper, we report the synthesis of axially anisotropic, colloidal $CdS_{1-x}Se_x$ nanorods that are characterized by having distinct thick and thin ends. These nanocrystals form spontaneously over relatively long reaction periods (~1.4 h) when a mixture of trioctyl phosphine sulfide and selenide (TOPS and TOPSe) is used as chalcogenide source, specifically with TOPS to TOPSe ratios between 95:5 and 9:1. Using a combination of optical and structural characterization methods, we show the amount of Se in these nanorods is much higher (up to 6×) than what could be expected from TOPSe loading used during their

synthesis. We also show axially anisotropic $CdS_{1-x}Se_x$ nanorods are single-crystalline, with an axial composition gradient between a CdSe-rich thick end, and a CdS-rich thin end. Using different control experiments, we explore the mechanism of formation of these axially anisotropic nanorods, and establish they form in a sequential manner, where quick growth of a CdSe-rich head ($\leq$ 20 min) precedes slow growth of a CdS-rich tail (~85 min). Finally, we probe the degree of electronic communication between the two segments of the nanorods by carrying out palladium photodeposition experiments. We show palladium photodeposition occurs along the whole length of the nanorods using a lamp whose light is absorbed by the smaller band gap CdSe-rich segment, but not by the larger band gap CdS-rich segment.

Results and Discussion

As part of a study directed at harvesting sunlight with one-dimensional semiconductor colloids, we became interested in CdSe based on its relatively small band gap (1.7 eV bulk). However, we faced difficulties in making CdSe nanorods and frequently obtained instead mixtures of CdSe dots, rods, and multipods. While we amply recognize these complications arise from variable amounts of impurities present in different batches of chemicals, removing such impurities by purification added unwanted and lengthy extra steps to our synthesis. In contrast, we noted a procedure recently reported for making CdS nanorods is highly reproducible, even without prior purification of precursors or ligands.[9] This procedure involves reaction between trioctylphosphine sulfide (TOPS) and an *in-situ* generated cadmium-octadecyl phosphonate complex in trioctylphosphine oxide at 315°C for 85 min, and results in long (154.1 ± 30.4 nm) and thin (5.6 ± 0.8 nm diameter) CdS nanorods with a high aspect ratio (length / diameter) of 27 and a small size-dispersion (Figure 1a and entry 1 in Table 1). Unfortunately, CdS is a bluer, larger band-gap (2.4 eV bulk) material compared

to CdSe, and is less attractive for harvesting sunlight. Nonetheless, we reasoned that introducing small amounts of Se during synthesis might lead to $CdS_{1-x}Se_x$ nanorods with a smaller band gap compared to pure CdS.

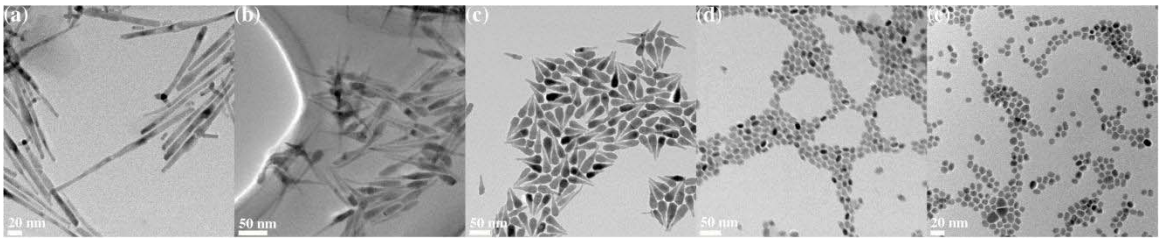

Figure 1. TEM micrographs showing $CdS_{1-x}Se_x$ morphology as a function of Se loading (actual EA composition in parenthesis): (a) 0% Se loading (CdS), (b) 5% Se loading ($CdS_{0.68}Se_{0.32}$), (c) 10% Se loading ($CdS_{0.42}Se_{0.58}$), (d) 20% Se loading ($CdS_{0.33}Se_{0.67}$), (e) 100% Se loading (CdSe). Scale bars: 20 nm (a, e), 50 nm (b, c, d).

Table 1. Composition and dimensions of axially-anisotropic $CdS_{1-x}Se_x$ nanorods

Entry	Rxn. time / min	%Se Loading [a]	%Se Composition: EA[b] (XRD)[c]	Total length / nm (XRD)[d]	Head diameter / nm	Tail diameter / nm	Aspect ratio[e]
1	85	0	0[b] (0)[c]	154.1 ± 30.4 (43.0)[d]	5.6 ± 0.8	5.6 ± 0.8	27
2	85	5	32[b] (45)[c]	91.3 ± 6.4 (24.0)[d]	12.8 ± 1.9	3.7 ± 0.4	7.0
3	85	10	58[b] (63)[c]	59.3 ± 8.0 (29.1)[d]	17.8 ± 2.4	5.6 ± 0.8	3.3
4	85	20	67[b] (81)[c]	20.5 ± 2.9 (13.4)[d]	11.8 ± 1.7	11.8 ± 1.7	1.7
5	85	100	100[b] (100)[c]	11.4 ± 2.1 (10.5)[d]	8.5 ± 1.0	8.5 ± 1.0	1.3
6[g]	20	5	n.d.[f] (n.d.)[f]	51.8 ± 5.4[g] (n.d.)[f]	14.0 ± 1.1[g]	14.0 ± 1.1[g]	3.7
7[h]	85	- - -[h]	n.d.[f] (n.d.)[f]	37.5 ± 7.4 (n.d.)[f]	10.2 ± 1.1	3.7 ± 0.6	3.7

[a]%Se used during synthesis. [b]Determined by elemental analysis. [c]Estimated from XRD. [d]Calculated from (002) peak. [e]Minimum aspect ratio = Length / Head diameter. [f]Not determined. [g]Also observed small dots with a diameter = 3.1 ± 0.8 (see Figure 8a). [h]Made in presence of pre-made pure CdSe nanorods, using a 0% Se loading.

$CdS_{1-x}Se_x$ nanorod morphology. To test this idea, we replaced TOPS in the injection solution with a mixture of TOPS and TOPSe while keeping the total chalcogenide concentration constant. To our surprise, replacing a fraction of TOPS with TOPSe not only leads to $CdS_{1-x}Se_x$ nanorods, but such $CdS_{1-x}Se_x$ nanorods can display a high degree of anisotropy along their main axis when the total amount of chalcogenides contains 10% or less Se loading. Figure 1 shows the morphology of $CdS_{1-x}Se_x$ nanocrystals that result from changing Se loading in each preparation. Figure 2 shows the corresponding changes in $CdS_{1-x}Se_x$ nanorod length, diameter, and aspect ratio as a function of Se loading. These trends are quantitatively summarized in Table 1.

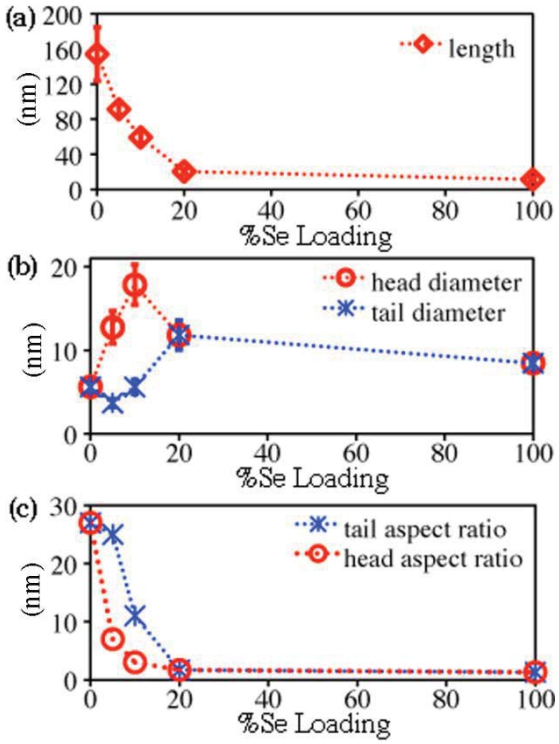

Figure 2. Effect of %Se loading on $CdS_{1-x}Se_x$ length (a), diameter (b), and aspect ratio (c).

At 0% Se loading, long nanorods form with a consistent diameter of 5.6 ± 0.8 nm along their whole length (Figure 1a and entry 1 in Table 1). Increasing Se loading between 1% and 10% leads to axially anisotropic nanorods having two distinct fat (head) and thin (tail) ends (Figure 2b). For example, at 5% Se loading the nanorods have head and tail diameters of 12.8 ± 1.9 nm and 3.7 ± 0.4 nm, respectively, whereas at 10% Se loading the nanorods have head and tail diameters of 59.3 ± 8.0 nm and 17.8 ± 2.4 nm, respectively. We casually referred to these nanocrystals as having 'tadpole' (5% Se) or 'drumstick' (10% Se) morphology (Figure 1b-c and entries 2-3 in Table 1). Qualitatively, these tadpole and drumstick $CdS_{1-x}Se_x$ nanocrystals appear to have similar morphology to 'paddle' CdS and 'teardrop' CdSe nanocrystals previously reported in the literature.[13,17] Increasing Se loading above 10% Se leads to progressively shorter nanorods that once again retain a consistent diameter along their length (Figure 2b). For example, at 20% Se loading nanorods have a consistent diameter of 11.8 ± 1.7 nm (Figure 1d-e and entries 4-5 in Table 1). Across the $CdS_{1-x}Se_x$ series, the nanorods length dramatically decreases from 154.1 ± 30.4 nm to 11.4 ± 2.1 nm for 0% and 100% Se loading, respectively (Figure 2a).

Optical properties of $CdS_{1-x}Se_x$ nanorods. As initially expected, the absorption spectrum of $CdS_{1-x}Se_x$ nanorods is red-shifted compared to pure CdS nanorods. Figure 3a shows the absorption edge of $CdS_{1-x}Se_x$ nanorods shifts to longer wavelengths as Se loading increases, and Figure 3b shows the corresponding change in apparent band gap (estimated from 1st absorption peak). As shown in Figure 3b, even a modest increase in Se loading, from 0% to 5% Se causes a dramatic drop in apparent band gap. This strongly indicates the concentration of Se in these nanocrystals is much higher than calculated based on synthetic Se loading alone (see further discussion below). The photoluminescence properties of $CdS_{1-x}Se_x$

nanorods also change depending on the amount of Se present, and the observed changes are compounded by the nanorods' complex composition and structure (presented below). Qualitatively, figures 3c and 3d show preparations that using Se loadings between 10-100% result in weakly luminescent nanorods, with maximum relative luminescence (QY ≈ 0.2%) corresponding to nanorods obtained with a 20% Se loading.

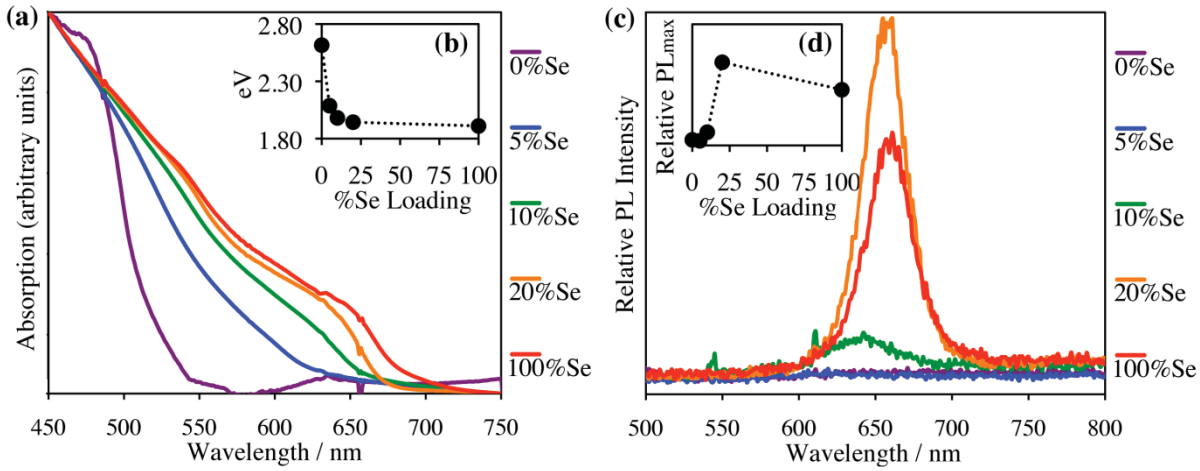

Figure 3. $CdS_{1-x}Se_x$ optical properties: Change in absorption (a), band gap (b), and PL intensity (c, d) with increasing Se loading. (Low solubility of CdS nanorods results in scattering above 500 nm)

$CdS_{1-x}Se_x$ nanorod structure and overall composition. Figure 4a shows powder X-ray diffraction patterns of several $CdS_{1-x}Se_x$ nanorod samples with different Se loadings. Each XRD pattern consists of a single set of peaks most consistent with a hexagonal, wurtzite crystal structure. We can rule out the presence of two separate pure CdS and CdSe phases in these samples based on the fact that each $CdS_{1-x}Se_x$ XRD pattern consists of a single set of peaks (Figure 4a). A control sample made by mixing pure CdS and CdSe nanorods (0% Se and 100% Se) has an XRD pattern that consists of two distinct sets of peaks, with two peaks showing for each set of lattice planes (Figure 4a). In contrast, all $CdS_{1-x}Se_x$ nanorod samples with $1 > x > 0$ show a single peak for each set of lattice planes, and individual 2·theta values fall in between the values for pure wurtzite CdS and CdSe phases reported in the Inorganic

Crystal Structure Database (ICSD 2010-2/2010 from Fachinformationszentrum Karlsruhe (FIZ) and NIST. FindIt Version 1.7.1.). Individual diffraction peaks progressively shift to smaller 2·theta (2θ) values (wider *d*-spacings) with increasing Se loading, in agreement with lattice expansion to accomodate the incorporation of increasing amounts of larger Se ions. This indicates some type of alloying between CdS and CdSe phases in these nanostructures. To investigate this further we plotted the experimentally measured *d* spacings for each set of lattice planes as a function of Se loading. Figure 4b shows such plot is non-linear but highly curved, which is typical of non-Vegard behavior.[77] This observation strongly indicates the nanocrystals may not be completely alloyed, but instead contain some degree of heterostructuring, perhaps in the form of a graded alloy. Note: A homogeneous alloy or solid solution could have formed based on relative S^{2-} (1.7 Å) and Se^{2-} (1.84 Å) ionic sizes (8.2% difference), and CdSe (7.010 Å), and CdS (6.749 Å) wurtzite lattice paramaters (3.9% lattice mismatch).

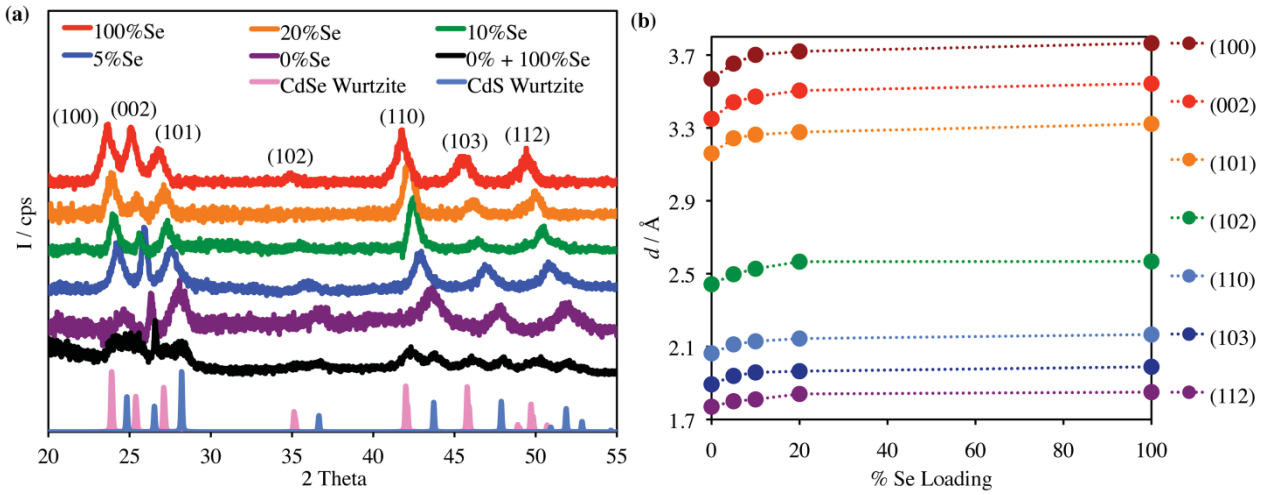

Figure 4. (a) $CdS_{1-x}Se_x$ XRD patterns for different %Se loadings. XRD patterns of a pure CdS/pure CdSe mix. (0%+100% Se loading), and bulk wurtzite(hexagonal) CdSe and CdS are shown for comparison. (b) Change in $CdS_{1-x}Se_x$ interplanar *d*-spacings as a function of %Se loading.

Another feature observed from powder diffraction data is that the length of the nanorods calculated from the (002) XRD peak is almost always shorter than measured from TEM (Table 1). This behavior has been previously observed and attributed to the presence stacking faults along nanorods length, which effectively decreases the apparent nanocrystal size.[17] Figure 4b also shows individual XRD peaks occur at smaller 2·theta values and correspond to larger *d* spacings than could be expected from Se loadings used in the synthesis. Figure 5 shows the actual composition of $CdS_{1-x}Se_x$ nanorods obtained from experimental XRD data as well as from chemical elemental analysis (EA). Both XRD and EA data confirm the nanorods' actual Se content is always higher than the Se loading used during their synthesis, which strongly indicates Se has a higher tendency than S to incorporate into these nanostructures. By comparing experimental XRD and EA data with the corresponding Se loadings (Table 1), we estimate there is a three- to nine-fold (3-9×) preference for Se over S to go into these nanostructures.

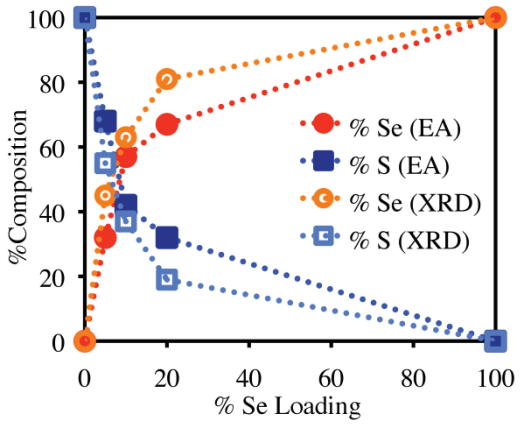

Figure 5. $CdS_{1-x}Se_x$ composition obtained experimentally from elemental analysis and X-ray diffraction plotted against synthetic Se loading.

S- and Se-atom distribution in $CdS_{1-x}Se_x$ nanorods. The unusual anisotropic morphology observed by TEM suggests $CdS_{1-x}Se_x$ nanorods possess an inhomogeneous composition along their length.[25] To answer this question, we resorted to high-resolution HR-TEM,

energy dispersive X-ray spectroscopy (EDS), and energy-filtered (EF) TEM. Figure 6 shows representative EDS and HR-TEM data of drumstick-like $CdS_{0.42}Se_{0.58}$ nanorods that result from 10% Se loading. EDS line scans along the nanorods' main axis show Se content dramatically increases on going from tail to head regions (Figure 6a-b). HR-TEM confirms nanorods are single crystalline as judged by the continuity in lattice fringes along their structure (Figure 6b). We also used HR-TEM to measure interplanar *d* spacings at different points along the length of several of these nanorods, and found the *d* spacings get consistently larger on going from the tail to head regions. This can be attributed to a higher fraction of larger Se atoms at the head and a higher fraction of smaller S atoms at the tail of the nanorods. The net result of this composition gradient is lattice expansion towards the head of the nanorods.

Figure 7 shows three registered TEM and energy-filtered (EF) TEM images of tadpole-like $CdS_{0.68}Se_{0.32}$ nanorods that result from 5% Se loading. In agreement with what is observed by EDS and HR-TEM on the shorter nanorods, Se-channel EF-TEM indicates Se is preferentially located at the thicker head region of the nanorods (Figure 7a vs. b), whereas the S-channel EF-TEM image indicates S distributes along the whole length of the nanorods (Figure 7c vs. b). Taken together, these EDS, HR-TEM, and EF-TEM results unambiguously confirm Se incorporates preferentially at the head region of the nanorods, whereas mostly S is present at the tail region of the nanorods. The structural and single crystalline continuity of the nanorods along their axis, along with progressively increasing Se concentration towards their head is consistent with these structures being graded alloys.

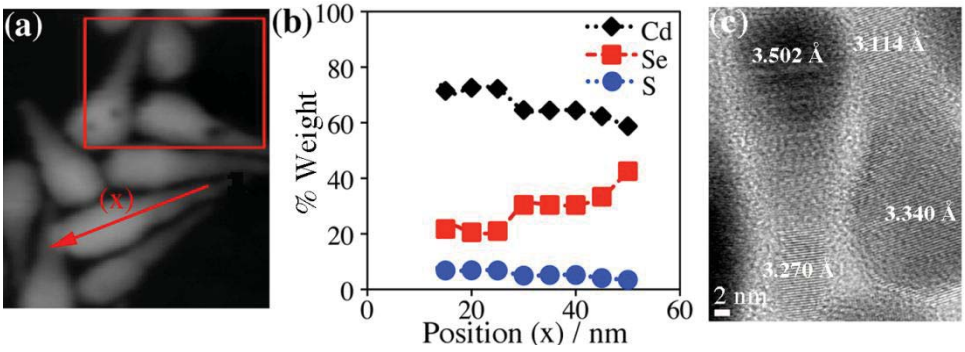

Figure 6. Individual $CdS_{0.42}Se_{0.58}$ nanorod sample analyses: (a) Direction and length(x), and (b) composition plot of an EDS line scan (arrow length=50 nm; square area was used for drift correction). (c) HR-TEM micrograph showing interplanar (002) *d* spacings (perpendicular to *c* axis) become progressively larger from the tail to the head of the nanorods.

Formation mechanism of anisotropic $CdS_{1-x}Se_x$ nanorods. Having established the heterostructured, graded-alloy composition of anisotropic $CdS_{1-x}Se_x$ nanorods, we turned our attention to their growth mechanism. Our most immediate question was whether CdSe-rich (head) and CdS-rich (tail) segments formed (a) concomitantly (that is, both segments form in parallel simultaneously), (b) sequentially (one segment forms first, the other forms from it), or (c) independently of each other.

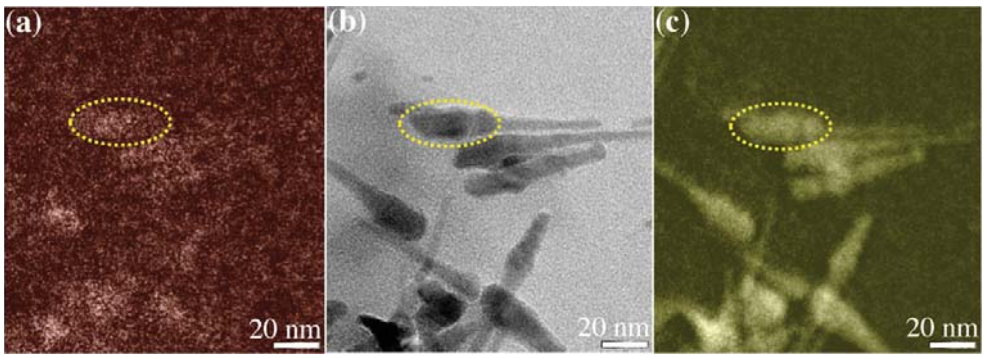

Figure 7. Registered EF-TEM images of tadpole-like $CdS_{0.68}Se_{0.32}$nanorods: (a) Se-channel, (b) regular-TEM, and (c) S-channel.

To probe this question, we studied time evolution of particles by stopping the reaction and characterizing products at different times. Figure 8a-c shows key results from such experiments using $CdS_{0.68}Se_{0.32}$ nanorods obtained with a 5% Se loading as a model system.

At relatively short reaction times, for example after 20 min, we observed formation of thick nanorods (51.8 nm ± 5.4 nm in length, 14.0 nm ± 1.1 nm in diameter) along with a few small dots (3.1 nm ± 0.8 nm) (Figure 8a and entry 6 in Table 1). However, after 85 min thick nanorods appeared to grow a thin tail and produced tadpole-like, final anisotropic nanorods (91.3 nm ± 6.4 nm in length), whereas small dots disappeared (Figure 8b and entry 2 in Table 1). Interestingly, the diameter of the 20 min nanorods (14.0 nm ± 1.1 nm) and head diameter of the 85 min nanorods (12.8 nm ± 1.9 nm) are the same within experimental error, strongly suggesting both shares the CdSe-rich composition described above. Formation of a few small dots and their eventual disappearance along with formation of long nanorod tails is consistent with initial formation of CdS homo-nuclei, which dissolve over time in favor of heterogeneous nucleation on one side of the thick CdSe nanorods along the *c*-axis, perpendicular to the (002) set of planes. To confirm these results, we repeated the procedure used to make pure CdS nanorods (using only TOPS or with a 0% Se loading) in presence of pure CdSe nanorods (pre-made using only TOPSe or with a 100% Se loading) (Figure 8d-f). In absence of CdSe nanorods, pure and long CdS nanorods are formed as shown previously (see above).[9] However, in presence of CdSe nanorods, these acted like seeds for formation of highly anisotropic, drumstick-like $CdS_{1-x}Se_x$ nanorods (Figure 8e), in agreement with the time-dependent mechanistic experiment above.

We then attempted to form anisotropic nanorods from preformed CdS nanorods by reacting pure CdS nanorods with TOPSe (Figure 8g-i). This experiment was unsuccessful, in that the length (188.3 nm ± 53.4 nm), diameter (9.1 nm ± 4.6 nm), and overall aspect of the initial CdS nanorods remained constant within experimental error. Some etching of the CdS nanorod surface occurred however, as judged by formation of a few medium size dots

consistent with formation of CdSe (10. 8 nm ± 2.6 nm) (Figure 8h). Additional experiments where we treated CdS nanorods with both TOPSe and Cd-phosphonate precursors were similarly unsuccessful, leading to rectangular 'block'-shaped nanocrystals with dimensions (65.2 nm ± 8.8 nm) × (18.7 nm ± 3.8 nm) instead of axially anisotropic nanorods (not shown). Together, these results demonstrate that while 'thin' CdS tails can form starting from 'fat' CdSe nanorod seeds, the opposite cannot happen, namely 'fat' CdSe heads cannot form from 'thin' CdS tail seeds. In other words, formation of heterostructured, graded-alloy anisotropic $CdS_{1-x}Se_x$ nanorods is a sequential process that starts by quick growth of a CdSe-rich nanorod head, followed by slow growth of a CdS-rich tail.

Perhaps an even more intriguing question is the reason behind sequential formation of axially anisotropic $CdS_{1-x}Se_x$ nanorods. It is clear from our observations that under the experimental conditions used in this study the rate of CdSe nanorod (head) growth (≤ 20 min) is much faster than the rate of CdS nanorod (tail) growth (~85 min). The relative ease of formation of these nanorods cannot be a consequence of relative thermodynamics of crystalline energies, since CdS is a much more stable crystalline system compared to CdSe: Based on literature thermochemical data,[78] we calculate the lattice energy of CdS, 834 kcal/mol is significantly higher than for CdSe, 798 kcal/mol. These values are consistent with the melting points of CdS, 1748°C, and CdSe, 1512°C. Instead, we believe the relative ease of formation of nanorods is a consequence of relative reactivity of TOPS and TOPSe in solution. For tertiary alkyl phosphines such as TOP, the strength of a terminal P-Se bond is 75 kcal/mol, whereas the strength of a terminal P-S bond is 96 kcal/mol.[79] Because of the significantly weaker P-chalcogen bond strength in TOPSe compared to TOPS, by 21 kcal/mol, one can expect TOPSe to be much more reactive towards the Cd-phosphonate precursor than TOPS, leading

to faster formation of CdSe compared to CdS. This suggests it may be possible to control relative degrees of Se and S in these and other nanostructures by judicious control of molecular precursor but further work is needed to confirm this idea.

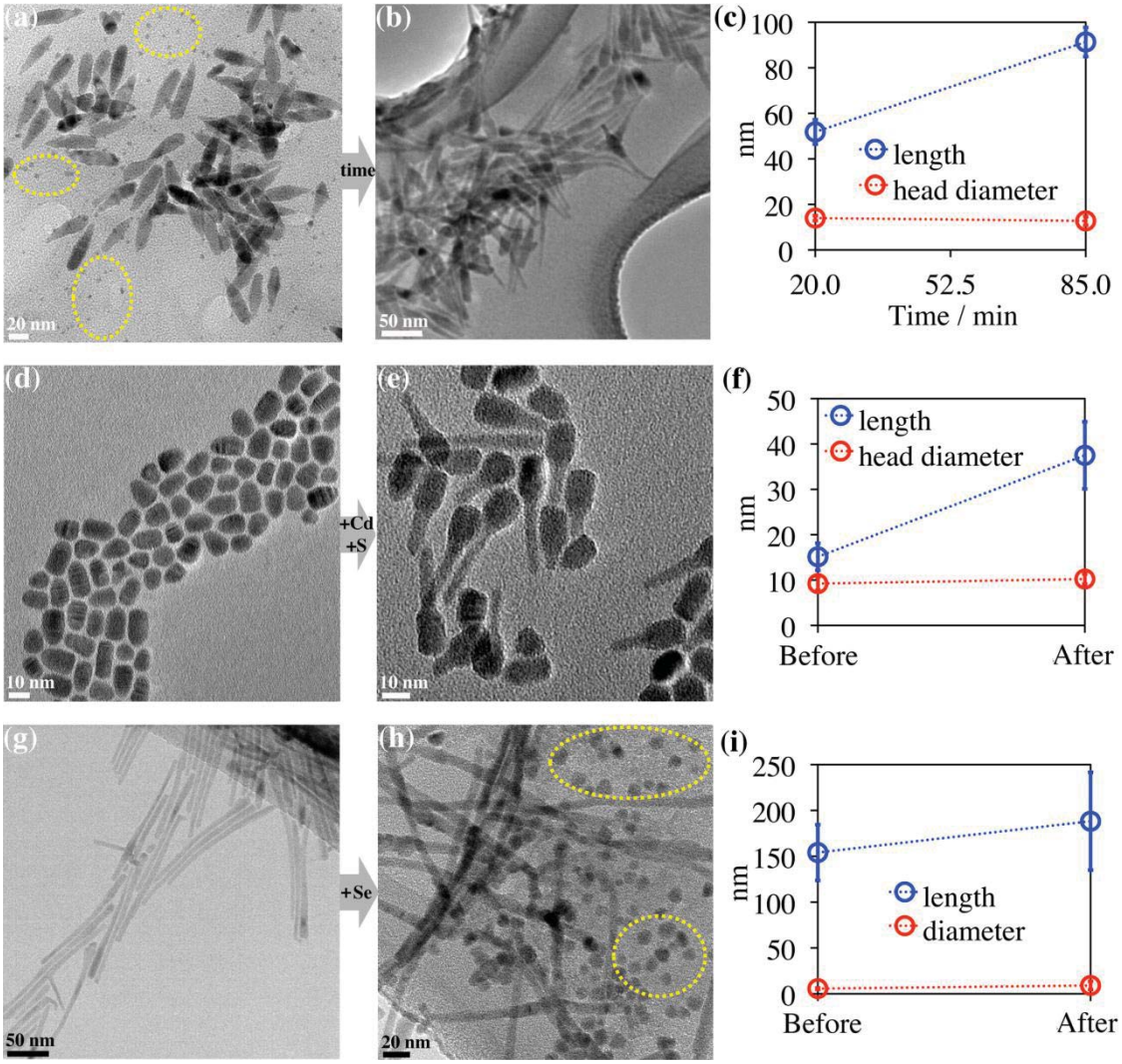

Figure 8. Mechanistic investigations of anisotropic $CdS_{1-x}Se_x$ nanorod formation: (a-c) Time evolution of $CdS_{0.68}Se_{0.32}$ nanorods: At short reaction times (20 min), the nanorods head has already formed, along with very small CdS nuclei (circled) (a). Over time (85 min total reaction time), small CdS nuclei dissolved and only final $CdS_{0.68}Se_{0.32}$ nanorods were observed. (d-i) Independent formation of $CdS_{1-x}Se_x$ nanorods from preassembled elements: (d-f) Reaction of CdSe nanorods (d) with Cd and S precursors results in $CdS_{1-x}Se_x$ nanorod formation (e), (g-i) whereas reaction of CdS nanorods (g) with Se does not (a few CdSe nuclei, circled, formed instead) (h).

Electronic communication among CdSe- and CdS-rich segments. A key feature sought for many potential applications of heterostructured nanomaterials is good optical and electronic communication between the heterostructure's different components. To probe this aspect, we carried out photodeposition of palladium nanoparticles on axially anisotropic $CdS_{1-x}Se_x$ nanorods (Figure 9). Others, [60-76] and we [(to be communicated)] have independently observed photodeposition of metals on the surface of colloidal semiconductor nanocrystals can be selectively carried out using lasers or fluorescent lamps. Light absorption by the semiconductor results in formation of electron-hole pairs that can be subsequently quenched by surface defect or 'trap' states. The resulting surface-localized electrons can serve as reduction and seeding points for formation of metal nanoparticles from soluble organometallic precursors. Here, we used a 575 nm lamp (~75 nm fwhm) and $(TMEDA)PdMe_2$ to deposit Pd on $CdS_{0.42}Se_{0.58}$ nanorods obtained with a 10% Se loading (Figure 9). After 1 h irradiation, Pd nanoparticles formed having a size of 5.0 ± 1.5 nm, with an average of 1.3 Pd particles per nanorod, and a maximum of 3 Pd particles per nanorod. After 3 h irradiation, Pd nanoparticles formed having a size of 5.1 ± 1.4 nm, with an average of 8.0 Pd particles per nanorod, and a maximum of 15 Pd particles per nanorod (Figure 9). Clearly, irradiation time does not impact Pd nanoparticle size, however Pd loading greatly increases with longer irradiation times as evidenced by the non-linear, large increase (6×) in number of Pd particles per rod on going from 1 h to 3 h irradiation (1.3 Pd particles to 8.0 Pd particles, respectively). Based on the band edge position of the two different CdS- or CdSe-rich domains, light emitted by the 575 nm lamp is strongly absorbed by the CdSe-rich head (~650 nm absorption edge), but not by the CdS-rich tail (~500 nm absorption edge). Because

Pd nanoparticles form not only on the head but also on the tail of the nanorods (Figure 9c), we infer excitons can travel unimpeded across whole $CdS_{1-x}Se_x$ graded alloy nanocrystals. In other words, exciton quenching by surface defects appears to occur at any point on the surface of these nanorods, leading to photoreduction of the Pd molecular precursor and surface seeding of Pd nanoparticles along the whole length of $CdS_{0.42}Se_{0.58}$ nanorods. A full detailed account on metal photodeposition behavior, characterization, and application of the resulting nanostructures will be the subject of a separate article.

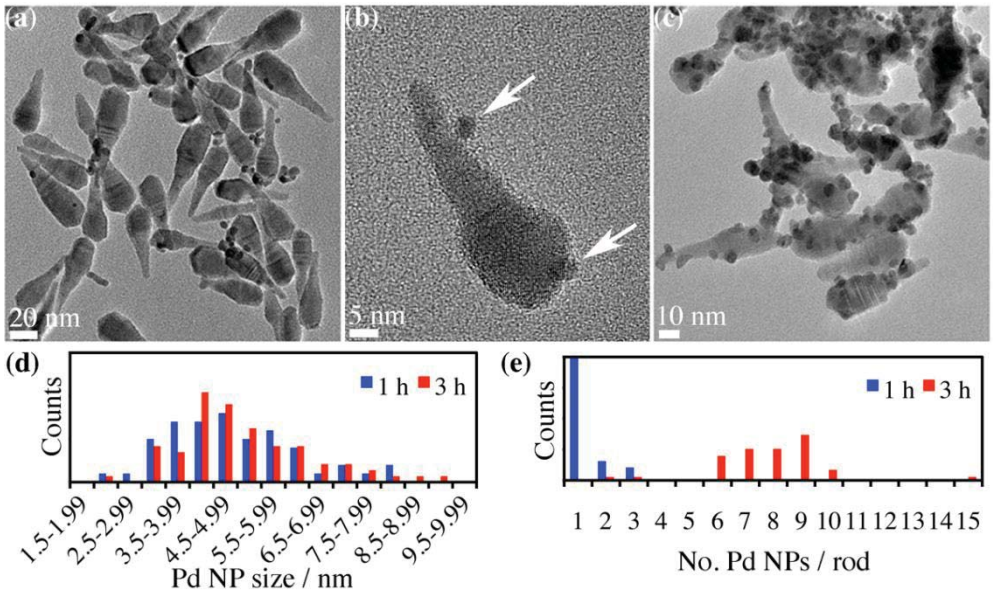

Figure 9. Photodeposition of Pd nanoparticles on $CdS_{0.42}Se_{0.58}$ nanorods obtained with a 10% Se loading: (a, b) 575 nm lamp, 1 h irradiation. (c) 575 nm lamp, 3 h. (The arrows in b point to Pd particles on tail and head segments). (d) Pd nanoparticle size histogram. (e) Pd nanoparticle count per nanorod histogram. (Size measurements and statistics were obtained for at least 50-100 particles)

Conclusions

In summary, we have prepared axially anisotropic $CdS_{1-x}Se_x$ nanorods *via* a single injection of a mixture of TOPS and TOPSe precursors to a hot cadmium-phosphonate complex. The morphology of the resulting nanocrystals strongly depends on relative amounts of S and Se used. Axially anisotropic nanorods with a thick head segment and a thin tail

segment are obtained when the Se loading is between 5% and 10% of total chalcogenides. The aspect ratio of the nanorods decreases as Se loading increases. The optical properties of the nanostructures are tunable with composition. The absorption band edge of these nanostructures red-shifts with increasing Se loading. X-Ray diffraction and elemental analyses show the actual Se content in $CdS_{1-x}Se_x$ nanorods is consistently higher than synthetic Se loading. X-Ray diffraction data, Vegard's plots, and high-resolution TEM studies confirm axially anisotropic nanorods possess a graded alloyed structure. Elemental mapping by energy dispersive spectroscopy and energy filtered TEM showed the head region of anisotropic nanorods is rich with Se and the tail region is rich with S. Time dependent evolution studies show formation of these nanorods starts with homogeneous nucleation and quick growth of a thick CdSe-rich head, followed by heterogeneous nucleation and slow growth of a CdS-rich thin tail. This anisotropic growth can be attributed to the stability of chalcogenide precursors. TOPSe is less stable and more reactive compared to TOPS. As a result, TOPSe reacts with cadmium-phosphonate much faster, forming the head segment first. Over time, TOPS slowly reacts with cadmium-phosphonate, forming the thin tail segment along the *c* axis. Mechanistic experiments show the opposite synthetic sequence is not possible. Namely, formation of a CdSe-rich head does not occur starting from a CdS-rich tail. Metal deposition experiments conducted using 575 nm light irradiation show there is good electronic communication between the CdS-rich and CdSe-rich segments. We are currently exploring using axially anisotropic $CdS_{1-x}Se_x$ nanorods and $CdS_{1-x}Se_x$-Pd heterostructures as building blocks for more complex nanostructures and devices.

Experimental Section

Materials. Cadmium oxide (99.998%) and sulfur (99.999%) were purchased from AlfaAesar, octadecylphosphonic acid (ODPA) from PCI Synthesis, selenium (99.999%), trioctylphosphine oxide (TOPO) (99%), triethylamine (≥99.5%), and anhydrous toluene from Sigma-Aldrich, and trioctylphosphine (TOP) (97%) and cis-dimethyl(N,N,N,'N'-tetramethylethylenediamine)palladium(II) ((TMEDA)$PdMe_2$) (99%) from Strem. Materials were used as received unless specified otherwise. CdS nanorods (154.1±30.4 nm length, 5.6±0.8 nm diameter) were prepared according to a literature procedure.[9] Elemental analyses were performed by Galbraith Laboratories, Inc., of Knoxville, Tennessee.

Synthesis of $CdS_{1-x}Se_x$ nanorods. *TOP-Chalcogen stock solutions.* A solution of S (407.7 mg, 12.5 mmol) in TOP (4.61 g, 12.5 mmol) (2.25 M TOPS stock solution), and a solution of Se (987.0 mg, 12.5 mmol) in TOP (4.61 g, 12.5 mmol) (2.25 M TOPSe stock solution) were prepared under a dry N_2 atmosphere inside a glove box. TOPS and TOPSe solutions were mixed in varying ratios to make different injection solutions (2.25 M TOP-chalcogen). *General synthesis procedure.* CdO (105.0 mg, 0.810 mmol), TOPO (1.375 g, 3.56 mmol) and ODPA (535 mg, 0.937 mmol) were weighed onto a three-neck round bottom (RB) flask. The flask was fitted with a glass-coated stir bar, a condenser and a stainless steel thermocouple. The apparatus was sealed and brought onto an Schlenk line. Using a heating mantle, the mixture was heated to 100°C and evacuated under vacuum for 15 min, refilled with argon and heated to 320°C to form a completely colorless solution. The solution was cooled to 120°C and evacuated under vacuum for 15 min, refilled with argon and heated back to 320°C. When the temperature reached 300°C, TOP (1.20 ml, 2.69 mmol) was injected into the flask. When the temperature reached 320°C, a mixture of TOPS and TOPSe (1 mL total

volume, 2.25 mmol total chalcogens) was rapidly injected, causing a gradual color change. Upon injection, the temperature was allowed to equilibrate at 315°C and kept constant for a total reaction time of 85 minutes. The final reaction mixture was removed from the heating mantle and cooled to room temperature. After dilution with toluene (5 mL), nanocrystals were isolated by addition of a $1{:}1^{v}/_{v}$ iso-propanol/nonanoic acid mixture (24 mL), followed by centrifugation (5,000 rpm for 10 min).

Mechanistic experiments. *Time evolution.* We used the general synthetic procedure above starting from CdO (105.0 mg, 0.810 mmol), TOPO (1.375 g, 3.56 mmol), ODPA (535 mg, 0.937 mmol), and TOP (1.20 ml, 2.69 mmol), using a mixture of TOPS (0.95 ml, 2.1375 mmol) and TOPSe (0.05 ml, 0.1125 mmol) as chalcogenide injection solution (5% Se loading). We repeated this procedure stopping the reaction at different times by removing the heating mantle and cooling to room temperature. Products were isolated as described above. *Reaction of CdSe nanorods with Cd-phosphonate and TOPS.* We first prepared pure CdSe nanorods by the general synthetic procedure starting from CdO (105.0 mg, 0.810 mmol), TOPO (1.375 g, 3.56 mmol), ODPA (535 mg, 0.937 mmol), TOP (1.20 ml, 2.69 mmol), and using TOPSe (1.00 ml, 2.25 mmol). The reaction was stopped after 85 min and products were isolated as described in the general synthetic procedure above. Isolated CdSe nanorods were dissolved in toluene (3 mL), transferred to a new three-neck RB flask, and the solvent removed under vacuum. In a separate flask, CdO (105.0 mg, 0.810 mmol), TOPO (1.375 g, 3.56 mmol) and ODPA (535 mg, 0.937 mmol) were weighed, heated to 100°C and evacuated under vacuum for 15 min, refilled with argon and heated to 320°C to form a completely colorless solution. The solution was allowed to cool to 120°C, evacuated under vacuum for 15 min, refilled with argon, and transferred to the flask containing the CdSe nanorods *via*

syringe. The mixture of Cd-phosphonate precursor and CdSe nanorods was heated to 320°C. When the temperature reached 300°C, TOP (1.20 ml, 2.69 mmol) was injected into the flask. When the temperature reached 320°C, a solution of TOPS (1 mL, 2.25 mmol) was rapidly injected. Upon injection, the temperature was allowed to equilibrate at 315°C and kept constant for a total reaction time of 85 minutes. Products were isolated as described above. *Reaction of CdS nanorods with TOPSe.* We first prepared pure CdS nanorods[9] by the general synthetic procedure above starting from CdO (105.0 mg, 0.810 mmol), TOPO (1.375 g, 3.56 mmol), ODPA (535 mg, 0.937 mmol), and TOP (1.20 ml, 2.69 mmol), and using TOPS (1.00 ml, 2.25 mmol). The reaction was stopped after 85 min and products isolated as described above. Isolated CdS nanorods were transferred to a three-neck RB flask containing TOPO (1.375 g, 3.56 mmol). The mixture was heated to 100°C and evacuated for 15 minutes, refilled with Argon and heated to 320°C. At this temperature a mixture containing TOP (1.2 ml, 3.56 mmol) and TOPSe (0.05 ml, 0.1125 mmol) was rapidly injected. The temperature was allowed to equilibrate at 315°C and kept constant for a total reaction time of 85 minutes. Products were isolated as described above.

Synthesis of $CdS_{0.42}Se_{0.58}$-Pd heterostructures. $CdS_{0.42}Se_{0.58}$ nanorods obtained with a 10% Se loading were dissolved and diluted in toluene to give an optical density (absorbance) of 1.3 at 630 nm. A 2.0 mL volume of this solution was degassed, refilled with dry argon, and stored in the dark for 12 h in a re-sealable Schlenk tube. Under a dry atmosphere, $(TMEDA)PdMe_2$ (30.0 mg, 0.118 mmol) was dissolved in anhydrous toluene (1 mL), and added to $CdS_{1-x}Se_x$ nanorod solution *via* syringe along with triethylamine (0.5 mL, used as terminal electron donor).[71] Deposition was carried out for 1-3 h photochemically at R.T. in a Rayonet® photoreactor containing 16 side-on fluorescent lamps (575 nm/75 nm fwhm).

Products were purified twice by precipation with methanol (30 mL) and centrifugation (5,000 rpm for 10 min). All products could be redispersed in toluene.

Structural characterization. *X-Ray Diffraction.* Powder X-ray diffraction (XRD) data were measured using Cu-Kα radiation on a Scintag XDS-2000 diffractometer equipped with a theta-theta goniometer, a sealed-tube solid-state generator, and an air-cooled Kevex Psi Peltier silicon detector. *Transmission Electron Microscopy.* Transmission electron microscopy (TEM) of samples was conducted on carbon-coated copper grids using a FEI Technai G2 F20 Field Emission scanning transmission electron microscope (STEM) at 200 kV (point-to-point resolution <0.25 nm, line-to-line resolution <0.10 nm). Nanorods' elemental axial composition was characterized by energy dispersive spectroscopy (EDS) line scans in STEM mode, and by energy-filtered (EF) imaging spectroscopy (EF-TEM). *Particle analysis.* Dimensions were measured manually and/or by using ImageJ. Size measurements and particle counts/statistics were obtained for at least >50-100 $CdS_{1-x}Se_x$ and Pd particles. Average sizes are reported along with ±standard deviations. For axially anisotropic nanorods, we report two diameters: 'Head' diameter is the largest observed diameter. 'Tail' diameter is mid-point on thinner half of nanorods.

Optical characterization. Absorption spectra were measured with a photodiode-array Agilent 8453 UV-Vis spectrophotometer. Solvent absorption was recorded and substracted from all spectra. Steady state photoluminescence (PL) spectra were measured with a Horiba-Jobin Yvon Nanolog scanning spectrofluorometer equipped with a photomultiplier detector. Photoluminescence (PL) quantum yields (QYs) were measured following literature procedures.[80] Nanorod samples were diluted in hexane or toluene to give an optical density of 0.05-0.2 at 510 nm. Their PL emission was compared to rhodamine 590 in methanol, with

QY=95%. Excitation wavelength was 510 nm and emission was recorded between 525-800 nm. QYs were calculated as: $QY_{QD} = 0.95 \times (OD_{rhodamine590}/OD_{QD}) \times (PLarea_{QD}/PLarea_{rhodamine590}) \times (RI_{QD}^2/RI_{rhodamine590}^2)$, where $RI_{rhodamine590}$ was taken as the refractive index of methanol (1.3288), and RI_{QD} as the refractive index of toluene (1.4941). Absorption and PL emission spectra of QD and dye samples were measured at least twice and average QYs recorded.

Acknowledgments

This research was supported by the U.S. Department of Energy, Office of Basic Energy Sciences, Division of Chemical Sciences, Geosciences, and Biosciences, through the Ames Laboratory. The Ames Laboratory is operated for the U.S. Department of Energy by Iowa State University under Contract No. DE-AC02-07CH11358. The document number assigned to this thesis/dissertation is IS-T 3100. We thank Iowa State University, the U.S. Department of Energy Ames Laboratory Royalty Account, and the Institute for Physical Research and Technology (IPRT) for laboratory startup funds (J.V.), Yijun Guo for assistance with PL measurements, and John Corbett and Gordon Miller for helpful discussions.

References

[1] Talapin, D. V.; Lee, J.-S.; Kovalenko, M. V.; Shevchenko, E. V. *Chem. Rev.* **2010**, *110*, 389-458.

[2] Hochbaum, A. I.; Yang, P. *Chem. Rev.* **2010**, *110*, 527-546.

[3] Wang, F.; Dong, A.; Sun, J.; Tang, R.; Yu, H.; Buhro, W. E. *Inorg. Chem.* **2006**, *45*, 7511-7521.

[4] Kuno, M. *Phys. Chem. Chem. Phys.* **2008**, *10*, 620-639.

[5] Hu, J.; Odoc, T. W.; Lieber, C. M. *Acc. Chem. Res.* **1999**, *32*, 435-445.

[6] Lu, W.; Lieber, C. M. *J. Phys. D: Appl. Phys.* **2006**, *39*, R387-R406.

[7] Fan, H. J.; Werner, P.; Zacharias, M. *Small* **2006**, *2*, 700-717.

[8] Peng, X. G.; Manna, L.; Yang, W. D.; Wickham, J.; Scher, E.; Kadavanich, A.; Alivisatos, A. P. *Nature* **2000**, *404*, 59-61.

[9] Robinson, R. D.; Sadtler, B.; Demkencho, D. O.; Erdonmez, C. K.; Alivisatos, A. P. *Science* **2007,** *317*, 355-358.

[10] Sadtler, B.; Demchenko, D. O.; Zheng, H.; Hughes, S. M.; Merkle, M. G.; Dahmen, U.; Wang, L. W.; Alivisatos, A. P. *J. Am. Chem. Soc.* **2009**, *131*, 5285-5293.

[11] Peng, Z. A.; Peng, X. *J. Am. Chem. Soc.* **2001**, *123*, 183-184.

[12] Jun, Y.; Lee, S.; Kang, N.; Cheon, J. *J. Am. Chem. Soc.* **2001,** *123*, 5150-5151.

[13] Saunders, A. E.; Ghezelbash, A.; Sood, P.; Korgel, B. A. *Langmuir* **2008**, *24*, 9043-9049.

[14] Sapra, S.; Poppe, J.; Eychmüller. A. *Small* **2007**, *3*, 1186-1888.

[15] Peng, Z. A.; Peng, X. *J. Am. Chem. Soc.* **2002**, *124*, 3343-3353.

[16] Felice, S.; Saunders, A. E.; Korgel, B. A. *J. Phys. Chem. B* **2005**, *109*, 8539-8542.

[17] Manna, L.; Scher, E. C.; Alivisatos, A. P. *J. Am. Chem. Soc.* **2000,** *122*, 12700-12706.

[18] Huang, J.; Kovalenko, M. V.; Talapin, D. V. *J. Am. Chem. Soc.* **2010**, *132*, 15866-15868.

[19] Wang, W.; Banerjee, S.; Jia, S.; Steigerwald, M. L.; Herman, I. P. *Chem. Mater.* **2007**, *19*, 2573-2580.

[20] Manna, L.; Wang, L. W.; Cingolani, R.; Alivisatos, A. P. *J. Phys. Chem. B* **2005**, *109*, 6183-6192.

[21] Peng, X. A.; Peng, X. *J. Am. Chem. Soc.* **2001,** *123*, 1389-1395.

[22] Talapin, D. V.; Shevchenko, E. V.; Murray, C. B.; Kornowski, A.; Förster, S.; Weller, H. *J. Am. Chem. Soc.* **2004**, *126*, 12984-12988.

[23] Li, L.-S.; Alivisatos, A. P. *Phys. Rev. Lett.* **2003**, *90*, 097402-1-097402-4.

[24] Blanton, S. A.; Leheny, R. L.; Hines, M. A.; Guyot-Sionnest, P. *Phys. Rev. Lett.* **1997**, *79*, 865-868.

[25] Swafford, L. A.; Weigand, L. A.; Bowers, M. J., II; McBride, J. R.; Rapaport, J. L.; Watt, T. L.; Dixit, S. K.; Feldman, L. C.; Rosenthal, S. J. *J. Am. Chem. Soc.* **2006**, *128*, 12299-12306.

[26] Zou, Y.; Li, D.; Yang, D. *Nanoscale Res. Lett.* **2010**, *5*, 966-971.

[27] Ouyang, J.; Vincent, M.; Kingston, D.; Descours, P.; Boivineau, T.; Zaman, M. B.; Wu, X.; Yu, K. *J. Phys. Chem. C* **2009,** *113*, 5193-5200.

[28] Jang, E.; Jun, S.; Pu, L. *Chem. Commun.* **2003**, 2964-2965.

[29] Bailey, R. E.; Nie, S. *J. Am. Chem. Soc.* **2003**, *125*, 7100-7106.

[30] Smith, A. M.; Nie, S. *J. Am. Chem. Soc.* **2011**, *133*, 24-26.

[31] Van Embden, J.; Jasieniak, J.; Mulvaney, P. *J. Am. Chem. Soc.* **2009**, *131*, 14299-14309.

[32] Li, J. J.; Wang, Y. A.; Guo, W.; Keay, J. C.; Mishima, T. D.; Johnson, M. B.; Peng, X. *J. Am. Chem. Soc.* **2003**, *125*, 12567-12575.

[33] Mahler, B.; Lequeux, N.; Dubertret, B. *J. Am. Chem. Soc.* **2010**, *132*, 953-959.

[34] Vela, J.; Htoon, H.; Chen, Y.; Park, Y.-S.; Ghosh, Y.; Goodwin, P.; Werner, J.; Wells, N. P.; Casson, J. L.; Hollingsworth, J. A. *J. Biophoton.* **2010**, *3*, 706-717.

[35] Bao, H.; Gong, Y.; Li, Z.; Gao, M. *Chem. Mater.* **2004**, *16*, 3853-3859.

[36] Smith, A. M.; Mohs, A. M.; Nie, S. *Nature Nanotechnol.* **2009**, *4*, 56-63.

[37] Dabbousi, B. O.; Rodriguez-Viejo, J.; Mikulec, F. V.; Heine, J. R.; Mattoussi, H.; Ober, R.; Jensen, K. F.; Bawendi, M. G. *J. Phys. Chem.* **1997**, *101*, 9463-9475.

[38] Talapin, D.V.; Rogach, A.L.; Kornowski, A.; Haase, M.; Weller, H. *Nano Lett.* **2001**, *1*, 207-211.

[39] Malik, M.A.; O'Brien, P.; Revaprasadu, N. *Chem. Mater.* **2002**, *14*, 2004-2010.

[40] Hines, M. A.; Guyot-Sionnest, P. *J. Phys. Chem.* **1996**, *100*, 468-471.

[41] Reiss, P.; Bleuse, J; Pron, A. *Nano Lett.* **2002**, *2*, 781-784.

[42] Xie, R.; Kolb, U.; Li, J.; Basché, T.; Mews, A. *J. Am. Chem. Soc.* **2005**, *127*, 7480-7488.

[43] Carbone, L.; Nobile, C.; De Giorgi, M.; Della Sala, F.; Morello, G.; Pompa, P.; Hytch, M.; Snoeck, E.; Fiore, A.; Franchini, I. R. *et al. Nano Lett.* **2007**, *7*, 2942-2950.

[44] Zou, Y.; Li, D.; Yang, D. *J. Cryst. Growth* **2010**, *312*, 3406-3409.

[45] Talapin, D. V.; Nelson, J. H.; Shevchenko, E. V.; Aloni, S.; Sadtler, B.; Alivisatos, A. P. *Nano Lett.* **2007,** *7*, 2951-2959.

[46] Gross, D.; Susha, A. S.; Klar, T. A.; Da Como, E.; Rogach, A. L.; Feldmann, J. *Nano Lett.* **2008**, *8*, 1482-1485.

[47] Halpert, J. E.; Porter, V. J.; Zimmer, J. P.; Bawendi, M. G. *J. Am. Chem. Soc.* **2006**, *128*, 12590-12591.

[48] McBride, J.; Treadway, J.; Feldman, L. C.; Pennycook, S. J.; Rosenthal, S. J. *Nano Lett.* **2006**, *6*, 1496-1451.

[49] Koo, B.; Korgel, B. A. *Nano Lett.* **2008**, *8*, 2490-2496.

[50] Tang, B.; Yang, F.; Lin, Y.; Zhuo, L.; Ge, J.; Cao, L. *Chem. Mater.* **2007**, *19*, 1212-1214.

[51] Liang, Y.; Zhai, L.; Zhao, X.; Xu, D. *J. Phys. Chem. B* **2005**, *109*, 7120-7123.

[52] Pan, A.; Yang, H.; Liu, R.; Yu, R.; Zou, B.; Wang, Z. *J. Am. Chem. Soc.* **2005**, *127*, 15692-15693.

[53] Ouyang, L.; Maher, K. N.; Yu, C. L.; McCarty, J.; Park, H. *J. Am. Chem. Soc.* **2007**, *129*, 133-138.

[54] Dong, A.; Tang, R.; Buhro, W. E. *J. Am. Chem. Soc.* **2007**, *129*, 12254-12262.

[55] Zhong, H.; Scholes, G. D. *J. Am. Chem. Soc.* **2009**, *131*, 9170-9171.

[56] Li, Y.; Zhong, H.; Li, R.; Zhou, Y.; Yang, Z.; Li, Y. *Adv. Funct. Mater.* **2006**, *16*, 1705-1716.

[57] Peng, X. *Adv. Mater.* **2003**, *15*, 459-463.

[58] Gunlach L.; Piotrowiak, P. *J. Phys. Chem. C* **2009**, *113*, 12162-12166.

[59] Joo, J.; Son, J. S.; Kwon, S. G.; Yu, J. H.; Hyeon, T. *J. Am. Chem. Soc.* **2006**, *128*, 17, 5632-5633.

[60] Pacholski, C.; Kornowski, A.; Weller, H. *Angew. Chem. Int. Ed.* **2004**, *43*, 4774-4777.

[61] Costi, R.; Saunders, A. E.; Banin, U. *Angew. Chem. Int. Ed.* **2010**, *49*, 4878-4897.

[62] Habas, S. E.; Yang, P.; Mokari, T. *J. Am. Chem. Soc.* **2008**, *130*, 3294-3295.

[63] Chan, S. C.; Barteau, M. A. *Langmuir* **2005**, *21*, 5588-5595.

[64] Kudera, S.; Carbone, L.; Casula, M. F.; Cingolani, R.; Falqui, A.; Snoeck, E.; Parak, W. J.; Manna, L. *Nano Lett.* **2005**, *5*, 445-449.

[65] Kwon, K.-W.; Lee, B. H.; Shim, M. *Chem. Mater.* **2006**, *18*, 6357-6363.

[66] Kwon, K.-W.; Shim, M. *J. Am. Chem. Soc.* **2005**, *127*, 10269-10257.

[67] Gao, J.; Zhang, B.; Gao, Y.; Pan, Y.; Zhang, X.; Xu, B. *J. Am. Chem. Soc.* **2007**, *129*, 11928-11935.

[68] Menagen, G.; Macdonald, J. E.; Shemesh, Y.; Popov, I.; Banin, U. *J. Am. Chem. Soc.* **2009**, *131*, 17406-17411.

[69] Chakrabortty, S.; Yang, J. A.; Tan, Y. M.; Mishra, N.; Chan, Y. *Angew. Chem. Int. Ed.* **2010**, *49*, 1-6.

[70] Elmalem, E.; Saunders, A.E.; Costi, R.; Salant, A.; Banin, U. *Adv. Mater.* **2008**, *20*, 4312-4317.

[71] Dukovic, G.; Merkle, M. G.; Nelson, J. H.; Hughes, S. M.; Alivisatos, A. P. *Adv. Mater.* **2008**, *20*, 4306-4311.

[72] Cozzoli, P. D.; Pellegrino, T.; Manna, L. *Chem. Soc. Rev.* **2006**, *35*, 1195-1208.

[73] Shi, W.; Sahoo, Y.; Zeng, H.; Ding, Y.; Swihart, M. T.; Prasad, P. N. *Adv. Mater.* **2006**, *18*, 1889-1894.

[74] Shemesh, Y.; Macdonald, J. E.; Menagen, G.; Banin, U. *Angew. Chem. Int. Ed.* **2011**, *50*, 1185-1189.

[75] Maynadié, J.; Salant, A.; Falqui, A.; Respaud, M.; Shaviv, E.; Banin, U.; Soulantica, K.; Chaudret, B. *Angew. Chem. Int. Ed.* **2009**, *48*, 1814—1817.

[76] Deka, S.; Falqui, A.; Bertoni, G.; Sangregorio, C.; Poneti, G.; Morello, G.; De Giorgi, M.; Giannini, C.; Cingolani, C.; Manna, L. *et al.* *J. Am. Chem. Soc.* **2009**, *131*, 12817-12828.

[77] Vegard, L. *Z. Krystallogr.* **1928**, *67*, 239-259.

[78] Xu, F.; Rock, P. A.; Ma, X.; Kauzlarich, S. M.; Navrotsky, A. *J. Mater. Res.* **2009**, *24*, 1368-1374.

[79] McDonough, J. E.; Mendiratta, A.; Curley, J. J.; Fortman, G. C.; Fantasia, S.; Cummins, C. C.; Rybak-Akimova, E. V.; Nolan, S. P.; Hoff, C. D. *Inorg. Chem.* **2008**, *47*, 2133-2141.

[80] Grabolle, M.; Spieles, M.; Lesnyak, V.; Gaponik, N.; Eychmüller, A.; Resch-Genger, U. *Anal. Chem.* **2009**, *81*, 6285-6294.

CHAPTER 3

MOLECULAR CONTROL OF THE NANOSCALE: EFFECT OF PHOSPHINE CHALCOGENIDE REACTIVITY ON CdS-CdSe NANOCRYSTAL COMPOSITION AND MORPHOLOGY

Reprinted with permission from **2012**, *6*, 5348.

T. Purnima A. Ruberu, Haley R. Albright, Brandon Callis, Brittney Ward, Joana Cisneros, Hua-Jun Fan, Javier Vela

Abstract

We demonstrate molecular control of nanoscale composition, alloying, and morphology (aspect ratio) in CdS-CdSe nanocrystal dots and rods by modulating the chemical reactivity of phosphine-chalcogenide precursors. Specific molecular precursors studied were sulfides and selenides of triphenylphosphite (TPP), diphenylpropylphosphine (DPP), tributylphosphine (TBP), trioctylphosphine (TOP), and hexaethylphosphoroustriamide (HPT). Computational (DFT), NMR (^{31}P and ^{77}Se), and high temperature crossover studies unambiguously confirm a chemical bonding interaction between phosphorous and chalcogen atoms in all precursors. Phosphine-chalcogenide precursor reactivity decreases in the order: TPPE > DPPE > TBPE > TOPE > HPTE (E = Se > S). For a given phosphine, the selenide is always more reactive than the sulfide. $CdS_{1-x}Se_x$ quantum dots were synthesized via single injection of a R_3PS-R_3PSe mixture to cadmium-oleate at 250°C. X-Ray diffraction (XRD), transmission electron microscopy (TEM), and UV/Vis and PL optical spectroscopy reveal

relative R_3PS and R_3PSe reactivity dictates $CdS_{1-x}Se_x$ dot chalcogen content and extent of radial alloying (alloys vs. core/shells). CdS, CdSe, and $CdS_{1-x}Se_x$ quantum rods were synthesized by injection of a single R_3PE (E = S or Se) precursor or a R_3PS–R_3PSe mixture to cadmium phosphonate at 320°C or 250°C. XRD and TEM reveal the length-to-diameter aspect ratio of CdS and CdSe nanorods is inversely proportional to R_3PE precursor reactivity. Purposely matching or mismatching R_3PS-R_3PSe precursor reactivity leads to $CdS_{1-x}Se_x$ nanorods without or with axial composition gradients, respectively. We expect these observations will lead to scalable and highly predictable "bottom-up" programmed syntheses of finely hetero-structured nanomaterials with well-defined architectures and properties that are tailored for precise applications.

Introduction

Preparative nanotechnology or "nano-manufacturing" is rapidly evolving toward fabrication of ever more complex materials with precise structure and properties. Tuning composition, relative configuration and spatial arrangement of hetero-structured nanomaterials can impact our ability to engineer and direct energy flows at the nanoscale. In the case of II-VI and IV-VI semiconductors, composition control has been demonstrated for homogeneously alloyed $CdS_{1-x}Se_x$,[1-4] $CdS_{1-x}Te_x$,[5] $CdSe_{1-x}Te_x$,[6] PbS_xSe_{1-x}, PbS_xTe_{1-x} and $PbSe_xTe_{1-x}$[7] nanocrystals with size- and composition-tunable band gaps.[4,8,9] In some cases, a nonlinear relationship between composition and absorption/emission energies, called optical bowing, resulted in new properties not obtainable from the parent binary systems.[3] For example, CdS_xTe_{1-x} nanocrystals displayed small absorption–emission spectral overlap, up to 150 nm Stokes shifts, and significantly red-shifted PL with respect to CdS and CdTe nanocrystals.[5]

Controlling nanocrystal morphology is key to controlling nanocrystal proper-ties.[10-14] A common technique to produce nanorods, for example, is to perform slow and/or subsequent reactant injections.[15-17] In intrinsically anisotropic systems such as hexagonal (wurtzite) II-VI semiconductors, unidirectional (nanorod) growth occurs along the c(z) axis under high precursor concentrations. Bulky cadmium-phosphonate complexes are known to maintain high precursor concentrations via controlled release of Cd^{2+} ions to the medium.[18] Nearly spherical to rod-like shapes are produced using ligands such as hexylphosphonic acid.[19] Aspect ratio is sensitive to phosphonic acid alkyl chain length; the shorter the chain, the more elongated and branched are the nanorods.[18,20] Aspect ratio control has been studied for ZnS, ZnSe,[16,21] ZnTe, CdS,[15] CdSe,[17-19] CdTe, $ZnS_{1-x-y}Se_xTe_y$ and $CdSe_{1-x}Te_x$[22] nanorods. ZnTe aspect ratio was controlled by temperature-tuning nanocrystal growth kinetics.[23] Composition-tunable CdSe, CdTe and $CdSe_xTe_{1-x}$ tetrapods, the latter with nonlinear composition-dependent absorption and emission and spectral coverage up to 1000 nm (near-IR), were also reported.[22]

The mechanism by which cationic and phosphine-chalcogenide precursors react to form II-VI and IV-VI nanocrystals is currently under intense study and debate.[24,25] Two mechanisms, one involving Se^{2-} and another involving Se^0 transfer, were found to be simultaneously responsible for PbSe nanocrystal formation from Pb(oleate)2 and phosphine-selenides.[26] A kinetic model was used to describe combined nanocrystal nucleation and growth phenomena.[27] Reaction of $Pb(oleate)_2$ and trioctylphosphine selenide (TOPSe) at low temperature produced spherical PbSe nanocrystals, while reaction with hexaethylphosphorous-triamide (HPT, also called tris(diethylamino)-phosphine selenide) at

high temperature produced PbSe nanorods. Coupled thermo gravimetric-mass spectrometry analysis (TGA-MS) showed HPT accelerates precursor decomposition by releasing amines.[28]

Trioctyl- and tributyl-phosphine chalcogenides (TOPE and TBPE; E = S, Se, Te) react with Cd and Zn oleates or alkylphosphonates via a Lewis acid-substitution mechanism, producing ME (M = Cd, Zn) nanocrystals, phosphine oxides (TOPO or TBPO) and oleic or phosphonic anhydrides.[29] Using a high throughput synthesis platform, CdSe yield as well as nucleation and growth rates from $Cd(ODPA)_2$ in TOPO were found to depend on phosphine selenide concentration and number of aryl groups.[30] Trialkyl-phosphine selenide P=Se bond cleavage starts by nucleophilic attack of carboxylate on Cd^{2+}-activated phosphine selenide, followed by proton transfer from carboxylic acid to Se and Cd-Se bond formation. The rate-limiting step lies at or before formation of acyloxytrialkylphosphonium ion, which was trapped with alcohols.[31] Reaction of DPPSe and $Cd(benzoate)_2$ in dodecylamine proceeds through a diphenyldiselenophosphinate intermediate and generates tetraphenyldiphosphine as a byproduct.[32] Magic-sized CdSe clusters are thought to be intermediates during CdSe nanorod synthesis from $Cd(phosphonate)_2$ and TOPSe in TOP-TOPO. Interestingly, acidic impurities accelerate reaction rates when technical grade rather than pure TOPO is used.[33] Tertiaryphosphine selenide sources such as TOPSe were recently proposed to be unreactive toward metal carboxylates; small quantities of secondary phosphine impurities were proposed to be responsible for nanocrystal nucleation.[34] Whether this effect is catalytic or stoichiometric remains unknown.

In this paper, we use a combined experimental and theoretical approach to demonstrate molecular precursor reactivity determines the relative ease of formation between nanocrystal phases. This opens new avenues for achieving predictable, molecular-level or “bottom-up”

control of nanoscale-composition and morphology. Based on our recent observation of spontaneous formation of compositionally graded nanorods, this idea is consistent with Hammond's postulate, whereby the transition state energy for the rate determining step, nucleation, is closest in energy to the precursors rather than to the much more stable nanocrystalline products, effectively a thermodynamic sink. We specifically focus on tuning sterics and electronics and therefore altering reactivity of different phosphine chalcogenides (sulfides and selenides) in order to control architecture, composition and aspect ratio of CdS-CdSe colloidal nanocrystals (dots and rods).

Results and Discussion

Initial observation: Spontaneous formation of composition-graded, axially-anisotropic $CdS_{1-x}Se_x$ nanorods.[35] Using a single injection of premixed trioctyl-phosphine sulfur (TOPS) and trioctyl-phosphine selenium (TOPSe) to a bis(phosphonate)-cadmium $Cd(ODPA)_2$ complex at 320°C, we recently synthesized axially anisotropic $CdS_{1-x}Se_x$ nanorods having a thick “head” and a thin “tail” (Scheme 1).[38] X-ray dif-fraction (XRD), high-resolution (HR) and energy-filtered (EF) transmission electron microscopy (TEM), and energy-dispersive X-ray spectroscopy (EDS) showed nanorod heads are CdSe-rich, whereas nanorod tails are CdS-rich.[35] This axial anisotropy and composition gradient is accompanied by a marked band-gap differential, and allows directing metal (Pt, Pd) nanoparticle photodeposition toward either side of $CdS_{0.42}Se_{0.58}$ nanorods by changing irradiation wavelength.[36]

Time evolution and mechanistic studies showed $CdS_{1-x}Se_x$ nanorods form sequentially, starting with quick CdSe head nucleation (<20 min), followed by slow CdS tail growth (~85 min) (Scheme 1). The relative ease of formation between these two nanorod segments cannot be a consequence of relative crystalline energies: CdS is much more stable (m.p. 1748°C,

lattice energy ~834 kcal/mol) compared to CdSe (m.p. 1512°C, lattice energy ~798 kcal/mol).[35, 37] Instead, this must be a consequence of relative TOPS vs. TOPSe precursor reactivity. This idea is consistent with Hammond's postulate,[38] whereby the transition state energy for the rate determining step, nucleation, is closest to the precursors than to the much more stable crystalline nanorods, effectively a thermodynamic sink.[39] If true, this could open new avenues for achieving molecular-level or "bottom-up" control of nanoscale-composition and morphology. By tuning sterics and electronics and therefore altering molecular precursor reactivity, one could control relative formation rates of different nanocrystalline phases.

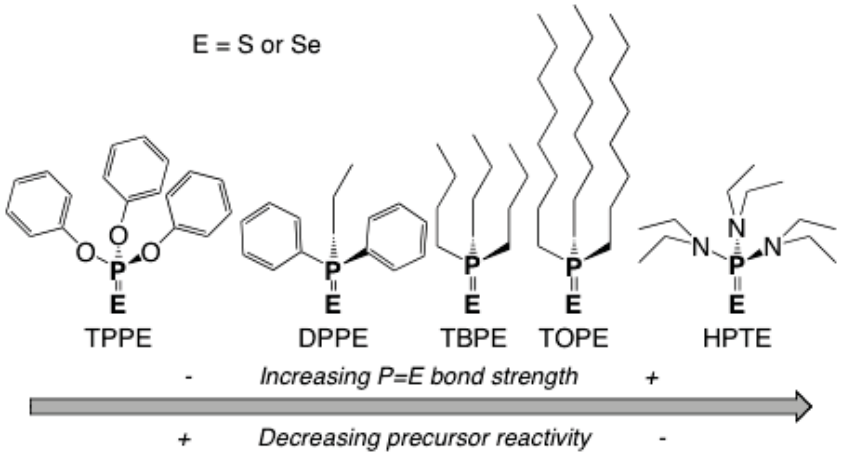

Figure 1. Phosphine-chalcogenide precursors used in this study.

Here, we focused our attention on the reactivity of chalcogenide (sulfide and selenide) derivatives, $R_3P=E$, of five commercially available phosphines, R_3P: Triphenylphosphite (TPP), diphenylpropylphosphine (DPP), tributylphosphine (TBP), trioctylphosphine (TOP), and hexaethyl-phosphorous-triamide (HPT) (Figure 1). All of the phosphines in this series are liquid at room temperature (R.T.), which facilitates precursor preparation by chemical "dissolution" of chalcogen (sulfur or selenium). On the contrary, triphenylphosphine, another commercially available phosphine, was not used here because it is a solid at R.T. (m.p. 79-81°C). Qualitatively, we predicted more electron-donating groups would lead to better

stabilization of a partial positive charge on phosphorous, thus to stronger phosphorous-chalcogen (P=E) bonds and less reactive precursors (Figure 1).

Estimating phosphine-chalcogen bond strength and relative precursor reactivity from DFT calculations. To better understand these phenomena, we first turned our attention to computational modeling of the factors that control precursor reactivity at the atomic level. We focused on geometric and electronic properties around the reactive phosphorous-chalcogen bond. Table 1 lists relative energetic parameters, including zero-point energy correction (ΔE°_{ZPE}), enthalpies ($\Delta H°$), and free energies ($\Delta G°$) corrected to R.T. for the reaction $R_3P + S \rightarrow R_3PE$ (E = S or Se). In the optimized geometries, P=S bond lengths slightly increase from TPPS (1.921 Å), to DPPS (1.974 Å), TBPS (1.978 Å), TOPS (1.978 Å), and HPTS (1.982 Å). Similarly, P=Se bond lengths slightly increase from TPPSe (2.073 Å), to DPPSe (2.129 Å), TBPSe (2.131 Å), TOPSe (2.131 Å), and HPTSe (2.141 A). However, we do not believe this is an indication of relative P=E (S, Se) bond strength, but rather a consequence of size and steric bulk of phosphorous substituents as reflected in the cone angles available for three phosphines in the series: TOP (128°), TBP (132°), DPP (136°).[40-43]

Table 1. The relative reaction energetic parameters with zero-point energy correction ($\Delta E°ZPE$), enthalpy ($\Delta H°$) and free energies ($\Delta G°$) corrected to room temperature.

	$\Delta E°$	$\Delta E°_{ZPE}$	$\Delta H°$	$\Delta G°$	$\Delta E°$
Basis set	6-311G*				cc-pVTZ
Sulfides					
TPP+S→TPPS	-76.20	-74.06	-74.87	-64.66	-79.55
DPP+S→DPPS	-75.21	-73.35	-74.01	-63.91	-80.03

Table 1 continued

TBP+S→TBPS	-79.88	-77.71	-78.41	-68.38	-83.42
TOP+S→TOPS	-82.86	-80.99	-81.57	-71.60	-86.95
HPT+S→HPTS	-89.77	-86.71	-87.57	-77.60	-91.78
Selenides					
TPP+Se→TPPSe	-62.42	-60.84	-61.40	-51.67	-63.77
DPP+Se→DPPSe	-62.96	-61.63	-62.07	-52.10	-65.98
TBP+Se→TBPSe	-67.04	-65.43	-65.87	-56.23	-69.75
TOP+Se→TOPSe	-70.07	-68.60	-68.99	-59.10	-72.98
HPT+Se→HPTSe	-76.81	-74.38	-75.00	-65.22	-77.52

From Table 1, chalcogenide (E = S or Se) formation is exothermic or "downhill" ($\Delta G°<0$), i.e. all phosphine-chalcogenides (R_3PE) are thermo-dynamically more stable than the reactants (R_3P + E). We believe the negative values $-\Delta G°$ or $-\Delta E°$ are good predictors of relative P=E bond strength and precursor reactivity. For example, calculated $-\Delta E°$ values for trioctyl-phosphine (TOP) sulfide and selenide are ~87 kcal/mol and ~73 kcal/mol, respectively. These values roughly agree with previous results, which gave P=S and P=Se bond strengths of 96 kcal/mol and 75 kcal/mol, respectively.44 The $\Delta E°$ difference between two phosphine-chalcogenides at the end of the series, TPPE and HPTE is ~13 kcal/mol for S and ~14 kcal/mol for Se (solvation increases this difference to ~23 kcal/mol for S and ~16 kcal/mol for Se, see Supporting Information). Both $-\Delta G°$ and $-\Delta E°$ calculations clearly show phosphine-chalcogenide stability relative to the release of free phosphine and chalcogen increases in the order: TPPE ~ DPPE < TBPE < TOPE < HPTE. Single point energy $\Delta E°$ results using optimized geometries with 6-311G* and cc-pVTZ basis sets mirror this trend. Phosphine-chalcogenide precursor reactivity, understood as the ability to give off or release

chalcogen, significantly decreases in the order: TPPE ~ DPPE > TBPE > TOPE > HPTE (E = S, Se). This trend explains our afore-mentioned sequential formation of axially anisotropic $CdS_{1-x}Se_x$ nanorods: Because of significantly weaker P=E bond in TOPSe compared to TOPS (by 21 kcal/mol, Table 1), Cd(ODPA)2 reacts faster with TOPSe than with TOPS, leading to faster CdSe nucleation compared to CdS.[35]

Figure 2 shows the highest occupied molecular orbital (HOMO) for HPTE and TPPE (E = S, Se). HOMOs are based on the 1-node p-orbital interaction between P and E, and are π-bond in character. The TPPSe HOMO has a small contribution from phenyl substituents, while the HPTS and HPTSe HOMOs have large amide nitrogen contributions. In TPPE, the oxygen between phenyl and P creates an electron density gap, and the oxygen lone pairs do not facilitate a π-interaction. In HPTE, the amine nitrogen directly connects to P, and the amide groups are situated perfectly for extensive π-interaction with P, making HPT bind S and Se very strongly. Much weaker π-interactions in TPP are observed in atomic polar tensor (APT) atomic popu-lations analysis (unlike Mülliken analysis,[45-47] APT[48] analysis exhibits modest basis set sensitivity and models atomic populations more realistically).[49,50] Both analyses place positive and negative charges on P and E (S or Se), respectively. APT analysis shows a progressive increase of positive P charge upon going from free phosphine to phosphine-chalcogenide. Upon binding to E, APT P charge increases from TPP (0.622, S; 0.528, Se), to DPP (0.979, S; 0.872, Se), TBP (0.846, S; 0.750, Se), TOP (0.867, S; 0.767, Se), and HPT (0.866, S; 0.781, Se). Thus P polarization increases precursor stability; it is lowest for TPP, confirming TPPS and TPPSe as most reactive chalcogen sources in the series (Figure 1).

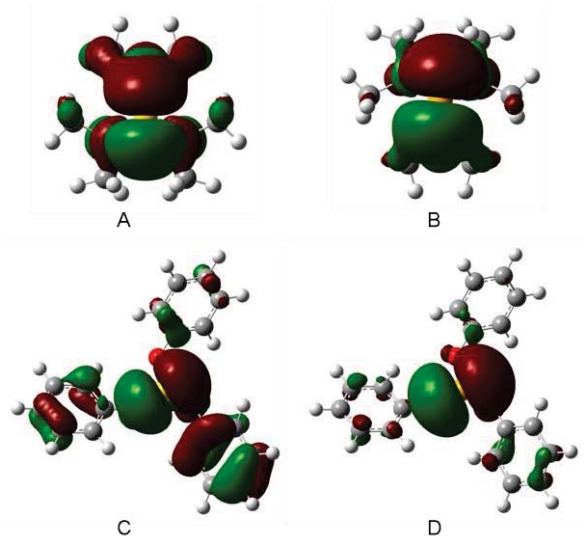

Figure 2. DFT-calculated highest occupied molecular orbitals (HOMO's) for HPTS (a), HPTSe (b), TPPS (c), and TPPSe (d) (viewed down the pseudo-C_3(z) axis). The 1-node π-interaction from the phenyl ring in TPPS is isolated from the P=S π-bond interaction.

Estimating phosphine-chalcogen bond strength and reactivity from ^{31}P and ^{77}Se NMR. We used nuclear magnetic resonance (NMR) spectroscopy to gather experimental evidence that could substantiate these results. Specifically, we measured ^{31}P and ^{77}Se NMR spectra of the different phosphines, phosphine-sulfide and phosphine-selenide precursors (Table 2). Critically, ^{31}P resonances of all phosphine-selenides (R_3PSe) show satellites characteristic of strong ^{31}P coupling (J = 330-520 Hz) to NMR active ^{77}Se (S = 1/2 nucleus with 7.58% natural abundance) (Figure 3a). Similarly, ^{77}Se resonances of all phosphine-selenides (R_3PE) appear as doublets characteristic of strong ^{77}Se coupling to ^{31}P (S = 1/2, 100% natural abundance) (Figure 3b). Observation of this coupling unambiguously corroborates presence of phosphorous-selenium bonds in all selenide precursors; it also indirectly corroborates phosphorous-sulfur bonds in all sulfide precursors because P=S bonds are stronger than corresponding P=Se bonds (Table 1).[44]

Phosphine-chalcogenide (R_3P=Se, R_3P=S) ^{31}P NMR chemical shifts (δ) are more "downfield" (higher δ) compared to parent phosphines (R_3P), indicating P atom becomes more electron deficient upon chalcogenide formation (HPT is the only exception, see

Supporting Information). ^{31}P chemical shifts (δ) reflect relative P=E (S, Se) bond strengths; they correlate well with reported electron-donating abilities of phosphines, as reflected by available pK_a values: TOP (pK_a = 8.4), TBP (pK_a= 8.4), DPP (pK_a =4.9) and TPP (pK_a = 2.0) (TPP is the strongest base because its conjugate acid has the smallest pK_a).[51,52] ^{31}P NMR chemical shifts (δ) also correlate well with relative P=Se and P=S bond energies (-ΔG°'s, Table 1) (HPT is again the exception, see below). Phosphine-sulfide (R_3P=S) ^{31}P δ values are more downfield compared to phosphine-selenide (R_3P=Se) δ values because S is smaller, more electronegative and forms stronger P=E bonds than Se.

Table 2. ^{31}P and ^{77}Se NMR analysis of phosphine-chalcogenides.[a]

	R_3P[b]	R_3PS[b]	R_3PSe[b]	R_3PSe[c]
	^{31}P δ/ppm	^{31}P δ/ppm	^{31}P δ/ppm (J ^{31}P-^{77}Se/Hz)	^{77}Se δ/ppm (J ^{77}Se-^{31}P/Hz)
TPP	128.43 (*s*)	53.65 (*s*)	58.99 (*s*)[d] (513)	291.70 (*d*) (513)
DPP	-16.04 (*s*)	42.89 (*s*)	34.15 (*s*)[d] (360)	342.53 (*d*) (360)
TBP	-30.02 (*s*)	49.39 (*s*)	37.12 (*s*)[d] (339)	381.70 (*d*) (340)
TOP	-30.07 (*s*)	49.28 (*s*)	36.99 (*s*)[d] (339)	390.30 (*d*) (358)
HPT	122.58 (*s*)	82.37 (*s*)	82.21 (*s*)[d] (392)	258.78 (*d*) (386)

[a] *s* = singlet, *d* = doublet. [b]Referenced against 85% phosphoric acid, H_3PO_4 (δ 0 ppm). [c]Referenced against $PPh_3Se/CDCl_3$ (δ -266.20 ppm *vs.* Me_2Se δ 0 ppm). [d] ^{77}Se satellites (7.58%) observed.

Minimizing phosphine-chalcogen exchange: High-temperature crossover experiments. We also probed the tendency of chalcogens to exchange or "crossover" between different phosphines (Scheme 2a). This question is important when two or more phosphine-chalcogenides are used as nanocrystal precursors (Scheme 2b, c); it also serves as an indirect test for the existence of P=S and P=Se bonds at high temperature. Specifically, we performed chalcogen crossover experiments between DPPS and TOPSe to give DPPSe and TOPS. According to Table 1, this exchange reaction is slightly exothermic (favorable), with a $\Delta G° = -0.69$ kcal/mol. Experimentally, we premixed DPPS and TOPSe at R.T., and injected this mixture to a Cd-free solution containing only oleic acid and dioctylamine under argon at different temperatures. Aliquots were drawn at different times, and the extent of chalcogen exchange monitored by ^{31}P NMR. As shown in Figure 4, exchange at R.T. is very slow, with neither DPPSe nor TOPS being observed after 5 min. Exchange at very high temperature, *e.g.* 300°C, is too fast, with as much as half of DPPS and TOPSe converted to DPPSe and TOPS after 5 min.

Scheme 2. High-temperature chalcogen exchange

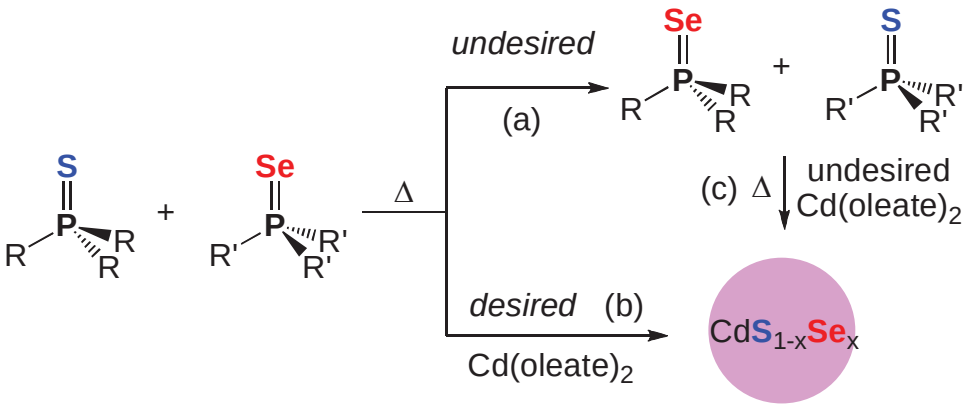

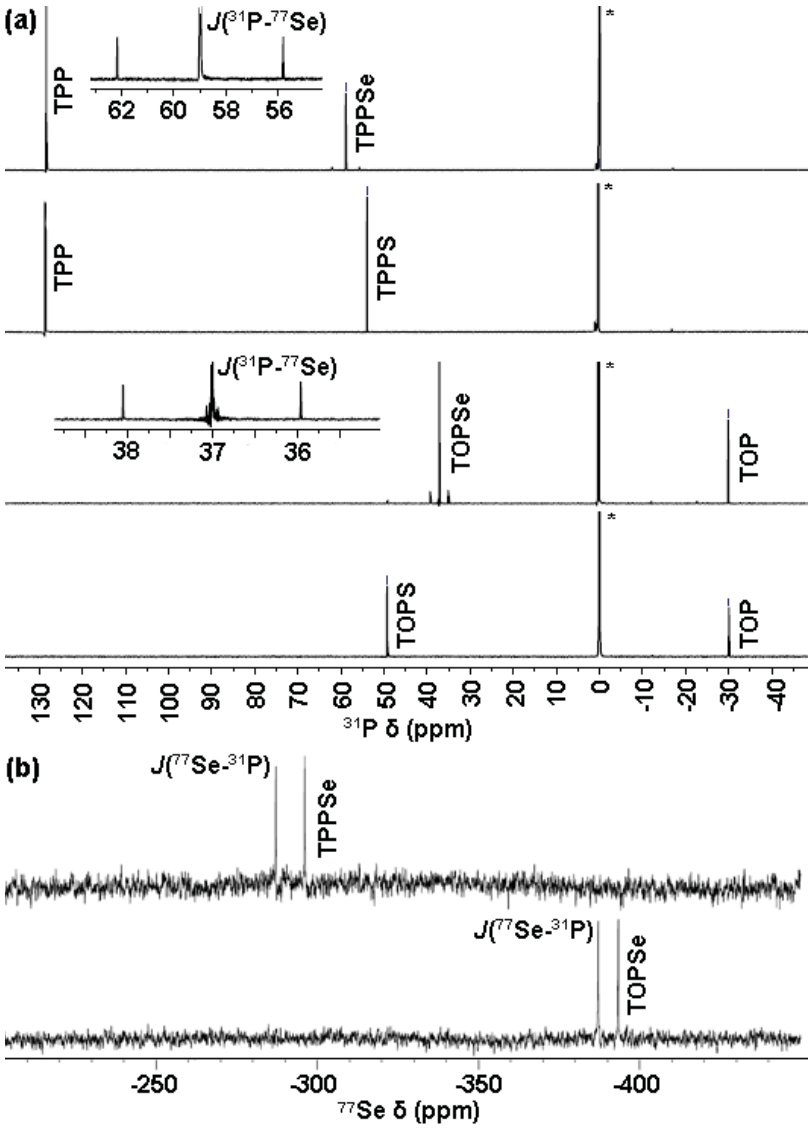

Figure 3. Sample (a) ^{31}P and (b) ^{77}Se NMR spectra of phosphine (R_3P) and phosphine-chalcogenide (R_3PE) precursors (E = S, Se). $J(^{31}P\text{-}^{77}Se)$ coupling (330-520 Hz) is observed for R_3PSe by both ^{31}P and ^{77}Se NMR. * = 85% H_3PO_4 internal standard.

Nevertheless, decreasing temperature somewhat and shortening reaction time helps minimize exchange. At 250°C, the minimum temperature at which we see appreciably reaction between phosphine-chalcogenides and $Cd(oleate)_2$ or $Cd(ODPA)_2$ with immediate nuclei formation, DPPSe is unobserved and TOPS is a minor product after 0.5 min (Figure 4b).

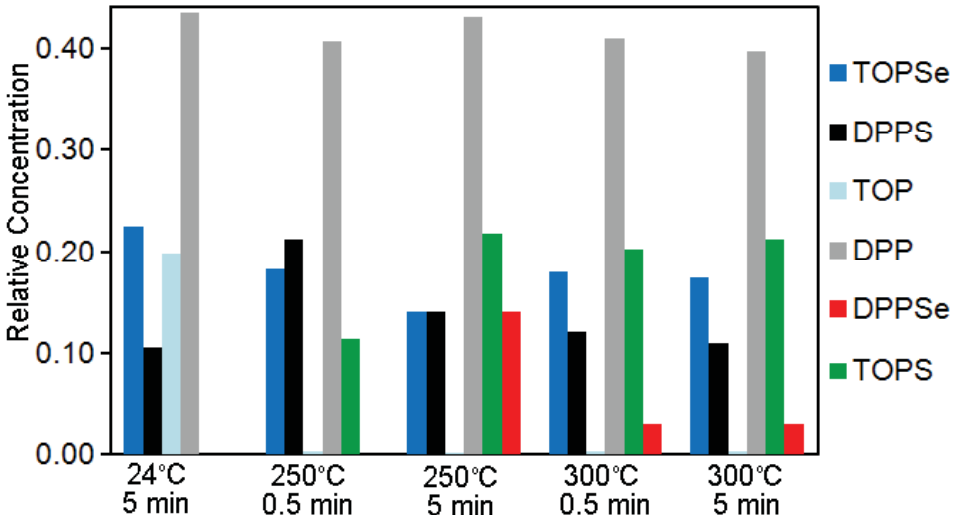

Figure 4. Chalcogen exchange between DPPS and TOPSe as a function of reaction temperature and time monitored by ^{31}P NMR.

Controlling $CdS_{1-x}Se_x$ nanodot composition. Having theoretical and experimental data at hand, we probed the effect of chalcogenide precursor reactivity on nanocrystal composition by synthesizing $CdS_{1-x}Se_x$ nanodots using different phosphine-sulfide (R_3PS) and phosphine-selenide (R'_3PSe) combinations. According to Vegard's Law, [53] complete $CdS_{1-x}Se_x$ solid solutions are possible over whole composition range ($0 \leq x \leq 1$). Both CdS and CdSe form zinc blende (cubic) and wurtzite (hexagonal) crystals, and four-coordinate S^{2-} and Se^{2-} ionic radii differ little, under <15% (4-7%).[54] Specific syntheses involved injecting fresh R_3PS–R'_3PSe mixtures to $Cd(oleate)_2$ at 250°C, keeping the same (growth) temperature for 5 min. After isolation, we examined the resulting dots' optical properties, particle size (diameter) and composition using a combination of UV-Vis absorption and photoluminescence (PL) spectroscopies, XRD, TEM, and EDS (Table 3 and Figure 6).

Table 3. Controlling $CdS_{1-x}Se_x$ nanodot composition.[a]

Precursor mix. (ratio)[a]	$(-\Delta G°_{P=S}) - (-\Delta G°_{P=Se})$[b] /kcal/mol	Particle size/nm XRD[c]	Particle size/nm TEM	Band gap/eV[d]	%S
TOPSe	-	2.2	4.6±1.0	2.18	0
TOPS–TOPSe (3:1)	12.5	3.4	5.2±0.9	2.13	1.8
DPPS–TOPSe (99:1)	4.81	3.2	4.8±0.7	2.09	41
DPPS–TOPSe (199:1)	4.81	3.4	5.1±0.9	2.12	54
TOPS	-	2.6	4.0±0.6	2.80	100

[a]Phosphines premixed at R.T. before injection to $Cd(oleate)_2$ at 250°C; dots grown 5 min at 250°C. [b]Difference in -ΔG°'s for chalcogenide formation estimated from Table 1. [c]From peak widths using Scherrer equation. [d]Observed (apparent) band gap = $1240/\lambda_{1S}$.

XRD shows $CdS_{1-x}Se_x$ nanodots have cubic, zinc blende structures (Figure 5a). d-Spacings extracted from XRD correlate well with chalcogenide (S:Se) composition obtained from EDS and chemical elemental analysis (%S, Figure 5b). DPPE, TBPE and TOPE (E = S, Se) are reliable and useful chalcogen sources with varying reactivities. However, phosphines at the ends of the series in Figure 1, TPPE and HPTE are too reactive and unreactive, respectively. TPPSe reacts with $Cd(oleate)_2$ too fast and forms aggregates rather than dots, whereas HPTS does not react at all. The P=Se bond in HPTSe is also very strong: According to XRD and EDX, DPPS-HPTSe mixtures reacted with $Cd(oleate)_2$ to produce $CdS_{1-x}Se_x$ and Cd_3P_2 (Figure 5a).[28]

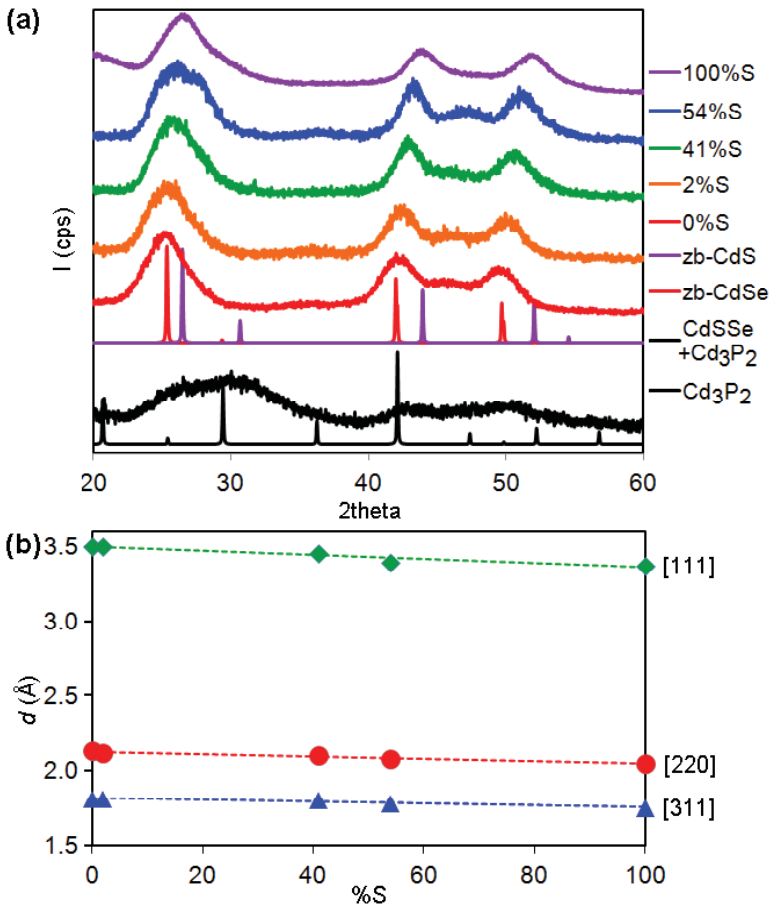

Figure 5. XRD patterns (a) and Vegard's plot (b) for $CdS_{1-x}Se_x$ dots obtained from different R_3PS–R_3PSe mixtures. In (a), reacting DPPS-HPTSe with $Cd(oleate)_2$ resulted in a mixture of CdSSe and Cd_3P_2.

Observed nanodot band gaps appear erratic at first glance (Figure 6a, b), however this is in great part due to different nanodot sizes across batches: Single crystalline domain sizes (diameters) obtained from XRD peak widths are all smaller than Bohr radii for CdS (<3.0 nm) and CdSe (<5.6 nm) and are thus confined (quantized) [55] (Table 3). When corrected for size, [56] $CdS_{1-x}Se_x$ nanodot band gaps progressively widen (blue-shift) with increasing sulfur content (Figure 6c). Critically, the band gap of nanocrystals made from sulfide and selenide precursors that are closer in reactivity, such as TOPSe–DPPS ($\Delta\Delta G°_{P=E}$ = 4.81 kcal/mol), lie on or very near a straight line between the size-corrected band gaps of pure CdS and CdSe

dots (Figure 6c). When two precursors have similar reactivity, they nucleate concomitantly at similar rates, forming true $CdS_{1-x}Se_x$ solid solutions. Solid solution band gaps are determined by the content-weighed band gap average between CdS and CdSe (Figure 6c). In contrast, the band gap of nanocrystals made from sulfide and selenide precursors with highly disparate reactivity, such as TOPSe–TOPS ($\Delta\Delta G°_{P=E}$ = 12.5 kcal/mol), lie far from the straight line between the size-corrected band gaps for pure CdS and pure CdSe, a phenomenon known as "bowing" (Figure 6c).3 When two precursors have very different reactivity, they nucleate separately at different rates (and times), forming CdSe/CdS core/shells. Core/shell band gaps are determined by CdSe core and degree of electron and hole delocalization into CdS shell.[57-59] In other words, purposely matching or mismatching molecular precursor reactivity can control degree of radial alloying and overall architecture of nanodots.

As reflected by XRD d-spacings and size-corrected band gaps, nanodot elemental composition (EDS and elemental analysis) correlates well with relative phosphine-chalcogenide reactivity. Plotting (%S)/ (%Se) content vs. relative P=S and P=Se bond energies (estimated as the difference in $-\Delta G°$ values from Table 1) shows %S increases and %Se decreases as P=S bond becomes weaker and P=Se bond becomes stronger (Figure 6c). We have used these data to develop an empirical expression that describes relative chalcogen content (S/Se) in $CdS_{1-x}Se_x$ nanodots as a function of theoretical and experimental parameters: The amount of each chalcogen incorporated should be (1) directly proportional to its precursor concentration (the more precursor molecules available, the more likely they will react with Cd), and (2) inversely proportional to its P=E bond energy (the stronger the bond, the more difficult it is to release chalcogen). Mathematically:

$$S/Se \approx k \times ([R_3PS]/ [R_3PSe]) \times [(-\Delta G°_{P=Se})/ (-\Delta G°_{P=Se})]$$

where k is an empirically fitted dimensionless constant (Figure 6d).

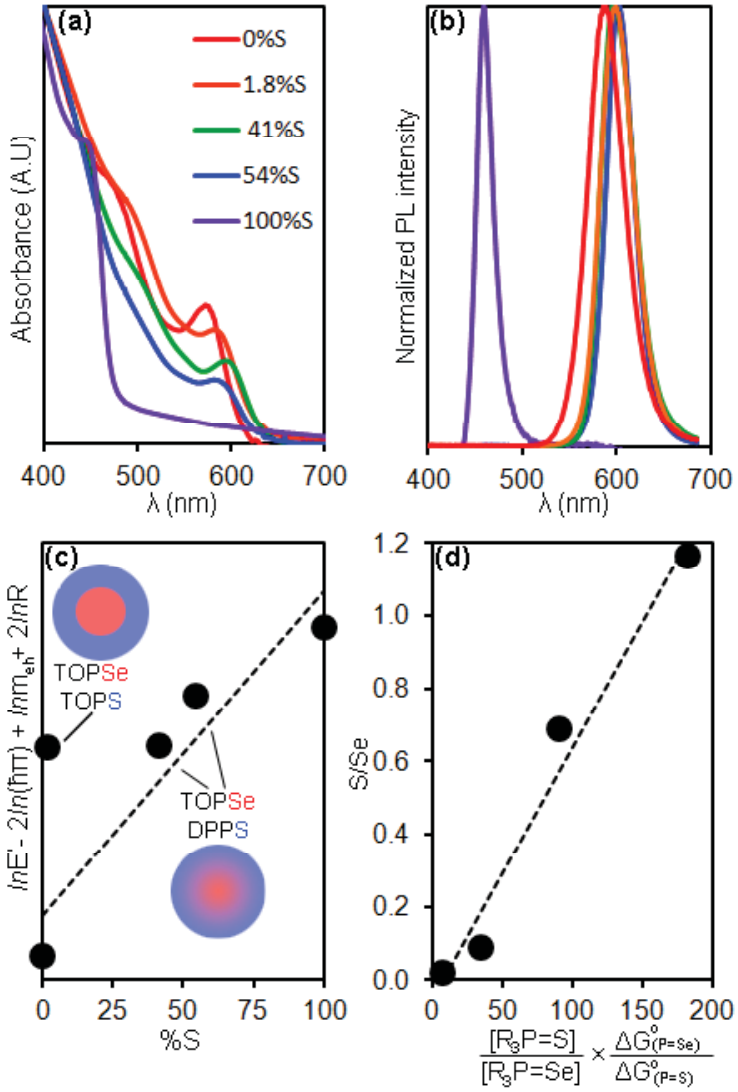

Figure 6. (a) UV-Vis, (b) PL, and (c) size-corrected band gaps of $CdS_{1-x}Se_x$ dots obtained from different R_3PS–R_3PSe mixtures. In (c), faster CdSe compared to CdS nucleation with TOPSe–TOPS leads to CdSe/CdS core/shells, whereas concomitant CdSe and CdS nucleation with TOPSe–DPPS leads to $CdS_{1-x}Se_x$ alloys. (d) Sulfur to selenium ratio (S/Se) in $CdS_{1-x}Se_x$ dots as a function of relative precursor concentration and reactivity: $\{([R_3PS]/[R_3PSe]) \times[(-\Delta G°P{=}Se)/(-\Delta G°P{=}S)]\}$. In (d), k = 0.00688.

Controlling CdE nanorod aspect ratio (E = S or Se). We then moved our attention to the effect of phosphine-chalcogenide precursor reactivity on length-to-diameter "aspect ratio" of

hexagonal (wurtzite) CdS and CdSe nanorods.[35] To probe this effect, we separately synthesized CdS and CdSe nanorods by single injection of one R_3PS or R_3PSe precursor, respectively, into a solution of $Cd(ODPA)_2$ at 320°C for CdS or 250°C for CdSe, and continued growth for 85 min. Lower reaction temperature was necessary for CdSe because phosphine-selenides are less stable (more reactive) precursors compared to phosphine-sulfides.[23] Figure 7 shows representative TEM images of CdS (a,b,c) and CdSe (e,f,g) nanorods obtained in this way. For both CdS and CdSe, nanorod length and aspect ratio consistently decrease as the phosphorous-chalcogen (P=E) bond energy decreases (Figure 7d,h and Table 4). In other words, nanorod length and aspect ratio decrease with increasing precursor reactivity.

Table 4. Controlling CdE nanorod aspect ratio (E = S or Se).

#	R_3PE	P=E energy[a] (kcal/mol)	length /nm	diameter /nm	Aspect ratio (l/d)
CdS nanorods[b]					
1	TOPS	71.60	267.0±38.7	3.2±0.6	83
2	TBPS	68.38	127.1±2.5	2.5±0.6	51
3	DPPS	63.91	64.4±4.6	4.4±1.1	15
CdSe nanorods[c]					
4	TOPSe	59.10	34.3±8.9	5.9±1.1	6
5	TBPSe	56.23	13.2±1.9	3.2±1.9	2
6	DPPSe	52.10	5.9±1.6	4.4±1.4	1

[a]Estimated as ΔG° from Table 1. [b]Synthesized at 320°C. [c]Synthesized at 250°C.

We note the biggest contribution to observed changes in aspect ratio are nanorod lengths: CdS nanorod length changes from 267.0nm±38.7nm, to 127.1nm±2.5nm, and 64.4nm±4.6nm

when TOPS, TBPS, and DPPS are used as sulfur precursors, respectively (Table 4, en-tries 1-3). CdSe nanorod length changes from 34.3nm±8.9nm, to 13.2nm±1.9nm, and 5.9nm±1.6nm when TOPSe, TBPSe, and DPPSe are used as selenium precursors, respectively (Table 4, entries 4-6). In contrast, changes in nanorod diameter are too small to be statistically significant: CdS nanorod diameters are 3.2nm±0.6nm, 2.5nm±0.6nm, and 4.4nm±1.1nm when TOPS, TBPS, and DPPS are used as sulfur precursors, respectively (Table 4, entries 1-3). CdSe nanorod diameters are 5.9nm±1.1nm, 3.2nm±1.9nm, and 4.4nm±1.4nm when TOPSe, TBPSe, and DPPSe are used as selenium precursors, respectively (Table 4, entries 4-6).

We rationalize these observations as follows: A decrease in phosphorous-chalcogen (P=E, E = S or Se) bond strength, i.e. lower P=E bond energy, increases phosphine-chalcogenide precursor reactivity. More reactive R_3PE precursors react faster and more un-controllably with $Cd(ODPA)_2$, leading to lower selectivity for anisotropic (unidirectional) 1D growth along wurtzite's z-axis and resulting in smaller nanorod aspect ratios. At the molecular level, we believe this is a nucleation-dominated effect: Each nanorod arises from a single initial nucleus or "seed" (small CdE cluster). Be-cause nanorod diameters stay the same –within experimental error– for different precursors, we assume they all grew from seeds formed at a similar, very early stage, i.e. nucleation. Upon injection, more reactive precursors such as DPPS or DPPSe form many more nuclei compared to less reactive precursors such as TOPS or TOPSe. After this fast nucleation event, there is less of the more reactive pre-cursor left in the reaction medium than of the less reactive precursor. This leads to more and shorter, lower aspect ratio nanorods for more reactive precursors than for less reactive (more stable) precursors.

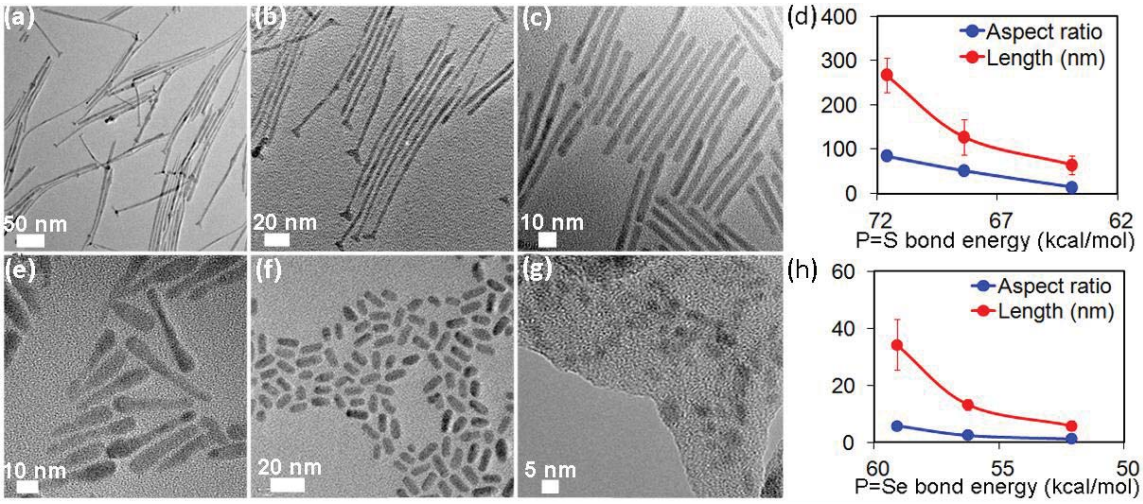

Figure 7. Change in nanorod aspect ratio as a function of precursor reactivity: CdS nanorods made with trioctyl-phosphine-sulfide, TOPS (a), tributyl-phosphine-sulfide, DPPS (b), and diphenylpropyl-phosphine-sulfide, DPPS (c). Plot of CdS nanorod length (nm) and aspect ratio as a function of calculated P=S bond strength (energy in kcal/mol) (d). CdSe nanorods made with trioctyl-phosphine-selenide, TOPSe (e), tributyl-phosphine-selenide, TBPSe (f), and diphenylpropyl-phosphine-selenide, DPPSe (g). Plot of CdSe nanorod length (nm) and aspect ratio as a function of calculated P=Se bond strength (energy in kcal/mol) (d). XRD shows all nanorods have mainly hexagonal (wurtzite) crystal structures.

The rate of chalcogen release from different molecular precursors during growth may also play a role in controlling nanorod aspect ratio. High precursor concentrations are known to favor unidirectional (1D) growth of wurtzite nanocrystals along the z-axis. A decrease in phosphorous-chalcogen bond strength accelerates the rate of chalcogen release to the reaction medium. More reactive precursors such as DPPS and DPPSe have weaker P=E bonds and cannot maintain high precursor concentrations for as long as less reactive precursors such as TOPS or TOPSe. Because high precursor concentrations are required for nanorod growth, more reactive precursors lead to shorter nanorods compared to less reactive (more stable) precursors.

The afore-mentioned trends also hold for analogous precursors across chalcogens (Table 4, entries 1-3 vs. 4-6). Phosphine-selenide precursors (R_3P=Se) have weaker phosphine-

chalcogen bonds and are much more reactive than phosphine-sulfide precursors ($R_3P=S$). As a result, CdSe nanorods form at lower temperatures (250°C) compared to CdS nanorods (320°C). Aspect ratio greatly decreases with increasing injection temperature: Only CdSe dots (l/d = 1) were formed at 320°C.

Table 5. Controlling axial anisotropy and composition gradients along $CdS_{1-x}Se_x$ nanorods.[a]

Precursor mix. (ratio)[a]	$(-\Delta G°_{P=S})$-$(-\Delta G°_{P=Se})$[b]	Length /nm[c]	Head diameter/nm[c]	Tail diameter/nm[c]	Aspect ratio[d]
TOPS–TOPSe(9:1)	12.5[a]	59.3±8.0	17.8±2.4	5.6±0.8	3 to 11[e]
TBPS–TBPSe(9:1)	12.1[a]	13.2±0.8	6.9±0.8	6.9±0.8	1.9

[a]Phosphines premixed at R.T. before injection to $Cd(ODPA)_2$ at 320°C; rods grown 85 min. [b]Difference in -ΔG°'s for chalcogenide formation estimated from Table 1. [c]From TEM. [d]Length/diameter. [e]Min.-max.

Controlling $CdS_{1-x}Se_x$ nanorod axial anisotropy and composition gradient. As mentioned above, we previously observed spontaneous formation of axially anisotropic $CdS_{0.42}Se_{0.58}$ nanorods by reacting a 9:1 TOPS–TOPSe mixture with $Cd(ODPA)_2$ at 320°C for 85 min (Scheme 1); these graded nanorods have a length of 17.8nm±2.4nm and diameters of 17.8nm±2.4nm (CdSe "head") and 5.6nm±0.8nm (CdS "tail") (Table 5 and Figure 8a).[35] We explained the formation mechanism of these nanorods by considering relative TOPS and TOPSe reactivities. Our calculations show P=E bond in TOPS is 12.5 kcal stronger (less reactive) than in TOPSe. Because of this large energy difference, fast (<20 min) CdSe homogeneous nucleation, followed by slow (~85 min) CdS- heterogeneous nucleation (epitaxial growth) along the nanorods z-axis leads to axially anisotropic rods (Figure 8a, c, e).

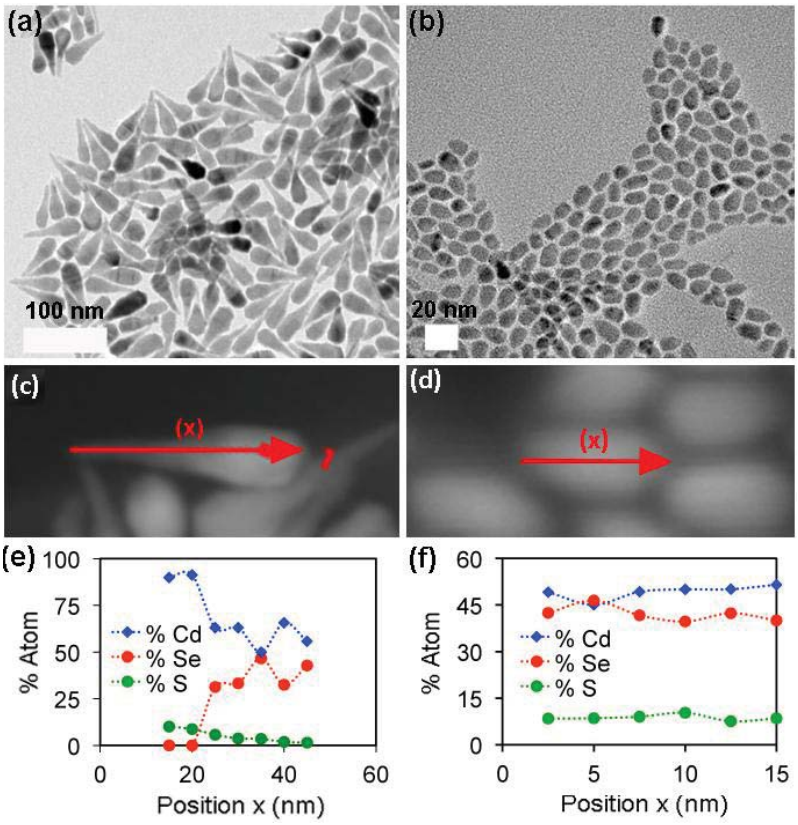

Figure 8. TEM images (a,b) and EDS line scans (c,d,e,f) of axially anisotropic $CdS_{0.42}Se_{0.58}$ nanorods made with a 9:1 TOPS–TOPSe precursor mixture (a,c,e), and regular $CdS_{0.34}Se_{0.66}$ nano-rods made with a 9:1 TBPS–TBPSe precursor mixture (b,d,f). Arrows represent 50 nm in (c) and 17.5 nm in (d). Other conditions: $Cd(ODPA)_2$, 320°C, 85 min. XRD shows all nanorods have mainly hexagonal (wurtzite) crystal structures.

In contrast, we have observed formation of more regularly shaped $CdS_{0.34}Se_{0.66}$ nanorods by reacting a 9:1 TBPS–TBPSe mixture with $Cd(ODPA)_2$ at 320°C for 85 min; these nanorods have a length of 13.2nm±0.8nm and a consistent diameter of 6.9nm±0.8 nm (Table 5 and Figure 8b). The overall aspect ratio (1.9) is smaller compared to the aspect ratio of the axially anisotropic nano-rods (3 to 7) (Table 5). Critically, EDS line scans show no composition gradient along the nanorods' length. We explain this uniform composition and consistent diameter (lack of axial anisotropy) based on relative TBPS and TBPSe reactivities. Our calculations show P=E bond in TBPS is somewhat closer in energy compared to (12.1

kcal stronger less reactive than) TOPSe. Because of this smaller energy difference, nanorods form by concomitant nucleation and growth of CdS1-xSex along the nanorods z-axis. As shown above for pure CdS and CdSe binary nanorods, overall aspect ratio is determined by relative precursor bond energies (and reactivities) in each case. The weighed averaged P=E bond energy ($-\Delta G_{ave}°$) for a 9:1 TOPS–TOPSe mix is 70.4 kcal/mol, whereas that for a 9:1 TBPS–TBPSe mix is 67.2 kcal/mol. As a result, axially anisotropic CdS0.42Se0.58 nanorods obtained with TOPS–TOPSe have a significantly higher aspect ratio (l/d up to 11) compared to regular $CdS_{0.34}Se_{0.66}$ nanorods obtained with TBPS–TBPSe (l/d = 1.9).

Conclusions

In summary, we have demonstrated predictable, "bottom-up" control of nanoscale composition, architecture, and morphology (aspect ratio) in CdS-CdSe nanocrystal quantum dots and rods by purposely altering and modulating the chemical reactivity of molecular phosphine-chalcogenide precursors, R_3PE (E = S, Se). Computational (DFT), NMR (^{31}P and ^{77}Se), and high temperature crossover studies unambiguously confirmed a chemical bonding interaction between phosphorous and chalcogen atoms in all R3PE precursors. These studies showed phosphine-chalcogenide reactivity decreases in the order: TPPE > DPPE > TBPE > TOPE > HPTE (E = Se > S). Structural (XRD, TEM, EDS) and optical (UV-Vis, PL) characterization of $CdS_{1-x}Se_x$ nanodots, synthesized by a single high-temperature injection of a R_3PS–R_3PSe mixture to cadmium-oleate, reveal their elemental composition and degree of radial alloying depends on relative R_3PS and R_3PSe reactivity. Similarly, structural (XRD, TEM, EDS) characterization of CdS, CdSe, and $CdS_{1-x}Se_x$ nanorods, synthesized by high temperature injection of individual R_3PE (E = S or Se) or R_3PS–R_3PSe precursor mixtures to cadmium-phosphonate, reveal their length-to-diameter (aspect) ratio and degree of axial

alloying (composition gradient) depends on R_3PE precursor reactivity. We expect these observations will contribute to the development of more predictable, "bottom-up" synthetic routes to fabricate well-defined hetero-structures with highly specific properties. We are currently exploring this idea in the fabrication of nanomaterials for catalytic and thermoelectric applications.

Experimental Section

Materials. Cadmium oxide (99.998%), sulfur (99.999%), oleic acid (tech., 90%), and diphenylpropyl phosphine (DPP) (97%) were purchased from AlfaAesar; octadecylphosphonic acid (ODPA) from PCI synthesis; selenium (99.999%), trioctylphosphine oxide (TOPO) (99%), anhydrous toluene, hexaethylphosphorous-triamide (HPT) (97%), and dioctylamine (98%) from Sigma-Aldrich; triphenylphosphite (TPP) (97%), tributylphosphine (TBP) (99%), and trioctylphosphine (TOP) (97%) from Strem. Materials were used as received unless specified otherwise. NMR data were collected on either a Varian 400-MR or Varian VXR-400 spectrometer. ^{31}P NMR spectra were referenced to 85% phosphoric acid, H_3PO_4 (δ 0 ppm). ^{77}Se NMR spectra were referenced to $PPh_3Se/CDCl_3$ (δ -266.20 ppm vs. Me_2Se δ 0 ppm).[60, 61] Standards were sealed within capillaries in NMR tubes. Chemical elemental analyses were performed by Galbraith Labs., Inc. (Knoxville, TN).

Synthesis. *$CdS_{1-x}Se_x$ nanodots*. R_3PS and R_3PSe stock solutions were made by dissolving 12.5 mmol of chalcogen (0.40 g S or 0.98 g Se) in 25 mmol phosphine (7.7 g TPP, 5.7 g DPP, 5.1 g TBP, 9.3 g TOP, or 6.2 g HPT) in a dry-N_2 filled glove box. Synthesis. CdO (24 mg, 0.18 mmol), OA (0.24 g, 0.85 mmol) and dioctylamine (8 g, 0.937 mmol) were heated to 100°C, evacuated under dynamic vacuum for 15 min, refilled with argon and heated to

300°C to form a completely colorless solution. Solution was allowed to cool to 120°C, evacuated under dynamic vacuum for 15 min, refilled with argon and heated back to 250°C. At 250°C, a premixed R_3PS–R_3PSe (1 mL total volume, 1.14 mmol total chalcogens) was swiftly injected, causing a rapid color change. Mixture was stirred for 0.5 or 5 min at 250°C, allowed to cool to R.T. and diluted with toluene (5 mL). Nanocrystals were isolated by addition of methanol (24 mL), followed by centrifugation (5,000 rpm for 10 min). *Chalcogen crossover control experiments.* TOPS (1.14 M, 0.3 mL) and DPPSe (1.14 M, 0.3 mL) were added to an NMR tube inside a dry-N_2 filled glove box. The tube was sealed and ^{31}P NMR was recorded R.T. as well as after heating to 100°C, 200°C and 300°C.

CdS nanorods. CdS nanorods were made by a modified literature procedure.[35,62] R_3PS stock solutions were made by dissolving S (0.40 g, 12.5 mmol) in 12.5 mmol phosphine (2.9 g DPP, 2.5 g TBP, or 4.6 g TOP) in a dry-N_2 filled glove box. *Synthesis.* CdO (105 mg, 0.81 mmol), TOPO (1.3 g, 3.6 mmol) and ODPA (530 mg, 0.94 mmol) were heated to 100 °C, evacuated under dynamic vacuum for 15 min, refilled with argon, and heated to 320 °C to form a completely colorless solution. Solution was cooled to 120 °C, evacuated under dynamic vacuum for 15 min, refilled with argon, and heated back to 320 °C. When temperature reached 300°C, phosphine (1.20 mL of DPP, TBP, or TOP) was injected into the flask. When temperature reached 320°C, R_3PS stock solution (1 mL, 2.25 mmol DPPS, TBPS, or TOPS) was swiftly injected, causing a gradual color change. Temperature was equilibrated at 315°C and stirring con-tinued for 85 min. Final mixture was al-lowed to cool to R.T. and diluted with toluene (5 mL). Nanocrystals were isolated by addition of 1:1 v/v 2-propanol/nonanoic acid mixture (24 mL), followed by centrifugation (5,000 rpm for 10 min). *CdSe nanorods.* R_3PSe stock solutions were made by dissolving Se (0.98 g, 12.5 mmol) in

12.5 mmol phosphine (2.9 g DPP, 2.5 g TBP, or 4.6 g TOP) in a dry-N2 filled glove box. *Synthesis.* CdSe nanorods were made by a similar procedure as reported above for CdS nanorods, except that injection and growth were performed at 250°C.

$CdS_{1-x}Se_x$ nanorods. R_3PS and R_3PSe stock solutions were made as reported above for CdS and CdSe nanorods. Axially anisotropic $CdS_{0.42}Se_{0.58}$ nanorods with a 'drumstick'-like morphology were synthesized by a literature procedure.[35] Regular (axially isotropic) CdS0.34Se0.66 nanorods were made as follows: CdO (105 mg, 0.81 mmol), TOPO (1.38 g, 3.6 mmol) and ODPA (540 mg, 0.94 mmol) were heated to 100°C, evacuated under dynamic vacuum for 15 min, refilled with argon and heated to 320°C to form a completely colorless solution. Solution was cooled to 120°C, evacuated under dynamic vacuum for 15 min, refilled with argon and heated back to 320°C. When temperature reached 300°C, TBP (1.20 ml) was injected into the flask. When temperature reached 320°C, a premixed, 9:1 TBPS–TBPSe solution (1 mL total volume, 2.25 mmol total chalcogens) was swiftly injected, causing a gradual color change. Temperature was equilibrated at 315°C and stirring continued for 85 min. Final mixture was allowed to cool to R.T. and diluted with toluene (5 mL). Nanocrystals were isolated by addition of 1:1 v/v 2-propanol/nonanoic acid mixture (24 mL), followed by centrifugation (5,000 rpm for 10 min).

Structural characterization. X-Ray Diffraction. Powder X-ray diffraction (XRD) data were measured using Cu-Kα radiation on a Scintag XDS-2000 diffractometer equipped with a theta-theta goniometer, a sealed-tube solid-state generator, and an air-cooled Kevex Psi Peltier silicon detector. Transmission Electron Microscopy. Transmission electron microscopy (TEM) was conducted on carbon-coated copper grids using a FEI Technai G2 F20 Field Emission scanning transmission electron microscope (STEM) at 200 kV (point-to-

point resolution <0.25 nm, line-to-line resolution <0.10 nm). Nanorods' elemental axial composition was characterized by energy dispersive spectroscopy (EDS) line scans in STEM mode, and by energy-filtered (EF) imaging spectroscopy (EF-TEM). Particle analysis. Dimensions were measured manually and/or by using ImageJ. Size measurements and particle statistics were obtained for at least >100 $CdS_{1-x}Se_x$, CdS and CdSe particles. Average sizes are reported along ±standard deviations.

Optical characterization. Absorption spectra were measured with a photodiode-array Agilent 8453 UV-Vis spectrophotometer. Solvent absorption was subtracted from all spectra. Steady state photoluminescence (PL) spectra were measured with a Horiba-Jobin Yvon Nanolog scanning spectrofluorometer equipped with a photomultiplier detector. Photoluminescence (PL) quantum yields (QYs) were measured following literature procedures.63 Absorption and PL emission spectra were measured ≥twice and average QYs recorded.

Computational details. Calculations were carried out using the Gaussian 03 package64 running on CenterOS based Linux cluster at the Prairie View A&M University. Tao-Perdew-Staroverov-Scuseria (TPSS) method, [65] a new generation of density functional implemented in Gaussian 03, was used for geometry optimization, solvation modeling and frequency calculations. TPSS matches or exceeds in accuracy prior functionals, including the popular B3LYP with hybrid exchange functional.[66] TPSS recognizes relatively weak in-teractions such as agostic interactions, while B3LYP significantly underestimates them. Because hydrogen atoms in the mod-eled system do not play significant roles, a 6-311G* basis set[67, 68] was used for all elements in our system. Not ap-plying polarization functions on H's far away from P does not significantly de-grade computational precision and accuracy and can

considerably accelerate calculations.[69] All structures were fully optimized and frequency analyses were performed until minima were achieved, with zero imaginary vibrational frequencies derived from vibrational frequency analysis. Thermodynamic functions including enthalpies, entropies and free energies were calculated at 298.15 K and 1 atm. To examine basis set effects, a Dunning/Huzinaga full double zeta[70] with Stuttgart/Dresden effective core poten-tial basis set (SDD) and a triple-zeta Dunning's correlation consistent basis set (cc-pVTZ)71 were used for all atoms with TPSS functionals to perform a sin-gle point energy (SPE) calculation.

Acknowledgment

This work is partially supported (1D semiconductor- based photocatalysts) by U.S. Department of Energy (DOE), Office of Basic Energy Sciences, Division of Chemical Sciences, Geosciences, and Biosciences through the Ames Laboratory. Ames Laboratory is operated for U.S. DOE by Iowa State University (ISU) under Contract No. DE-AC02-07CH11358. The document number assigned to this thesis/dissertation is IS-T 3100.We thank ISU, Ames Lab Royalty Account, and Institute for Physical Research and Technology (IPRT) for startup funds (J.V.); Office of Science, U.S. DOE Visiting Faculty Program (VFP), and Faculty and Student Teams (FaST) for summer internships (B.C., B.W., J.C., and H.-J.F.); ISU Chemistry for a Hach Undergraduate Scholarship (H.R.A.); and Sarah Cady for ^{77}Se NMR assistance.

References

[1] Swafford, L. A.; Weigand, L. A.; Bowers, M. J., II; McBride, J. R.; Rapaport, J. L.; Watt, T. L.; Dixit, S. K.; Feldman, L. C.; Rosenthal, S. J. *J. Am. Chem. Soc.* **2006**, *128*, 12299–12306.

[2] Ouyang, J.; Vincent, M.; Kingston, D.; Descours, P.; Boivineau, T.; Zaman, M. B.; Wu, X.; Yu, K. *J. Phys. Chem. C* **2009**, *113*, 5193–5200.

[3] Bailey, R. E.; Nie, S. M. *J. Am. Chem. Soc.* **2003**, *125*, 7100–7106.
[4] Regulacio, M. D.; Han, M.-Y. *Acc. Chem. Res.* **2010**, *43*, 621–630.

[5] Gurusinghe, N. P.; Hewa-Kasakarage, N. N.; Zamkov, M. *J. Phys. Chem. C* **2008**, *112*, 12795–12800.

[6] Wang, R.; Calvignanello, O.; Ratcliffe, C. I.; Wu, X.; Leek, D. M.; Zaman, M. B.; Kingston, D.; Ripmeester, J. A.; Yu, K. *J. Phys.Chem. C* **2009**, *113*, 3402–3408.

[7] Smith, D. K.; Luther, J. M.; Semonin, O. E.; Nozik, A. J.; Beard, M. C. *ACS Nano* **2011**, *5*, 183–190.

[8] Jang, E.; Jun, S.; Pu, L. *Chem. Commun*. **2003**, 2964–2965.

[9] Smith, A. M.; Nie, S. *J. Am. Chem. Soc.* **2011**, *133*, 24–26.

[10] Peng, X. *Adv. Mater.* **2003**, *15*, 459–463.

[11] Manna, L.; Wang, L. W.; Cingolani, R.; Alivisatos, A. P. *J. Phys. Chem. B* **2005**, *109*, 6183–6192.

[12] Peng, X. A.; Peng, X. *J. Am. Chem. Soc.* **2001**, *123*, 1389–1395.

[13] Talapin, D. V.; Shevchenko, E. V.; Murray, C. B.; Kornowski, A.; Förster, S.; Weller, H. *J. Am. Chem. Soc.* **2004**, *126*, 12984–12988.

[14] Li, L.-S.; Alivisatos, A. P. *Phys. Rev. Lett.* **2003**, *90*, 097402-1–097402-4.

[15] Saunders, A. E.; Ghezelbash, A.; Sood, P.; Korgel, B. A. *Langmuir* **2008**, *24*, 9043–9049.

[16] Cozzoli, P. D.; Manna, L.; Curri, M. L.; Kudera, S.; Gianninni, C.; Striccoli, M.; Agostiano, A. *Chem. Mater*. **2005**, *17*, 1296–1306.

[17] Peng, Z. A.; Peng, X. *J. Am. Chem. Soc.* **2001**, *123*, 183–184.

[18] Wang, W.; Banerjee, S.; Jia, S.; Steigerwald, M. L.; Herman, I. P. *Chem. Mater*. **2007**, *19*, 2573–2580.

[19] Peng, X.; Manna, L.; Yang, W.; Wickham, J.; Scher, E.; Kadavanich, A.; Alivisatos, P. *Nature* **2000**, *404*, 59–61.

[20] Peng, Z. A.; Peng, X. *J. Am. Chem. Soc.* **2002**, *124*, 3343–3353.

[21] Panda, A. B.; Acharya, S.; Efrima, S.; Golan, Y. *Langmuir* **2007**, *23*, 765–770.

[22] Li, Y.; Zhong, H.; Li, R.; Zhou, Y.; Yang, Z.; Li, Y. *Adv. Funct. Mater.* **2006**, *16*, 1705–1716.

[23] Zhang, J.; Jin, S.; Fry, H. C.; Peng, S.; Shevchenko, E.; Wiederrecht, G. P.; Rajh, T. *J. Am. Chem. Soc.* **2011**, *133*, 15324–15327.

[24] Bullen, C. R.; Mulvaney, P. *Nano Lett.* **2004**, *4*, 2303–2307.

[25] Yang, P.; Tretiak, S.; Ivanov, S. *J. Clust. Sci.* **2011**, *22*, 405–431.

[26] Steckel, J. S.; Yen, B. K. H.; Oertal, D. C.; Bawendi, M. G. *J. Am. Chem. Soc.* **2006**, *128*, 13032–13033.

[27] Rempel, J. Y.; Bawendi, M. G.; Jensen, K. F. *J. Am. Chem. Soc.* **2009**, *131*, 4479–4489.

[28] Koh, W.-K.; Yoon, Y.; Murray, C. B. *Chem. Mater.* **2011**, *23*, 1825–1829.

[29] Liu, H.; Owen, J. S.; Alivisatos, A. P. *J. Am. Chem. Soc.* **2007**, *129*, 305–312.

[30] Owen, J. S.; Chan, E. M.; Liu, H.; Alivisatos, A. P. *J. Am. Chem. Soc.* **2010**, *132*, 18206–18213.

[31] García-Rodríguez, R.; Liu, H. *J. Am. Chem. Soc.* **2012**, *134*, 1400–1403.

[32] Cossairt, B. M.; Owen, J. S. *Chem. Mater.* **2011**, *23*, 3114–3119.

[33] Jiang, Z.-J.; Kelley, D. F. *ACS Nano* **2010**, *4*, 1561–1572.

[34] Evans, C. M.; Evans, M. E. Krauss, T. D. *J. Am. Chem. Soc.* **2010**, *132*, 10973–10975.

[35] Ruberu, T. P. A.; Vela, J. *ACS Nano* **2011**, *5*, 5775–5784.

[36] Alemseghed, M. G.; Ruberu, T. P. A.; Vela, J. *Chem. Mater.* **2011**, *23*, 3571–3579.

[37] Xu, F.; Rock, P. A.; Ma, X.; Kauzlarich, S. M.; Navrotsky, A. *J. Mater. Res.* **2009**, *24*, 1368–1374.

[38] Hammond, G. S. *J. Am. Chem. Soc.* **1955**, *77*, 334–338.

[39] Bryan, J. D.; Gamelin, D. R. *Prog. Inorg. Chem.* **2005**, *54*, 47–126.

[40] Chin, M.; Durst, G. L.; Head, S. R.; Bock, P. L.; Mosbo, J. A. *J. Organomet. Chem.* **1994**, *470*, 73–85.

[41] Min, W. J.; Jung, S.; Lim, S. J.; Kim, Y.; Shin, S. K. *J. Phys. Chem. A* **2009**, *113*, 9588–9594.

[42] White, D.; Coville, N. J. *Adv. Organomet. Chem.* **1994**, *36*, 95–158.

[43] Brown, T. L.; Lee, K. J. *Coord. Chem. Rev.* **1993**, *128*, 89-116.

[44] McDonough, J. E.; Mendiratta, A.; Curley, J. J.; Fortman, G. C.; Fantasia, S.; Cummins, C. C.; Rybak-Akimova, E. V.; Nolan, S. P.; Hoff, C. D. *Inorg. Chem.* **2008**, *47*, 2133–2141.

[45] Bachrach, S. M. In *Reviews in Computational Chemistry*, Vol. V; Lipkowitz, K. B., Boyd, D. B., Eds.; VCH: New York, **1995.**

[46] Mulliken, R. S. *Phys. Rev.* **1932**, *41*, 49–71.
[47] Mulliken, R. S. *J. Chem. Phys.* **1955**, *23*, 1833–1840–2346.

[48] Cioslowski, J. *J. Am. Chem. Soc.* **1989**, *111*, 8333–8336.

[49] Amarasekara, A. S.; Lewis, D.; Nayani, S. L.; Timofeeva, T. V.; Fan, H.-J. *J. Molec. Struc.* **2010**, *977*, 175–179.

[50] Breneman, C. M.; Wiberg, K. B. *J. Comput. Chem.* **1990**, *11*, 361–73.

[51] Bush, R. C.; Angelici, R. J. *Inorg. Chem.* **1988**, *27*, 681–686.

[52] Henderson, W. A.; Streuli, C. A. *Anal. Chem.* **1960**, *32*, 985–987.

[53] Denton, A. R.; Ashcroft, N. W. *Phys. Rev. A* **1991**, *43*, 3161–3164.

[54] Shannon, R. D. *Acta Cryst. A* **1976**, *32*, 751–767.

[55] Zhong, X.; Feng, Y.; Knoll, W.; Han, M. *J. Am. Chem. Soc.* **2003**, *125*, 13559–13563.

[56] Hollingsworth, J. A.; Klimov, V. I. Soft Chemical Synthesis and Manipulation of Semiconductor Nanocrystals. In *Nanocrystal Quantum Dots*, 2nd Ed.; Klimov, V. I., Ed.; CRC Press: Boca Raton, FL, **2010**, 1–61.

[57] Guo, Y.; Marchuk, K.; Sampat, S.; Abraham, R.; Fang, N.; Malko, A. V.; Vela, J. *J. Phys. Chem. C* **2012**, *116*, 2791–2800.

[58] García-Santamaría, F.; Chen, Y. F.; Vela, J.; Schaller, R. D.; Hollingsworth, J. A.; Klimov, V. I. *Nano Lett.* **2009**, *9*, 3482–3488.

[59] Van Embden, J.; Jasieniak, J.; Mulvaney, P. *J. Am. Chem. Soc.* **2009**, *131*, 14299–14309.

[60] Cullen, E. R.; Guziec, F. S.; Murphy, C. J.; Wong, T. C.; Andersen, K. K. *J. Am. Chem. Soc.* **1981**, *103*, 7055–7057.

[61] Bullen, C.; van Embden, J.; Jasieniak, J.; Cosgriff, J. E.; Mulder, R. J.; Rizzardo, E.; Gu, M.; Raston, C. L. *Chem. Mater.* **2010**, *22*, 4135–4143.

[62] Robinson, R. D.; Sadtler, B.; Demchenko, D. O.; Erdonmez, C. K. Wang, L.-W.; Alivisatos, A. P. *Science* **2007**, *317*, 355–358.

[63] Grabolle, M.; Spieles, M.; Lesnyak, V.; Gaponik, N.; Eychmüller, A.; Resch-Genger, U. *Anal. Chem.* **2009**, *81*, 6285–6294.

[64] Frisch, M. J.; Trucks, G. W.; Schlegel, H. B.; Scuseria, G. E.; Robb, M. A.; Cheeseman, J. R.; Montgomery, J. A.; Vreven, T.; Kudin, K. N.; Burant, J. C. *et al*. Gaussian 03, Revision D.01. Gaussian, Inc.; Wallingford CT, **2004**.

[65] Tao, J. M.; Perdew, J. P.; Staroverov, V. N.; Scuseria, G. E. *Phys. Rev. Lett.* **2003**, *91*, 12129–12137.

[66] Staroverov, V. N.; Scuseria, G. E.; Tao, J. M.; Perdew, J. P. *J. Chem. Phys.* **2003**, *119*, 12129–12137.

[67] Hehre, W. J.; Ditchfie, R; Pople, J. A. *J. Chem. Phys.* **1972**, *56*, 2257–2261.

[68] Krishnan, R.; Binkley, J. S.; Seeger, R.; Pople, J. A. *J. Chem. Phys.* **1980**, *72*, 650–654.

[69] Fan, Y. B.; Hall, M. B. *Organometallics* **2005**, *24*, 3827–3835.

[70] Dunning, T. H.; Hay, P. J. In *Modern Theoretical Chemistry*, Vol. 3; Schaefer, H. F., Ed. Plenum: New York, **1976**, 1–28.

[71] Kendall, R. A.; Dunning, T. H.; Harrison, R. J. *J. Chem. Phys.* **1992**, *96*, 6796–806.

CHAPTER 4

CONTROLLED FABRICATION OF COLLOIDAL SEMICONDUCTOR-METAL HYBRID HETEROSTRUCTURES: SITE SELECTIVE METAL PHOTO DEPOSITION

Reprinted with permission from *Chem. Mater.* **2011**, *23*, 3571.

Mussie G. Alemseghed, T. Purnima A. Ruberu, Javier Vela

Abstract

Reliable synthesis of semiconductor-metal heterostructures would increase their availability for fundamental studies and applications in catalytic, magnetic, and opto-electronic devices. Here we demonstrate there are three main pathways for the formation of Pt and Pd nanoparticles on CdS and $CdS_{0.4}Se_{0.6}$ nanorods. A thermal pathway and a photochemical pathway occur when the metal precursor is heated or irradiated directly in the presence of an electron donor, leading to homogeneous nucleation and formation of freestanding metal nanoparticles. A separate photochemical pathway occurs in the presence of semiconductor nanorods, leading to exciton formation and quenching by electron trapping at surface defect sites. The localized electrons act as seeding points, leading to heterogeneous nucleation and formation of surface-bound metal nanoparticles. Careful selection of synthetic conditions allows deposition of Pt and Pd particles on CdS and $CdS_{0.4}Se_{0.6}$ nanorods with a high degree of selectivity (90-95% surface-bound obtained photochemically) over the formation of freestanding metal particles (70-94% unattached under thermal conditions). In addition, metal photo deposition occurs on specific segments of $CdS_{0.4}Se_{0.6}$ nanorods with

compositional anisotropy by taking advantage of the band gap differential between different nano-domains. Irradiation at short wavelengths favors formation of Pd nanoparticles on the large band-gap CdS-rich region of the nanorods (57% and 55% at 350 nm and 420 nm, respectively), while irradiation at longer wavelengths favors the formation of Pd nanoparticles on the small band gap CdSe-rich region of the nanorods (83% at 575 nm). The ability of tuning the spatial composition of these and similar heterostructures will impact the ability to engineer and direct energy flows at the nanoscale.

Introduction

Semiconductor-metal hybrid heterostructures are promising building blocks for applications in catalytic, magnetic, and optoelectronic devices.[1-7] The semiconductor's tunable band gap (300-4000 nm 4.1-0.3 eV),[8,9] broad and intense absorption ($\varepsilon \approx 10^5$-10^6 $L \cdot mol^{-1} \cdot cm^{-1}$),[10] and long-lived exciton (up to 40 ns for CdSe, 1.8 μs for PbS)[11,12] provide unmatched light absorption and emission capabilities. Large aspect ratio semiconductors such as nanorods are of particular interest due to their ability to generate multiple excitons.[13,14] The metal can serve as an additional chromophore, a fluorescence enhancer, a paramagnet, or a charge collecting material where carriers localize after exciton quenching. For example, semiconductor-metal hybrid heterostructures have been shown to convert solar energy into potential and chemical energy. They become redox-active upon illumination and remain redox-active after being stored in the dark for several hours.[15] In addition, semiconductor and metal nanocrystals display a high degree of chemical-, photo-, and colloidal-stability (solubility) unmatched by other materials such as organic polymers and transition metal complexes. The ability to selectively build semiconductor-metal

heterostructures with several morphologies and spatial relationships between their individual components could be used to engineer and direct energy flows at the nanoscale.[4]

Interest in the synthesis of colloidal semiconductor-metal hybrid nanostructures has grown exponentially in recent years.[1,2] Different research groups have used thermal and photochemical methods to synthesize CdS, CdSe, and core/shell CdSe/CdS nanorods tipped with Au,[16-20] Ag_2S,[19] Co,[21,22] Pt, PtM (M = Co, Ni),[23] PdO and Pd_4S[24] nanoparticles, ZnO nanorods-tipped with Ag nanoparticles,[25] a-TiO_2 nanorods tipped with Co nanoparticles,[26] and CdSe tetrapods tipped with Au nanoparticles.[18] Similarly, metal nanoparticle deposition along the whole length of semiconductor nanorods has been demonstrated for CdS-Au,[16,27] CdSe/CdS-Au,[19] CdSe-Pt,[28] CdS-PdO and CdS-Pd_4S,[24] CdS-Pt,[29] CdSe/CdS-Pt,[29] CdS-FePt,[30] and a-TiO_2-Co.[26] Other reports include CdSe nanowires decorated with Au, Pt, PtCo, and PtNi nanoparticles,[31] PbS nanocubes coated with Au nanoparticles,[32] and nanoporous CdS loaded with Pt nanoparticles.[33] Some of these reports build upon earlier work on the surface modification of microcrystalline semiconductors using platinum group metals as a way to generate hydrogen evolving photocatalysts, for example CdS-Pt doped wth Zn and Ag sulfides,[34,35] and powders made of MS/CdS/M (M = Pt, Ir),[36] CdS_xSe_{1-x}-Pt,[37] CdS/Pt/Na_2S,[38] CdS-Pt and TiO_2-Pt,[39] and CdS/TiO_2.[40]

Perhaps the most important aspect from a synthetic perspective is to prepare semiconductor-metal and other semiconductor-based hybrid heterostructures with ‘open’ (non-core/shell) [41,42] configurations in a controlled and selective fashion. Reliable synthetic routes would increase the availability of these materials for fundamental study and systematic testing, allowing the establishment of structure-activity relationships and facilitating their eventual application. It is valuable to investigate selective syntheses of colloidal

semiconductor-metal heterostructures that are highly reproducible and amenable to scale-up. In the case of CdS-Au heterostructures, photochemical deposition leads to growth of Au particles at the tips of CdS nanorods, whereas thermal deposition (in the dark) leads to growth of Au particles along the whole length of CdS nanorods.[1, 43] Deposition throughout the semiconductor surface is more desirable for solar energy harvesting because it could lead to more efficient multiple exciton quenching *via* charge separation. The opposite trend is observed in CdS-Pt heterostructures where photochemical deposition leads to growth of Pt particles along the whole length of CdS nanorods[29] and thermal deposition at high-temperature (200 °C) leads to growth of Pt particles at the CdS nanorod tips.[23] The exact deposition behavior varies depending on the particular metal and semiconductor surface under study. For CdS-PtM (M = Ni, Co), thermal deposition at low precursor concentrations results in PtM particles at the CdS nanorod tips (particularly for PtCo), whereas thermal deposition at high concentrations results in PtM particles along the whole length of the CdS nanorods.[23] For CdSe/CdS-Au and CdSe/CdS-Pt heterostructures, the position of the Au and Pt particles correlates with the position of CdSe core or 'seed'.[16,29] For CdSe/CdS-AuPd and CdSe/CdS-$AuFe_xO_y$ heterostructures, ultraviolet irradiation results in particles at the CdSe/CdS nanorod tips.[44] A majority of the documented photochemical deposition methods on nanostructures employ laser irradiation[16,17,19,25] which invariably occurs over small sample areas or 'spots' leading to low material yields and thus limiting its synthetic utility. Few researchers and virtually no synthetic chemists have direct and reliable access to expensive lasers.

In this paper we use thermal and large throughput lamp photochemical methods to address the controllable and site selective deposition of metal nanoparticles on single-phase

and heterostructured semiconductor nanorods. We use Pt and Pd deposition on regular CdS nanorods in addition to axially anisotropic $CdS_{1-x}Se_x$ nanorods as model systems. Based on the results of several deposition experiments under different temperature and illumination conditions, the formation of metal particles proceeds by at least three fundamental pathways. Two of these pathways, one thermal and one photochemical, are independent of the semiconductor surface and lead to the formation of freestanding metal particles. A third photochemical pathway is mediated by the semiconductor and leads to formation of surface-bound metal particles which are preferred because many semiconductor-metal interactions such as charge- and energy-transfer are strongly distance dependent. Selection of experimental conditions allows synthesis of surface-bound particles with a high degree of selectivity over formation of freestanding (unattached) metal particles. We also demonstrate photo deposition of metal particles can be controllably directed toward specific segments or regions of a heterostructured semiconductor with compositional anisotropy by taking advantage of the inherent band gap and optical properties of its different segments or 'nano-domains'.

Results and Discussion

To date, most colloidal semiconductor-metal heterostructures have been fabricated by decomposing soluble organometallic precursors or salts in the presence of semiconductor nanorods. This is accomplished by simple heating in some cases, such as deposition of Au particles along the length of CdS nanorods.[1,16] Better control over metal deposition, particularly Pt, has been reported using laser spot irradiation leading to growth of Pt particles along the length of CdS nanorods.[23,29] Exploring the feasibility of synthesizing hybrid heterostructures without use of lasers, we observed deposition of Pt and Pd on colloidal CdS

and $CdS_{1-x}Se_x$ nanorods could be easily carried out with an inexpensive set of lamps. Lamps illuminate much larger areas at a time compared to lasers (whole samples in this study as well as other recent studies);[17,25,44,47] their use could lead to a larger synthetic throughput and wider general availability of semiconductor-metal hybrid heterostructures for fundamental studies and application. While metal deposition should be possible with any lamp whose energy sat below the band gap of the semiconductor (*i.e.*, <520 nm or >2.4 eV for CdS nanorods); we find the precise mechanism and locale of metal deposition varies greatly depending on the specific irradiance profile of the lamp used.

Table 1. Metal deposition on colloidal semiconductor nanorods.[1]

No.	Nanorods	M	Precursor	Conds.[1]	T / °C	rxn. time / h	Np. diameter/nm	% Bound	% Free	np. / rod
1	CdS	Pt	$CODPtMe_2$	dark	80	3	1.9±0.6	30	70	1.1±0.9
2	CdS	Pt	$CODPtMe_2$	350nm	24	3	2.6±0.8	80	20	1.6±1.3
3	CdS	Pt	$CODPtMe_2$	420nm	24	3	3.1±1.4	95	5	1.4±0.9
4	None	Pt	$CODPtMe_2$	420nm	24	3	2.9±1.2	-	-	-
5	CdS	Pd	TMEDA-$PdMe_2$	420nm	24	3	7.2±1.7	90	10	5.6±2.2
6	CdS	Pd	TMEDA-$PdMe_2$	dark	24	3	4.1±0.7	6	94	2.1±0.7
7	$CdS_{0.4}Se_{0.6}$	Pd	TMEDA-$PdMe_2$	350nm	24	1	2.6±0.8	37	63	1.5±1.1
8	$CdS_{0.4}Se_{0.6}$	Pd	TMEDA-$PdMe_2$	420nm	24	1	4.9±2.2	48	52	2.1±1.5
9	$CdS_{0.4}Se_{0.6}$	Pd	TMEDA-$PdMe_2$	575nm	24	1	5.0±1.5	90	10	1.3±0.8
10	$CdS_{0.4}Se_{0.6}$	Pd	TMEDA-$PdMe_2$	575nm	24	3	5.1±1.4	92	8	8.0±2.0

[1]All reactions were carried out using a 2 mL nanorod solution in toluene of OD_{470nm} = 1.2 (CdS) or OD_{630nm} = 1.3 ($CdS_{0.4}Se_{0.6}$), 28-30 mg metal precursor, 0.5 mL NEt_3 as electron donor, and 1 mL

toluene. See Experimental.

Platinum deposition on CdS nanorods. We first attempted to deposit Pt on CdS nanorods thermally at 80 °C in the complete absence of light. Thermal deposition in the dark results in the formation of small Pt particles with a diameter of 1.9 ± 0.6 nm as observed by transmission electron microscopy (TEM) (Figure 1). However, the great majority of the thermally deposited Pt particles (70%) are freestanding, unattached to CdS nanorods. Only a small fraction of Pt particles (30%) are bound to the surface of CdS nanorods (Table 1, entry 1) (Figure 1d). Among surface-bound particles, there is an average of 1.1 ± 0.9 Pt particles per CdS nanorod, with a maximum of 3 Pt particles per CdS nanorod (Figure 1e). The fact that freestanding Pt particles form thermally from the direct reaction between $CODPtMe_2$ and triethylamine indicates that Pt particles can form independently from CdS and that preformed Pt particles do not tend to associate with CdS nanorods after they have already formed.

We then carried out metal deposition experiments under photochemical conditions, and observed different results depending on the specific lamp wavelength used. Photo deposition of Pt on CdS nanorods under illumination with a 350 nm lamp (35 nm fwhm) at room temperature (R.T.) results in the formation of Pt particles with a diameter of 2.6 ± 0.8 nm. A significant fraction of Pt particles (20%) formed under 350 nm illumination are still freestanding (remain unassociated with the CdS nanorods) (Table 1, entry 2). However, a larger fraction of Pt particles (80%) are bound to the surface of CdS nanorods (Figure 1d).

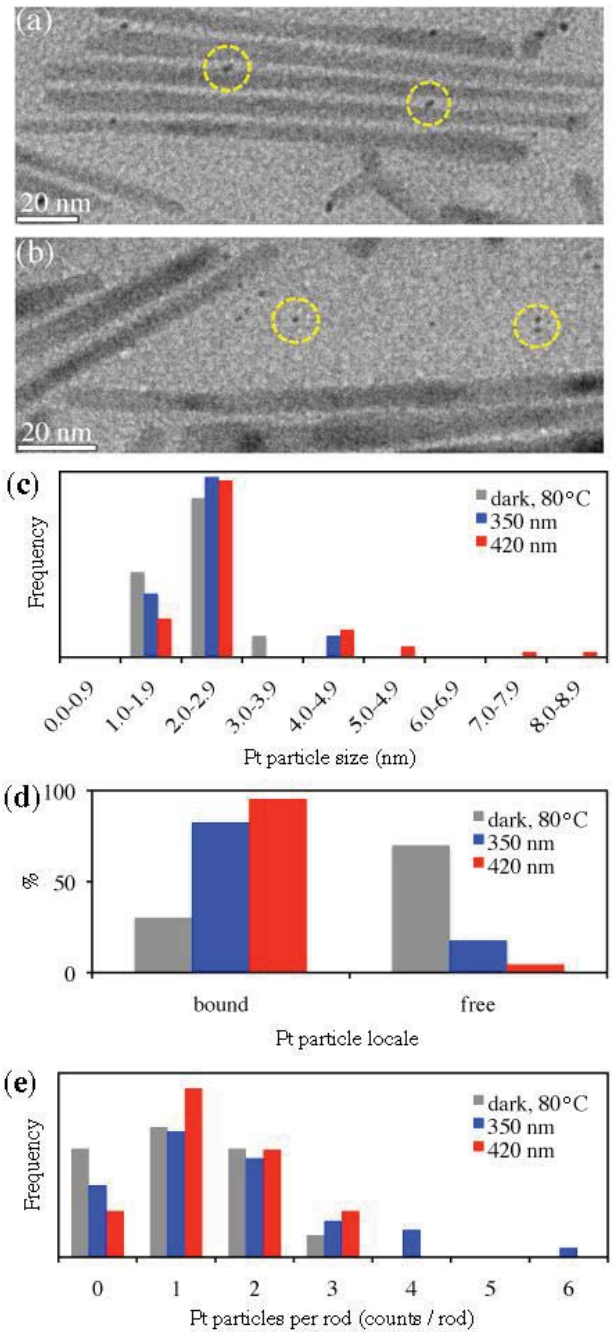

Figure 1. Sample TEM micrographs of CdS-Pt heterostructures prepared (a) photochemically (420 nm, R.T.), and (b) thermally (in the dark, 80 °C) (a few surface-bound and freestanding Pt particles are circled for comparison). Pt particle size (c), locale (d), and loading per rod (e) histograms for CdS-Pt heterostructures prepared thermally (80 °C in the dark, gray) and photochemically (350 nm, blue; 420 nm, red) (>50-100 CdS rods and >50-300 Pt particles measured in each case).

Among surface-bound particles, there is an average of 1.6 ± 1.3 Pt particles per CdS nanorod, although we observed a few cases with as many as 3, 4, and 6 Pt particles per CdS nanorod

(Figure 1e). Similarly, photo deposition of Pt on CdS nanorods under illumination with a 420 nm lamp (30 nm fwhm) at room temperature results in the formation of Pt particles with a diameter of 3.1 ± 1.4 nm (Figures 1 and 2). In this case, only a marginal number of Pt particles (5%)[48] are freestanding (Table 1, entry 3). The greater majority of Pt particles (95%) formed under 420 nm illumination are bound to the surface of CdS nanorods (Figures 1d and 2). Among surface-bound particles, there is an average of 1.4 ± 0.9 Pt particles per CdS nanorod, with a maximum of 3 Pt particles per CdS nanorod (Figure 1e). In the absence of the CdS nanorods, the reaction between $CODPtMe_2$ and triethylamine under 350 nm illumination at room temperature results in the formation of Pt particles with a diameter of 2.9 ± 1.2 (Table 1, entry 4). The fact that Pt particles form by direct reaction between $CODPtMe_2$ and triethylamine under 350 nm illumination confirms that photochemical formation of freestanding Pt particles can occur independently from the CdS nanorods. CdS nanorods need not act as 'sensitizers' for the decomposition of the organometallic precursor. Similar photochemical reactions have been reported for other metal particles and precursors.[49]

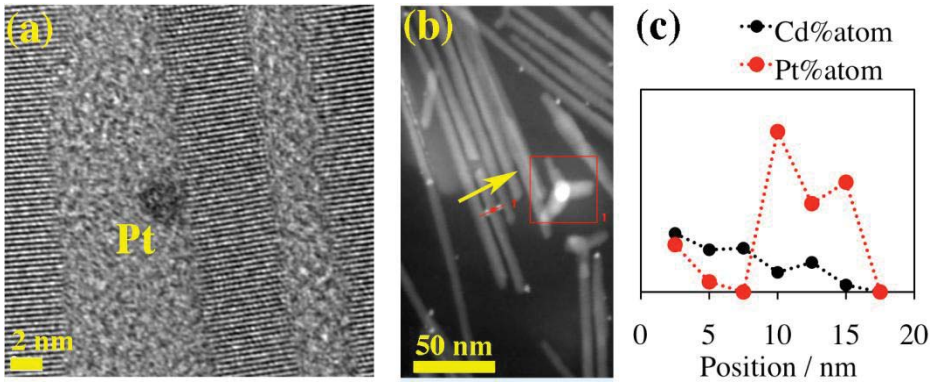

Figure 2. (a) High-resolution (HR) TEM micrograph of a surface-bound Pt particle produced via photo-chemical deposition on CdS nanorods (420 nm, 3 h). (b) EDX-Line scan and (c) corresponding composition profile of two Pt nanoparticles attached to opposing sides of a CdS nanorod. The yellow arrow indicates scan direction (squared area was used for drift correction).

Site selective metal photo deposition: Free- vs. surface-bound metal particles. The observations above are independent of the post-synthesis handling of samples, all of which were consistently worked up in the same way (see Experimental). Size selection was not performed. Instead, these observations suggest the existence of multiple parallel pathways for the formation of Pt nanoparticles. In order to better understand this, we recorded the absorption spectra of CdS nanorods and the molecular Pt precursor, $CODPtMe_2$, in toluene solution (Figure 3a). CdS nanorods have an absorption band-edge at 500 nm and continue to absorb more strongly at shorter wavelengths. The $CODPtMe_2$ precursor is colorless and does not absorb in the visible region but has three distinct bands in the ultraviolet region: 285 nm, 320 nm, and 360 nm. Comparing these spectral features to the irradiance profiles of the two lamps used (Figure 3b), both CdS nanorods and $CODPtMe_2$ can absorb light emitted by the 350 nm lamp. In contrast, only CdS nanorods, not $CODPtMe_2$, can absorb light emitted by the 420 nm lamp.

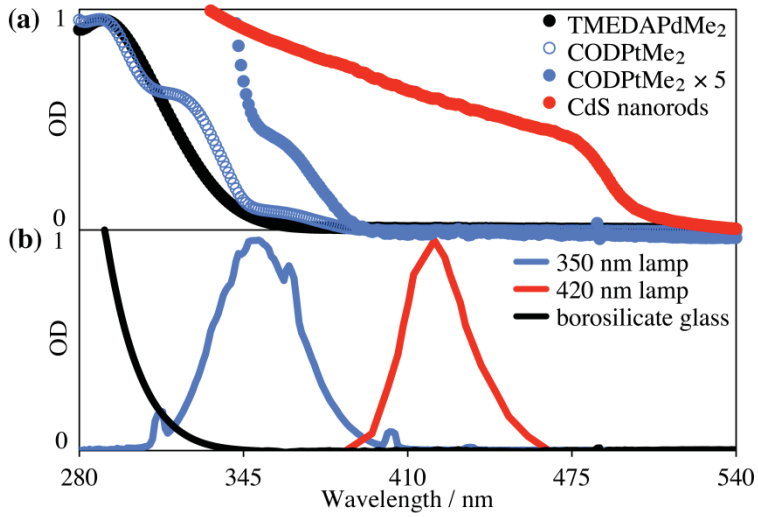

Figure 3. (a) Absorption spectra of $TMEDAPdMe_2$ (black), $CODPtMe_2$ (blue) and colloidal CdS rods (red) (recorded in toluene with quartz cuvettes). (b) Irradiance spectra of 350 nm (blue) and 420 nm (red) lamps, and absorption spectrum of the borosilicate glass (black) used as reaction vessel (all spectra were arbitrarily normalized to a maximum optical density OD = 1).

Our experimental observations can be explained as follows: When the organometallic precursor $CODPtMe_2$ is heated in the dark, it decomposes thermally and nucleates into freestanding (unbound) Pt particles anywhere in solution (Scheme 1a). Under photochemical conditions, direct absorption by (and excitation of) the $CODPtMe_2$ in the presence of triethylamine results in photoinduced reduction and nucleation of freestanding (unbound) Pt particles anywhere in solution, as observed experimentally to some extent (15%)[48] with the 350 nm lamp (Scheme 1b).[48,50] Together, these thermal and photochemical homogeneous nucleation pathways are responsible for the formation of freestanding Pt nanoparticles independently of the semiconductor surface. Alternatively, under photochemical conditions, when absorption (and excitation) occurs through the CdS nanorods, a third pathway occurs where electron-hole pairs (excitons) are formed on the semiconductor followed by migration of electrons to surface trap states (dangling bonds)[8] on the semiconductor surface. Holes can be quenched by triethyl amine, sulfide ions, or other electron donor. The surface localized electrons can act as seeding points for the binding and reduction of $CODPtMe_2$ into Pt nuclei. This heterogeneous nucleation mechanism is responsible for the formation of bound Pt nanoparticles on the surface of CdS nanorods, as observed experimentally with both 350 nm and 420 nm lamps (Scheme 1c).

Scheme 1. Metal deposition pathways

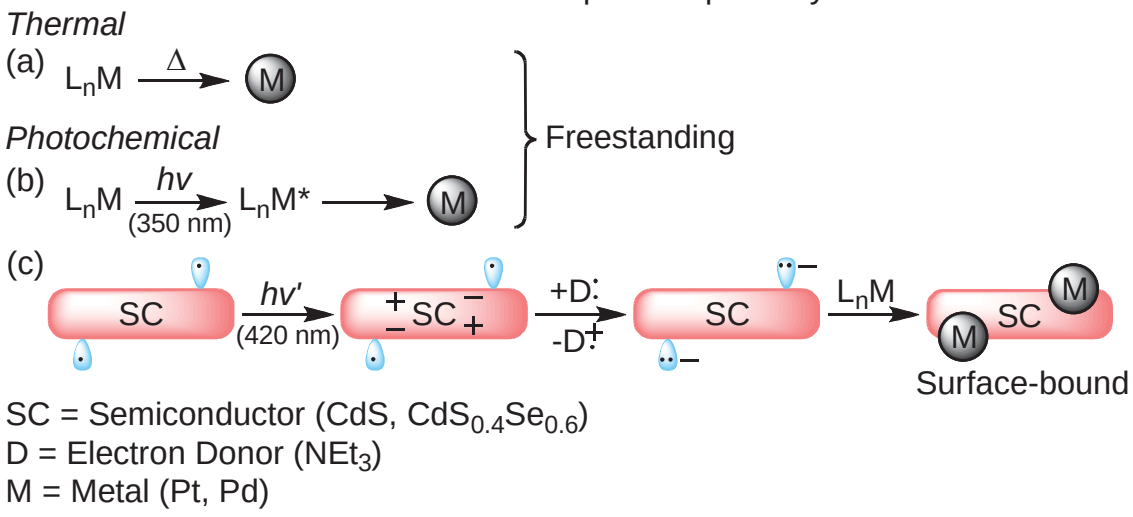

SC = Semiconductor (CdS, $CdS_{0.4}Se_{0.6}$)
D = Electron Donor (NEt_3)
M = Metal (Pt, Pd)

The observed site-selectivities (Table 1, entries 1-3) can be used to gather additional information about the metal photo deposition process. At 350 nm, the absorption coefficient of colloidal CdS nanoparticles is known to be of the order of $\varepsilon_{350nm} \approx 1.5 \pm 5 \times 10^6$ $L \cdot mol^{-1} \cdot cm^{-1}$, [10] whereas we measured the absorption coefficient of $CODPtMe_2$ to be only $\varepsilon_{350nm} = 260 \pm 30$ $L \cdot mol^{-1} \cdot cm^{-1}$. Using these values to normalize the respective relative populations of surface-bound (80%) and freestanding (15%)[48] particles obtained photochemically with the 350 nm lamp, we calculate a 1000× (thousand-fold) *apparent preference* for photochemical Pt particle formation *via* homogeneous nucleation (in solution) over heterogeneous nucleation (on the CdS surface). This simple calculation assumes growth of Pt nanoparticles from Pt nuclei is fast and irreversible. It does not take into account energy barriers required for either homogeneous or heterogeneous nucleation. Also, it does not take into account the efficiency of charge collection by dangling bonds on the semiconductor surface (exciton quenching by trap states), or of platinum photoreduction by either mechanism (Scheme 1b or 1c). Additionally, this preference may vary depending on the chemical composition of the semiconductor surface (Cd- vs. S-rich, ligand type and surface coverage, etc.).[2,8,49] We emphasize the above preference is just an *apparent* and yet-to-be-completed account of the relative ease of solution formation vs. surface deposition of Pt particles under photochemical conditions.

Palladium deposition on CdS nanorods. Using the optimized experimental conditions described above for Pt (illumination with a 420 nm lamp for 3h at R.T.), we carried out the photo deposition of Pd on CdS nanorods using the molecular precursor cis-dimethyl(N, N, N', N'-tetramethylenediamine)-palladium(II), $TMEDAPdMe_2$. In this case, Pd particles form

with an average diameter of 7.2 ± 1.7 nm, the majority of which (90%) are bound to the CdS surface, and only a few (10%) are freestanding (Table 1, entry 5) (Figure 4a, c, d).

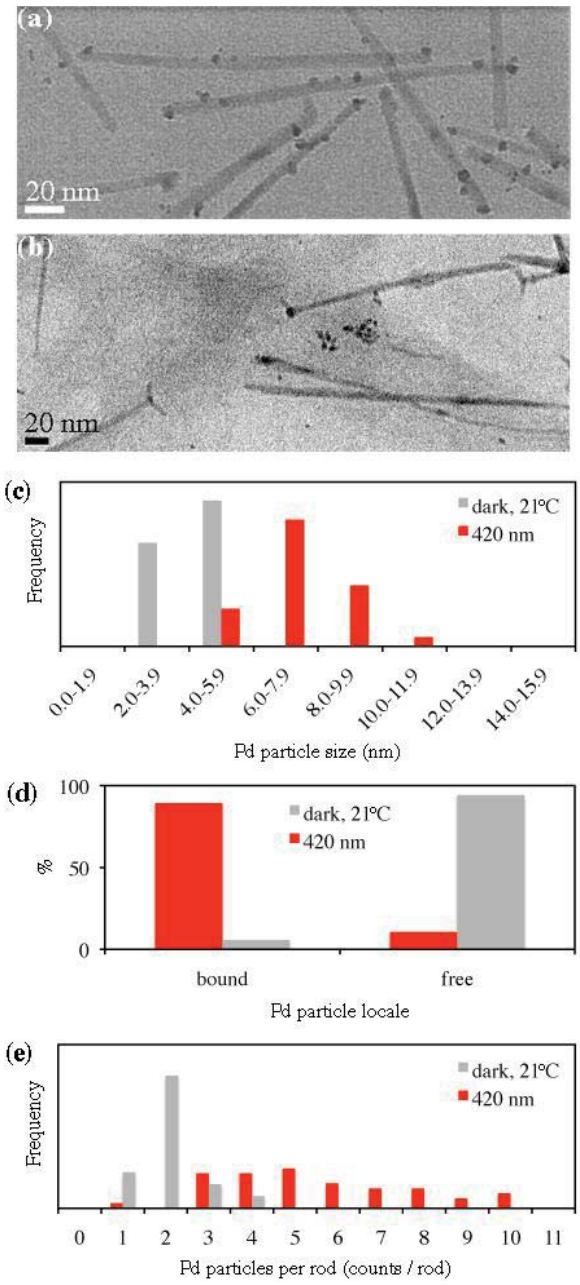

Figure 4. Sample TEM micrographs of CdS-Pd heterostructures prepared (a) photochemically (420 nm, 24 °C), and (b) thermally (in the dark, 24 °C). Pd particle size (c), locale (d), and loading per rod (e) histograms for CdS-Pd heterostructures prepared thermally (24 °C in the dark, gray) and photochemically (420 nm, red) (>50-100 CdS rods and >50-300 Pd particles measured in each case).

Among surface-bound particles, there is an average of 5.6 ± 2.2 Pd particles per CdS nanorod, and a maximum of 11 Pd particles per CdS nanorod (Figure 4e). Under these conditions, the Pd precursor appears to be more reactive and Pd deposition more facile, as judged by the larger Pd particle diameter and the higher number of Pd particles per rod compared to Pt. We attribute this difference to the inherent thermal and photochemical instability of $TMEDAPdMe_2$ compared to $CODPtMe_2$. Conversely, thermal deposition of Pd on CdS nanorods at room temperature in the complete absence of light results in the formation of Pd particles with a diameter of 4.1 ± 0.7 nm (Figure 4b, c). In agreement with our previous observations, the majority of the thermally deposited Pd particles (94%) are freestanding, and only a very few (6%) are bound to the surface of CdS nanorods (Table 1, entry 6) (Figure 4d). Among surface-bound particles, there is an average of 2.1 ± 0.7 Pd particles per CdS nanorod, with a maximum of 4 Pd particles per CdS nanorod (Figure 4e).

Palladium deposition on axially anisotropic CdSSe nanorods. We then attempted the photo deposition of Pd on axially anisotropic $CdS_{0.4}Se_{0.6}$ nanorods using $(TMEDA)PdMe_2$ as precursor. These $CdS_{0.4}Se_{0.6}$ nanorods have a graded-alloy composition between a thick CdSe-rich 'head' on one end and a thin CdS-rich 'tail' on the other end (Figures 5a and 6d).[46] Initial photo deposition experiments on these axially anisotropic nanostructures were directed at testing the degree of opto-electronic communication between small and large band gap segments; Pd particles can be deposited on both ends of the $CdS_{0.4}Se_{0.6}$ nanorods. However, we find illumination energy (lamp wavelength) and time both have a strong effect on the diameter, loading, and specific locale of the Pd particles obtained. Additionally, the distribution of Pd particles along the length of the axially anisotropic $CdS_{0.4}Se_{0.6}$ nanorods varies significantly depending on the specific lamp used.

Photo deposition of Pd on $CdS_{0.4}Se_{0.6}$ rods for 1 h at R.T. results in: 2.6 ± 0.8 nm diameter Pd particles with an average of 1.5 ± 1.1 (5 max.) Pd particles per rod when using a 350 nm lamp (35 nm fwhm); 4.9 ± 2.2 nm diameter Pd particles with an average of 2.1 ± 1.5 (6 max.) Pd particles per rod when using a 420 nm lamp (30 nm fwhm); 5.0 ± 1.5 nm diameter Pd particles with an average of 1.3 ± 0.8 (3 max.) Pd particles per rod when using a 575 nm lamp (~75 nm fwhm) (Table 1, entries 7-9) (Figure 5). Further, photo deposition for 3 h at R.T. results in 5.1 ± 1.4 nm diameter Pd particles with an average of 8.0 ± 2.0 (15 max) Pd particles per rod when using a 575 nm lamp (Table 1, entry 10) (Figure 5). These results highlight interesting trends in metal particle size, loading, and locale during the metal photo deposition process. First, it appears that the Pd particle diameter may increase with increasing lamp wavelength for a given photo deposition time, however the standard deviations are too large to make the differences in Pd particle diameter statistically significant: 2.6 ± 0.8 nm (350 nm for 1 h), 4.9 ± 2.2 nm (420 nm for 1h), and 5.0 ± 1.5 nm (575 nm for 1h) (Table 1, entries 7-9) (Figure 5d). In contrast, the Pd particle diameter remains constant for different photo deposition times while keeping the wavelength constant: 5.0 ± 1.5 nm (575 nm for 1 h) ~ 5.1 ± 1.4 nm (575 nm for 3 h) (Table 1, entries 9-10) (Figure 5d).

In agreement with our previous observations, the fraction of surface-bound Pd particles increases with increasing lamp wavelength: 350 nm for 1 h (37% surface-bound) < 420 nm for 1 h (48% surface-bound) < 575 nm for 1 h (80% surface-bound) (Table 1, entries 7-9) (Figure 5e). Similary, the fraction of surface-bound Pd particles remains mostly unchanged with increasing photo deposition time for a given wavelength: 575 nm for 1 h (90% surface-bound) ~ 575 nm for 3 h (92% surface-bound) (Table 1, entries 9-10) (Figure 5e). This is

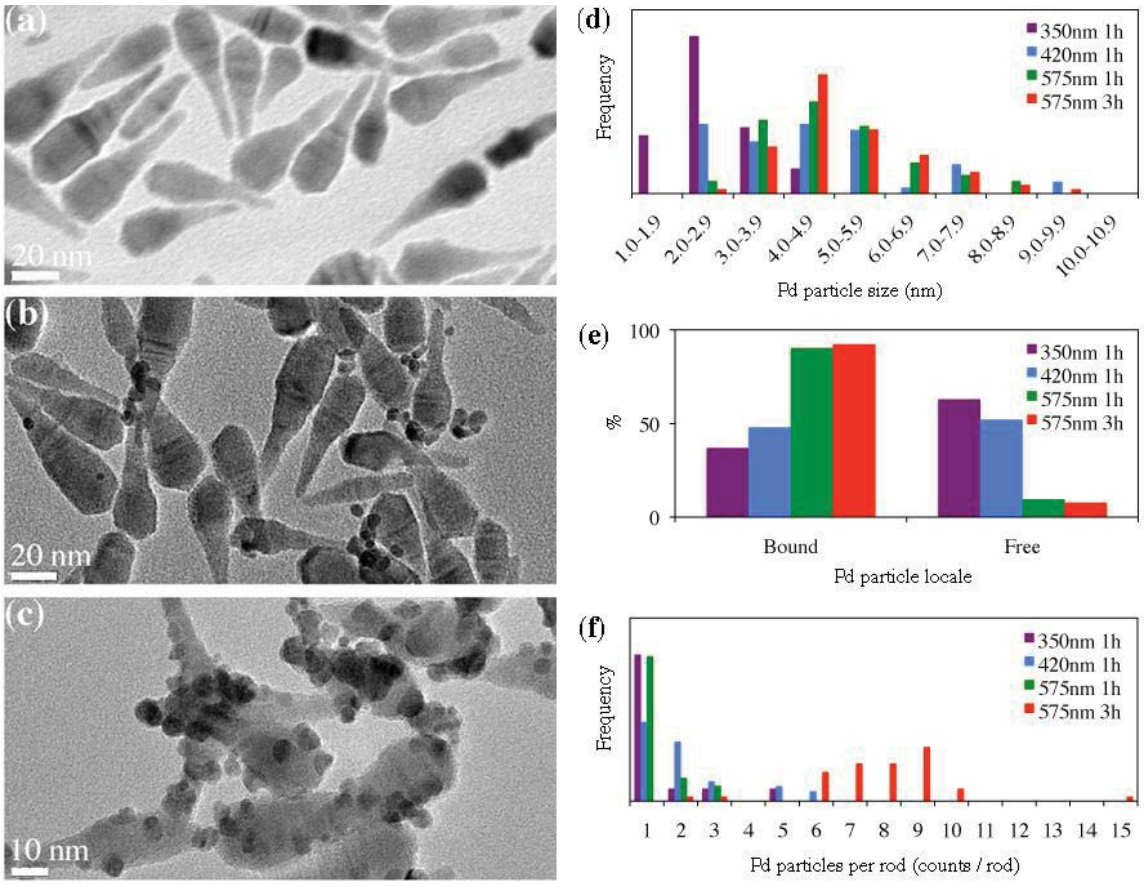

Figure 5. Sample TEM micrographs of $CdS_{0.4}Se_{0.6}$ nanorods (a), and $CdS_{0.4}Se_{0.6}$-Pd heterostructures prepared photochemically at 575 nm, 24 °C for 1h (b) and 3 h (c). Pd particle size (d), locale (e), and loading per rod (f) histograms for $CdS_{0.4}Se_{0.6}$-Pd heterostructures prepared photochemically at 350 nm for 1h (violet), 420 nm for 1h (blue), 575 nm for 1h (green), and 575 nm for 3h (red) (>50-100 $CdS_{0.4}Se_{0.6}$ nanorods and >50-300 Pd particles measured in each case).

consistent with our previous view that Pd and Pt particles form *via* semiconductor-mediated photochemical deposition and, unlike Au particles, freestanding Pd particles do not significantly stick to the surface of the $CdS_{0.4}Se_{0.6}$ nanorods after they formed. In turn, Pd loading (number of Pd particles per $CdS_{0.4}Se_{0.6}$ rod) remains approximately the same for different wavelengths while keeping the photo deposition time constant: 1.5 ± 1.1 Pd particles/rod (350 nm for 1 h) ~ 2.1 ± 1.5 Pd particles/rod (420 nm for 1 h) ~ 1.3 ± 0.8 Pd particles/rod (575 nm for 1 h) (Table 1, entries 7-9) (Figure 5f). Nonetheless, Pd loading

greatly increases with increasing photo deposition times while keeping the wavelength constant: 1.3 ± 0.8 Pd particles/rod (575 nm for 1 h) < 8.0 ± 2.0 Pd particles/rod (575 nm for 3 h) (Table 1, entries 9-10) (Figure 5f). This constitutes a six-fold increase in Pd loading with tripling of the photo deposition time.

Site selective metal photo deposition: Head- vs. tail-bound metal particles on axially anisotropic nanorods. To better understand the locale and distribution of Pd particles on the axially anisotropic $CdS_{0.4}Se_{0.6}$ nanorods, we measured the distance between the axial position of each surface-bound Pd particle and one of the nanorod tips (arbitrarily chosen as the 'head' tip), and then parameterized this distance by dividing it over the corresponding nanorod length (Figure 6a-d). In this way, the location of each surface-bound Pd particle is defined by a given 'length fraction' that has a value between 0 (head tip) and 1 (tail tip) (Figure 6d). The advantage of using length fractions rather than absolute position values minimizes inhomogeneities associated with the distribution in nanorod lengths (59.3 ± 8.0 nm).[46] This way, the locale or position of many Pd particles can be better compared among several nanorods and across different photo deposition experiments. Using length fraction measurements, we discerned that photo-deposited Pd particles preferentially accumulate toward one end or the other end of the axially anisotropic $CdS_{0.4}Se_{0.6}$ nanorods depending on the specific lamp wavelength used (Figure 6c). When we carry out the photo deposition using 350 nm and 420 nm lamps, a large fraction of the surface-bound Pd particles (≥ 50%) are located at, or very near, the tip of the thin CdS-rich tail of the $CdS_{0.4}Se_{0.6}$ nanorods with length fractions between 0.9-1 (Figure 6c). In contrast, when we carry out photo deposition with the 575 nm lamp, most of the surface-bound Pd particles (83%) are located on the thick CdSe-rich segment of the $CdS_{0.4}Se_{0.6}$ nanorods, with length fractions between 0-0.5 (Figure

6c). If, instead of using length fractions, we divide each nanorod longitudinally in two half segments (at ca. 30 nm half length), and measure the fraction of Pd particles located on the thicker half segment versus those located on the thinner half segment, we observe similar trends in particle distribution. When we carry out the photo deposition using 350 nm and 420 nm lamps, respectively 57% and 55% of the surface-bound Pd particles are located on the thinner CdS-rich segment (Figure 6e). In contrast, when we carry out the photo deposition with the 575 nm lamp, 83% of the surface-bound Pd particles are located on the thicker CdSe-rich segment (Figure 6e).

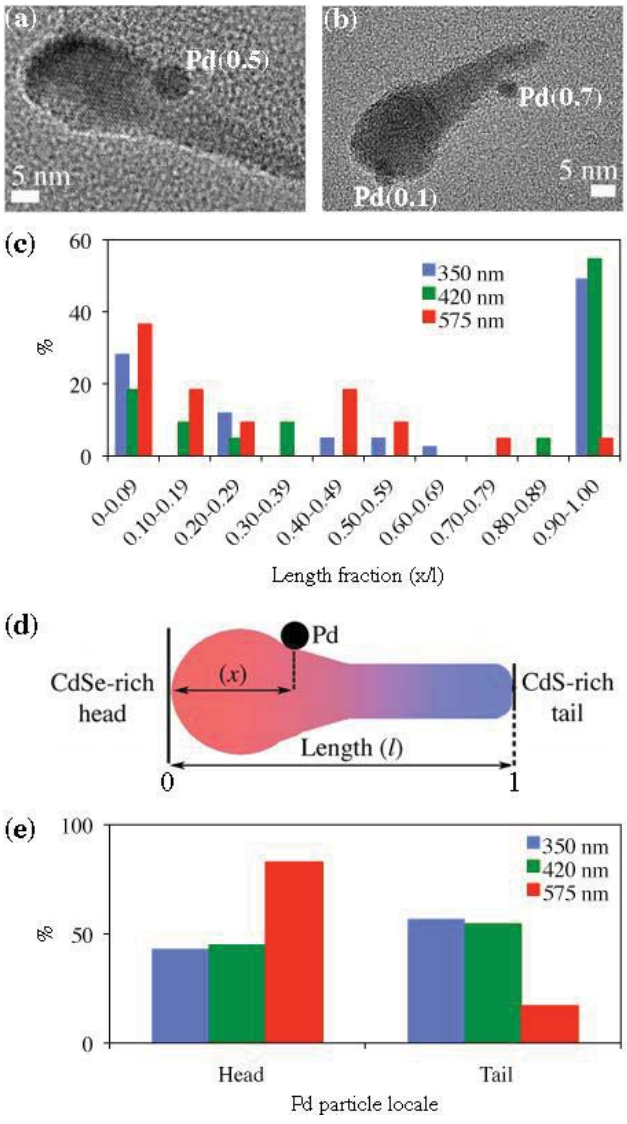

Figure 6. Photodeposition of Pd nanoparticles on axially anisotropic $CdS_{0.4}Se_{0.6}$ nanorods: (a) Sample TEM micrographs with Pd length fractions. (b) Location of Pd nanoparticles along the length of the $CdS_{0.4}Se_{0.6}$ nanorods, plotted as a fraction of the total length of the nanorods (length fraction). (c) Schematic of $CdS_{0.4}Se_{0.6}$-Pd heterostructures and length fraction measurements. (b) Head-side vs. tail-side population of Pd nanoparticles on $CdS_{0.4}Se_{0.6}$ nanorods.

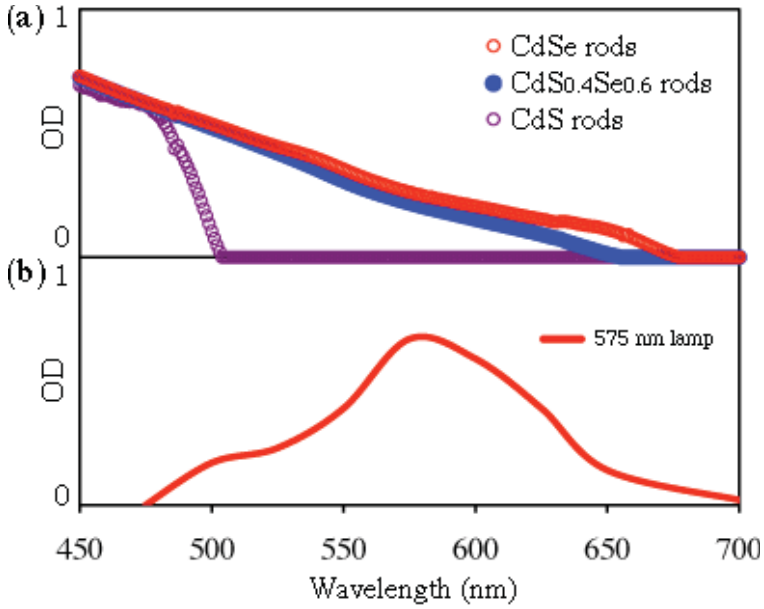

Figure 7. (a) Absorption spectra of colloidal CdS, $CdS_{0.4}Se_{0.6}$, and CdSe nanorods (recorded in toluene with quartz cuvettes), and (b) irradiance spectrum of 575 nm lamp (all spectra were arbitrarily normalized to a maximum optical density OD = 1).

These observations are relevant and somewhat resemble prior reports on metal (Au, Pd) photo deposition on CdSe/CdS seeded nanorods where metal particles grow either close to the CdSe seed[16,29] or at the CdS-tips.[44] However, to the best of our knowledge, this manuscript is the first to document that metal photo deposition behavior can be controlled and utilized to achieve the site selective or 'site-specific' photo deposition of metal particles on any specific segment of a heterostructure having an axial composition gradient. By switching the illumination energy to shorter or longer wavelengths while keeping all other experimental conditions constant (precursors, concentrations, temperature), the Pd particles

can be controllably and site selectively photo-deposited on either side of axially anisotropic $CdS_{0.4}Se_{0.6}$ nanorods (Figure 6c,e).

Based on the band edge position of pure CdSe (730 nm) and pure CdS (520 nm) phases (closer to 680 nm and 500 nm, respectively, as modeled by pure CdSe and pure CdS nanorods), [46] we can relate the differences in metal photo deposition locale to the optical properties of the individual $CdS_{0.4}Se_{0.6}$ nanorod segments (Figure 7). The CdSe-rich head directly absorbs light emitted by all three 350 nm, 420 nm, and 575 nm lamps, allowing Pd particles to deposit on the head surface when the nanorods are irradiated with any of these wavelengths (Figure 7). In contrast, the CdS-rich tail only absorbs light emitted by the 350 nm and 420 nm lamps, but not light emitted by the 575 nm lamp, allowing Pd particles to deposit on the tail surface with the 350 nm and 420 nm lamps, but not with the 575 nm lamp (Figure 7). The lower energy excitons produced with the 575 nm lamp appear to be localized on the head of the nanorods, and exciton trapping by surface defects must be rapid, given the strong effect the 575 nm lamp has in skewing the distribution of surface bound Pd particles toward the head of the nanorods. However, excitons appear able to travel relatively freely and uninterrupted across the whole length of the nanorods; we have observed Pd particles everywhere from the head tip to the tail tip of the nanorods with all the lamps, including the CdS-rich tail of the nanorods when using the 575 nm lamp (Figures 5c and 6a,b).

Among other factors that could affect metal deposition are the relative lamp intensities and relative nanorod absorption coefficients at each lamp wavelength. Lamp intensities determine the ‘power’ or availability of photons and are independent of lamp wavelengths. Relative absorption coefficients determine how many photons are absorbed at each wavelength. Using sixteen twelve-inch fluorescent lamps in each case, we measured the

power (P) inside the Rayonette® reactor as 136 W/m^2 (P_{350nm}), 16.6 W/m^2 (P_{420nm}), and 47.2 W/m^2 (P_{575nm}). Using the absorption spectrum of $CdS_{0.4}Se_{0.6}$ nanorods (Figure 7), we extract the following order of absorption coefficients: 5.4 (ε_{350nm}) > 3.5 (ε_{420nm}) > 1 (ε_{575nm}). Taking the products of lamp intensities and relative absorption coefficients, we obtain the following order: 16 ($P \cdot \varepsilon_{575nm}$) > 1.2 ($P \cdot \varepsilon_{420nm}$) ≈ 1 ($P \cdot \varepsilon_{350nm}$). Thus, light absorption and the efficiency of exciton generation with the 350 nm lamp may be higher than with the 420 nm or 575 nm lamps. However, we have conducted several photo deposition experiments and have not yet found a significant correlation between power and metal particle diameter or photo deposition locale/site selectivity. Further studies are under way to sort out the precise effect of irradiation power on metal photo deposition behavior.

Additionally, at individual particle level, relative absorption coefficients between different nanorod segments could play an important role. For example, both CdS-rich tail and CdSe-rich head segments absorb light emitted by 350 nm and 420 nm lamps with similar absorption coefficients.[10] This may be why the distribution of length fractions for Pd particles using the 350 nm and 420 nm lamps is relatively wide (Figure 6c). Finally, surface defects are likely to be important in determining the exact locale of metal deposition. The diameter of CdS-rich tail segments (5.6 ± 0.8 nm) is significantly thinner than the diameter of CdSe-rich segments (17.8 ± 2.4 nm). Thinner nanorods have larger surface-to-volume ratios as well as a sharper curvature and an increased surface energy.[8] Assuming that both segments are equally passivated, we can expect thin CdS-rich tail to contain a larger concentration of surface defects. This could explain why a larger fraction of Pd particles form on the CdS-rich segment when using 350 nm and 420 nm lamps, and why many Pd particles form at the tip of the CdS-rich tail where curvature is the sharpest.

Conclusions

In summary, we have studied site selective and site-specific synthesis of colloidal semiconductor-metal hybrid heterostructures using whole-flask illumination/lamp photo deposition methods. We have shown precise lamp wavelength and its irradiance profile are critical in controlling whether metal photo deposition occurs in solution *via* homogeneous nucleation or on the surface of a colloidal semiconductor *via* heterogeneous nucleation, leading to freestanding or surface-bound metal nanoparticles, respectively. Using a number of control and metal deposition experiments, we identified three fundamental pathways leading to metal nanoparticle formation. Two of these pathways, thermal- and direct photochemical-precursor decomposition, lead to homogeneous nucleation of metal nuclei anywhere in solution and result in formation of unbound freestanding metal nanoparticles. A third pathway, semiconductor-mediated photochemical seeding and reduction of the metal precursor, leads to heterogeneous nucleation of metal nuclei at the semiconductor surface and results in formation of surface-bound metal nanoparticles. We have used these observations to selectively deposit Pt and Pd particles on the surface of CdS nanorods and axially anisotropic $CdS_{0.4}Se_{0.6}$ nanorods as model systems. Furthermore, we have shown specific lamp irradiance profile is critical in controlling specific locale (site-specificity) and overall distribution of Pd nanoparticles deposited on axially anisotropic $CdS_{0.4}Se_{0.6}$ nanorods. We expect the ability to reliably and controllably prepare semiconductor-metal hybrid heterostructures by judicious selection of reaction conditions, in this case by careful selection of lamp wavelength and irradiation times, will have major impact on engineering and tailoring these materials to target specific optical, electronic, magnetic, and catalytic properties. Reliable syntheses will increase availability of these hybrid nanomaterials for

their fundamental study and application. We are presently studying the mechanism of metal deposition in more detail, and specifically the effect irradiation power/intensity may have on diameter and locale of resulting metal nanoparticles. We are also exploring the activity of the resulting hybrid materials in solar-to-chemical conversion of renewable feedstock as well as the deposition of other catalytically relevant and magnetically active metals on the surface of a variety of heterostructured nanoscale semiconductors.

Experimental Section

Materials. Cadmium oxide (99.998%) and sulfur (99.999%) were purchased from Alfa Aesar. Octadecylphosphonic acid (ODPA) was purchased from PCI Synthesis. Selenium (99.999%), trioctylphosphine oxide (TOPO) (99%) and triethylamine (≥99.5%) were purchased from Sigma-Aldrich. Trioctylphosphine (TOP) (97%), dimethyl(1,5-cyclooctadiene)platinum(II) ($CODPtMe_2$, 99%) and cis-dimethyl(N,N,N',N'-tetramethylenediamine)palladium(II) ($TMEDAPdMe_2$, 99%) were purchased from Strem. All chemicals were used as received unless specified otherwise. *Caution*: Appropriate personal protective equipment and engineering controls must be in place before the use of cadmium, a toxic heavy metal.

Photochemical experiments. Photochemical experiments were conducted in a fan-cooled Rayonette® photoreactor (Southern New England Ultraviolet Company, Branford, Connecticut) equipped with an air-cooling fan and a carousel unit. Between 2 and 16 (max) 12-inch side-on "fluorescent" lamps (Luzchem, Ottawa, Ontario) were used for each experiment.

Synthesis of colloidal CdS and CdSSe nanorods. *CdS nanorods.* CdS nanorods (154.1 ± 30.4 nm length, 5.6 ± 0.8 nm diameter) were prepared according to a reported literature

procedure.[45] The CdS nanorods were found to have a wurtzite crystal structure.[46] *CdSSe nanorods.* Axially anisotropic $CdS_{0.4}Se_{0.6}$ nanorods having a 'drumstick'-like morphology (59.3 ± 8.0 length, 17.8 ± 2.4 nm 'head' diameter, 5.6 ± 0.8 nm 'tail' diameter) were synthesized by a modified procedure recently reported by our group.[46] Briefly, CdO (105 mg, 0.81 mmol), TOPO (1.375 g, 3.56 mmol) and ODPA (535 mg, 0.94 mmol) were weighed onto a three-neck round bottom flask. The flask was fitted with a glass-coated magnetic stir bar, a condenser and a stainless steel thermocouple. The apparatus was sealed and brought onto an Schlenk line. Using a heating mantle, the mixture was heated to 100 °C and evacuated under vacuum for 15 min, then it was refilled with argon and heated to 320 °C to form a completely colorless solution. The solution was then allowed to cool to 120 °C and evacuated under vacuum for 15 min, then refilled with argon and heated back to 320 °C. When the temperature reached 300 °C, TOP (1.20 mL, 2.7 mmol) was injected into the flask. When the temperature reached 320 °C, a solution containing an air-free mixture of 2.25 M TOPS (0.90 mL, 2 mmol) and 2.25 M TOPSe (0.10 mL, 0.2 mmol) was rapidly injected, causing a gradual color change. Upon injection, the temperature was allowed to equilibrate at 315 °C and kept constant for a total reaction time of 85 minutes. The reaction mixture was then removed from the heating mantle and allowed to cool to room temperature. After dilution with toluene (5 mL), the nanorods were isolated by the addition of a 1:1 $^{v}/_{v}$ iso-propanol/nonanoic acid (24 mL) mixture, followed by centrifugation (5,000 rpm for 10 min). The $CdS_{0.4}Se_{0.6}$ nanorods were found to have a wurtzite crystal structure.[46]

Synthesis of CdS-Pt and CdS-Pd heterostructures. CdS nanorods were dissolved in toluene to give an optical density (OD) of 1.2 at 470 nm. A 2-mL volume of this solution was degassed, refilled with dry argon, and stored in the dark for 12h in a re-sealable Schlenk tube.

Under a dry atmosphere, $CODPtMe_2$ (28 mg, 0.08 mmol) for CdS-Pt, or cis-dimethyl(N,N,N',N'-tetramethylene-diamine)palladium(II) ($TMEDAPdMe_2$) (28 mg, 0.1 mmol) for CdS-Pd, was dissolved in anhydrous toluene (1 mL), mixed with triethylamine (0.5 mL, used as a terminal electron donor),[29] and added to the CdS nanorod solution *via* syringe. The deposition reaction was then carried out for 3h by one of two routes: (1) *Thermally* in the dark, in an oil bath pre-equilibrated at 80 °C for CdS-Pt, or in a room temperature (R.T.) water bath for CdS-Pd; or (2) *photochemically*, under illumination at room temperature (R.T.) (21 °C-24 °C) in a fan-cooled Rayonet® photoreactor containing a set of 16 side-on fluorescent lamps (350 nm or 420 nm, see below) (total intensities: 136 W/m^2 and 16.6 W/m^2, respectively). The non-volatile products were purified by precipitation with a 1:1 mixture of acetone and methanol (30 mL) and centrifugation (4200 rpm for 10 min). All products readily redisperse in toluene.

Synthesis of $CdS_{0.4}Se_{0.6}$-Pd heterostructures. Axially anisotropic $CdS_{0.4}Se_{0.6}$ nanorods[46] were dissolved in toluene to give an optical density (OD) of 1.3 at 630 nm. A 2.0 mL volume of this solution was degassed, refilled with dry argon, and stored in the dark for 12 h in a re-sealable Schlenk tube. Under a dry atmosphere, $(TMEDA)PdMe_2$ (30 mg, 0.1 mmol) was dissolved in anhydrous toluene (1 mL), mixed with triethylamine (0.5 mL, used as terminal electron donor),[45] and added to the $CdS_{1-x}Se_x$ nanorod solution *via* syringe. The deposition reaction was then carried out for 1 h or 3 h photochemically under illumination at room temperature (R.T.) (21 °C-24 °C) in a fan-cooled Rayonet® photoreactor containing a set of 16 side-on fluorescent lamps (350 nm, 420 nm or 575 nm, see below) (total intensities: 136 W/m^2, 16.6 W/m^2, and 47.2 W/m^2, respectively). The non-volatile products were purified

twice by precipitation with methanol (30 mL) and centrifugation (5,000 rpm for 10 min). All products could be readily redispersed in toluene.

Structural characterization. *X-Ray diffraction.* Powder X-ray diffraction (XRD) data were measured using Cu Kα radiation on a Scintag XDS-2000 diffractometer equipped with a theta-theta goniometer, a sealed-tube solid-state generator, and an air-cooled Kevex Psi Peltier silicon detector. The XRD samples were prepared by spreading solid nanocrystal samples onto a background-less quartz sample holder. *Transmission electron microscopy.* Transmission electron microscopy (TEM) was conducted using a FEI Technai G2 F20 Field Emission TEM, a scanning transmission electron microscope (STEM) operating at 200 kV. This instrument has a point-to-point resolution of less than 0.25 nm and a line-to-line resolution of less than 0.10 nm. TEM samples were prepared by placing 2-3 drops of dilute toluene solutions of the nanocrystals onto carbon coated copper grids. The elemental axial distribution and composition of the nanorods were characterized by energy dispersive spectroscopy (EDS) line scans in STEM mode, as well as by energy-filtered (EF) imaging spectroscopy (EF-TEM) using a Gatan Tritium GIF system. *Size and morphology analysis.* Particle dimensions were measured manually and/or with ImageJ. In all cases, measurements and statistics were obtained for at least 50-100 nanorods (CdS or $CdS_{0.4}Se_{0.6}$) and 50-300 metal particles (Pt, Pd). Uncertainties in all measurements are reported as the standard deviations.

Optical characterization. Absorption spectra were measured in 0.1 cm or 1 cm quartz cuvettes with a photodiode array Agilent 8453 UV-Vis spectrophotometer. The absorption of the solvent was recorded and subtracted from all spectra. The absorption coefficients (ε /

$L \cdot mol^{-1} \cdot cm^{-1}$) of organometallic precursors were measured according to Lambert-Beer's Law by carefully preparing and recording the absorbance of different solutions in toluene.

Acknowledgement

This research is supported by the U.S. Department of Energy, Office of Basic Energy Sciences, Division of Chemical Sciences, Geosciences, and Biosciences through the Ames Laboratory. The Ames Laboratory is operated for the U.S. Department of Energy by Iowa State University under Contract DE-AC02-07CH11358. The document number assigned to this thesis/dissertation is IS-T 3100. We thank Iowa State University (ISU), the U.S. Department of Energy Ames Laboratory Royalty Account, and the Institute for Physical Research and Technology (IPRT) for laboratory startup funds (J.V.), ISU Chemistry Department for Women in Chemistry Award (T.P.A.R.), Yaqiao Wu for helpful discussions, and Andreja Bakac, Aaron Sadow, John Verkade and Keith Woo for initial access to equipment.

References

[1] Costi, R.; Saunders, A. E.; Banin, U. *Angew. Chem. Int. Ed.* **2010**, *49*, 4878-4897.

[2] Cozzoli, P. D.; Pellegrino, T.; Manna, L. *Chem. Soc. Rev.* **2006**, *35*, 1195-1208.

[3] Vaneski, A.; Susha, A. S.; Rodríguez-Fernández, J.; Berr, M.; Jäckel, F.; Feldmann, J.; Rogach, A. L. *Adv. Funct. Mater.* **2011**, *21*, 1547-1556.

[4] Kamat, P. V. *J. Phys. Chem. C* **2007**, *111*, 2834-2860.

[5] Shi, W.; Sahoo, Y.; Zeng, H.; Ding, Y.; Swihart, M. T.; Prasad, P. N. *Adv. Mater.* **2006**, *18*, 1889-1894.

[6] Franklin, A. D.; Smith, J. T.; Sands, T.; Fisher, T. S.; Choi, K.-S.; Janes, D. B. *J. Phys. Chem. C* **2007**, *111*, 13756-13762.

[7] Zhong, D. K.; Cornuz, M.; Sivula, K.; Grätzel, M.; Gamelin, D. R. *Energy Environ. Sci.* **2011**, *4*, 1759-1764.

[8] Smith, A. M.; Nie, S. *Acc. Chem. Res.* **2010**, *43*, 190-200.

[9] Talapin, D. V.; Lee, J.-S.; Kovalenko, M. V.; Shevchenko, E. V. *Chem. Rev.* **2010**, *110*, 389-458.

[10] Yu, W. W.; Qu, L.; Guo, W.; Peng, X. *Chem. Mater.* **2003**, *15*, 2854-2860; **2004**, *16*, 560-560.

[11] García-Santamaría, F.; Chen, Y. F.; Vela, J.; Schaller, R. D.; Hollingsworth, J. A.; Klimov, V. I. *Nano Lett.* **2009**, *9*, 3482-3488.

[12] Cademartiri, L.; Bertolotti, J.; Sapienza, R.; Wiersma, D. S.; von Freymann, G.; Ozin, G. A. *J. Phys. Chem. B* **2006**, *110*, 671-673.

[13] Nozik, A. J. *Chem. Phys. Lett.* **2008**, *457*, 3-11.

[14] Klimov, V. I. *J. Phys. Chem. B* **2006**, *110*, 16827-16845.

[15] Costi, R.; Saunders, A.; Elmalem, E.; Salant, A.; Banin, U. *Nano Lett.* **2008**, *8*, 637-641.

[16] Menagen, G.; Macdonald, J. E.; Shemesh, Y.; Popov, I.; Banin, U. *J. Am. Chem. Soc.* **2009**, *131*, 17406-17411.

[17] Carbone, L.; Jakab, A.; Khalavka, Y.; Sönnichsen, C. *Nano Lett.* **2009**, *9*, 3710-3714.

[18] Mokari, T.; Rothenburg, E.; Popov, I.; Costi, R.; Banin, U. *Science* **2004**, *304*, 1787-1790.

[19] Chakrabortty, S.; Yang, J. A.; Tan, Y. M.; Mishra, N.; Chan, Y. *Angew. Chem. Int. Ed.* **2010**, *49*, 2888-2892.

[20] Mokari, T.; Sztrum, C. G.; Salant, A.; Rabani. E.; Banin, U. *Nature Mater.* **2005**, *4*, 855-863.

[21] Maynadié, J.; Salant, A.; Falqui, A.; Respaud, M.; Shaviv, E.; Banin, U.; Soulantica, K.; Chaudret, B. *Angew. Chem. Int. Ed.* **2009**, *48*, 1814-1817.

[22] Deka, S.; Falque, A.; Bertono, G.; Sangregoria, C.; Poneti, G.; Morello, G.; De Giorgi, M.; Giannini, C.; Cingolani, R.; Manna, L.; Cozzoli, P. D. *J. Am. Chem. Soc.* **2009**, *131*, 12817-12828.

[23] Habas, S. E.; Yang, P.; Mokari, T. *J. Am. Chem. Soc.* **2008**, *130*, 3294-3295.

[24] Shemesh, Y.; Macdonald, J. E.; Menagen, G.; Banin, U. *Angew. Chem. Int. Ed.*

2011, *50*, 1185-1189.

[25] Pacholski, C.; Kornowski, A.; Weller, H. *Angew. Chem. Int. Ed.* **2004**, *543*, 4774-4777.

[26] Casavola, M.; Grillo, V.; Carlino, E.; Giannini, C.; Gozzo, F.; Pinel, E. F.; Garcia, M. A.; Manna, L.; Cingolani, R.; Cozzoli, P. D. *Nano Lett.* **2007**, *7*, 1386-1395.

[27] Saunders, A. E.; Popov, I.; Banin, U. *J. Phys. Chem. B* **2006**, *110*, 25421-25429.

[28] Elmalem, E.; Saunders, A. E.; Costi, R.; Salant, A.; Banin, U. *Adv. Mater.* **2008**, *20*, 4312-4317.

[29] Dukovic, G.; Merkle, M. G.; Nelson, J. H.; Hughes, S. M.; Alivisatos, A. P. *Adv. Mater.* **2008**, *20*, 4306-4311.

[30] He, S.; Zhang, H.; Delikanli, S.; Qin, Y.; Swihart, M. T.; Zeng, H. *J. Phys. Chem. C* **2009**, *113*, 87-90.

[31] Plante, I. J.; Habas, S. E.; Yuhas, B. D.; Gargus, D. J.; Mokari, T. *Chem. Mater.* **2009**, *21*, 3662-3667.

[32] Yang, J.; Elim, H. I.; Zhang, Q.; Lee, J. Y.; Ji, W. *Angew. Chem. Int. Ed.* **2011**, *50*, 1185-1189.

[33] Bao, N.; Shen, L.; Takata, T.; Domen, K. *Chem.Mater.* **2008**, *20*, 110-117.

[34] Bühler, N.; Meier, K.; Reber, J.-F. *J. Phys. Chem.* **1984**, *88*, 3261-3268.
[35] Reber, J.-F.; Rusek, M. *J. Phys. Chem.* **1986**, *90*, 824-834.

[36] Rufus, I. B.; Viswanathan, B.; Ramakrishnan, V.; Kuriacose, J.C. *J. Photochem. Photobiol. A* **1995**, *91*, 63-66.

[37] Uchihara, T.; Abe, H.; Matsumura, M.; Tsobumura, H. *Bull. Chem. Soc. Jap.* **1989**, *62*, 1042-1046.

[38] Furlong, D.N.; Grieser, F.; Hayes, D.; Hayes, R.; Sasse, W.; Wells, D. *J. Phys. Chem.* **1986**, *90*, 2388-2396.

[39] Park, H.; Choi, W.; Hoffman, M.R. *J. Mater. Chem.* **2008**, *18*, 2379-2385.

[40] Jang, J. S.; Choi, S. H.; Kim, H. G.; Lee, J. S. *J. Phys. Chem. C* **2008**, *112*, 17200-17205.

[41] Ivanov, S. A.; Piryatinski, A.; Nanda, J.; Tretiak, S.; Zavadil, K. R.; Wallace, W. O.; Werder, D.; Klimov, V. I. *J. Amer. Chem. Soc.* **2007**, *129*, 11708-11719.

[42] Gross, D.; Susha, A. S.; Klar, T. A.; Da Como, E.; Rogach, A. L.; Feldmann, J. *Nano Lett.* **2008**, *8*, 1482-1485.

[43] Menagen, G.; Mocatta, D.; Salant, A.; Popov, I.; Dorfs, D.; Banin, U. *Chem. Mater.* **2008**, *20*, 6900-6902.

[44] Li, X.; Lian, J.; Lin, M.; Chan, Y. *J. Am. Chem. Soc.* **2011**, *133*, 672-675.

[45] Robinson, R. D.; Sadtler, B.; Demchenko, D. O. Erdonmez, C. K.; Wang, L.-W.; Alivisatos, P. *Science* **2007**, *317*, 355-358.

[46] Ruberu, T. P. A.; Vela, J. *ACS Nano* **2011**, *5*, in press.

[47] Chan, S. C.; Barteau, M. A. *Langmuir* **2005**, *21*, 5588-5595.

[48] Of the 20% unbound Pt particles observed, ca. 5% Pt particles are formed thermally at R.T. as observed with the 420 nm lamp (Table 1, entries 2-3).

[49] Sakamoto, M.; Fujistuka, M.; Majima, T. *J. Photochem. Photobio. C: Photochem. Rev.* **2009**, *10*, 33-56.

[50] Luo, X.; Imae, T. *J. Mater. Chem.* **2007**, *17*, 567-571.

CHAPTER 5

SELECTIVE ALCOHOL DEHYDROGENATION AND HYDROGENOLYSIS WITH SEMICONDUCTOR-METAL PHOTOCATALYST: TOWARD SOLAR-TO-CHEMICAL CONVERSION OF BIOMASS-RELEVENT SUBSTRATES

Reprinted with permission from *J. Phys. Chem. Lett.* **2012**, *3*, 2798.

T. Purnima A. Ruberu, Nicholas C. Nelson, Igor I. Slowing, Javier Vela

Abstract

Photocatalytic conversion of biomass is a potentially transformative concept in renewable energy. Dehydrogenation and hydrogenolysis of biomass-derived alcohols can produce renewable fuels such as H_2 and hydrocarbons, respectively. We have successfully used semiconductor-metal heterostructures for sunlight-driven dehydrogenation and hydrogenolysis of benzyl alcohol. The heterostructure composition dictates activity, product distribution and turnovers. A few metal (M = Pt, Pd) islands on the semiconductor (SC) surface significantly enhance activity and selectivity, and also greatly stabilize the SC against photo-induced etching and degradation. Under selected conditions, CdS-Pt favors dehydrogenation (H_2) over hydrogenolysis (toluene) 8:1, whereas $CdS_{0.4}Se_{0.6}$-Pd favors hydrogenolysis over dehydrogenation 3:1. Photochemically generated, surface-adsorbed hydrogen is useful in tandem catalysis, for example via transfer hydrogenation. We expect this work will lead to new paradigms for sunlight-driven conversions of biomass-relevant substrates.

Introduction

Solar-to-chemical energy conversion of biomass is a potentially transformative concept in renewable energy. Photocatalytic water splitting has been studied for many years. Without stoichiometric or "sacrificial" agents, known photocatalysts split water to molecular hydrogen, H_2, and oxygen, O_2, under visible light with up to 6-7% quantum yield (QY) ($^1/_2H_2$ per photon).[1-5] Biomass, an overlooked photocatalysis target, is an abundant source of alcohols in the form of carbohydrates and polyols such as cellulose, starch and glycerol.[6,7] Photocatalytic dehydrogenation[8-13] and hydrogenolysis of biomass-derived alcohols can produce renewable fuels such as H_2 or hydrocarbons, respectively.[14,15] Like water splitting, these reactions are endergonic ($\Delta G_{RT}>0$); but unlike water splitting, they require much less energy (Scheme 1). Using sunlight to achieve these transformations can revolutionize the field of H_2 [16, 17] and hydrocarbon[18,19] fuel production and biomass conversion.[20,21]

Semiconductor-metal (SC-M) heterostructures are ideal photocatalytic materials; [22-26] they become redox-active upon illumination and remain redox-active after dark storage for several hours.[27] The semiconductor strongly absorbs light and the metal collects photogenerated charges. Tuning heterostructure spatial composition can impact the ability to engineer and direct energy flows at the nanoscale.[28] We recently demonstrated certain synthetic conditions allow deposition of M (Pt, Pd) nanoparticles on $CdS_{1-x}Se_x$ ($0<1<x$) nanorods with high selectivity.[29] M photodeposition occurs on specific segments of compositionally graded $CdS_{0.4}Se_{0.6}$ nanorods due to the band gap differential between CdSe-rich and CdS-rich segments.[30] Here, we demonstrate photocatalytic alcohol dehydrogenation and hydrogenolysis driven by visible sunlight using such heterostructures.

Scheme 1. Hydrogen photoproduction from water vs. biomass

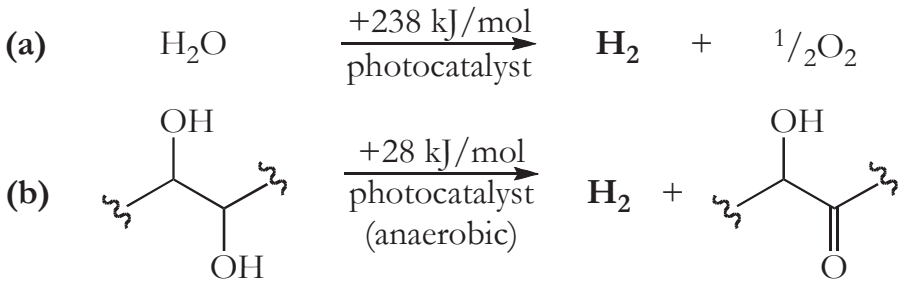

Scheme 2. Alcohol dehydrogenation vs. hydrogenolysis

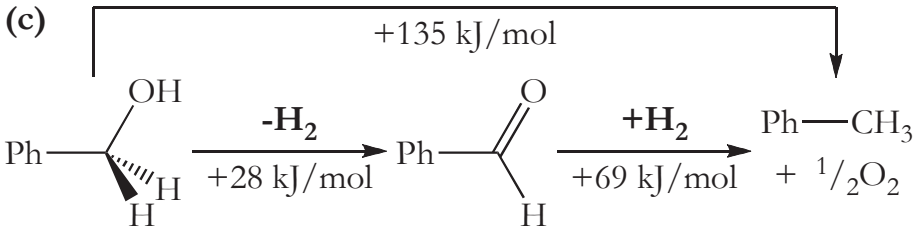

Results and Discussions

Under a dry nitrogen atmosphere, semiconductor-metal photocatalysts were dissolved in anhydrous deuterated benzene (C_6D_6) to give optical densities (OD) of 0.4 at 470 nm for CdS-M or 0.2 for 690 nm for $CdS_{0.4}Se_{0.6}$-M (M = Pt, Pd). Stock solutions were kept in the dark for at least >12 h prior to catalytic experiments. In the dark, photocatalyst stock solution (0.1 mL), benzyl alcohol ($PhCH_2OH$) (40 mg, 370 μmol), and C_6D_6 (0.4 mL) were added to an oven-dried NMR tube. The tube was capped with a septum and sealed with Parafilm®. The mixture was exposed directly to sunlight or lamp illumination in a Rayonette photoreactor and analyzed by NMR and GC.

Under direct sunlight illumination, $PhCH_2OH$ was converted to benzaldehyde, PhCHO, as observed by ^{1}H NMR and GC-MS. Headspace analysis by GC using a thermal conductivity detector (TCD) showed formation of H_2. H_2 was also detected at high conversion from its resonance at δ 4.47 ppm in ^{1}H NMR.[31] Interestingly, ^{1}H NMR and GC-

MS also showed formation of toluene, $PhCH_3$, as a byproduct.[32,33] Relative PhCHO, H_2 and $PhCH_3$ amounts produced are strongly affected by the structure and composition of the SC-M photocatalyst (Table 1, Figure 1). After 2 days under sunlight, the main product was H_2 when CdS-Pt was used, and toluene when CdS-Pd was used (entries 1-2, Table 1, Figure 2). In contrast, little selectivity was observed with unmodified CdS nanorods (entry 4, Table 1). Reactions run under sunlight with $CdS_{0.4}Se_{0.6}$-Pt and $CdS_{0.4}Se_{0.6}$-Pd favored toluene, although they were less selective than CdS-Pd (entries 7-8, Table 1, Figure 2). No H_2 and negligible amounts of PhCHO and $PhCH_3$ were detected for over a week when reactions were carried out in the presence of SC-free, unbound Pt or Pd nanoparticles (Figure 1b).[29]

Table 1. Photocatalytic Dehydrogenation and Hydrogenolysis of $PhCH_2OH$ with SC and SC-M Photocatalysts.[a]

	Photocatalyst (M np/SC rod)[b]	Conds.	Time	PhCHO TON[c]	$PhCH_3$ TON[c]	H_2 TON[c]
1	CdS-Pt (2.0±1.1)[b]	Sun	2 days	596	130	522
				$12 \cdot h^{-1}$	$3 \cdot h^{-1}$	$11 \cdot h^{-1}$
2	CdS-Pd (1.6±0.8)[b]	Sun	2 days	102	328	0
				$2 \cdot h^{-1}$	$7 \cdot h^{-1}$	0
3	CdS-Pd (2.9±0.9)[b]	Sun	2 days	24	0.5	0
				$0.5 \cdot h^{-1}$	$0.01 \cdot h^{-1}$	0
4	CdS	Sun	2 days	155	164	111
				$3 \cdot h^{-1}$	$3 \cdot h^{-1}$	$2 \cdot h^{-1}$
5	CdS-Pt (2.0±1.1)[b]	350 nm	3 h	696	114	909
				$232 \cdot h^{-1}$	$38 \cdot h^{-1}$	$303 \cdot h^{-1}$
6	CdS-Pd (1.6±0.8)[b]	350 nm	3 h	135	255	255
				$45 \cdot h^{-1}$	$85 \cdot h^{-1}$	$85 \cdot h^{-1}$

Table 1 continued

7	$CdS_{0.4}Se_{0.6}$-Pt (2.5±0.8)[b]	Sun	2 days	96	3840	2832
				$2 \cdot h^{-1}$	$80 \cdot h^{-1}$	$59 \cdot h^{-1}$
8	$CdS_{0.4}Se_{0.6}$-Pd (1.4±0.8)[b]	Sun	2 days	48	5232	2832
				$1 \cdot h^{-1}$	$109 \cdot h^{-1}$	$59 \cdot h^{-1}$
9	$CdS_{0.4}Se_{0.6}$-Pt (2.5±0.8)[b]	575 nm	6 h	54	4338	3228
				$9 \cdot h^{-1}$	$723 \cdot h^{-1}$	$538 \cdot h^{-1}$
10	$CdS_{0.4}Se_{0.6}$-Pd (1.4±0.8)[b]	575 nm	6 h	36	10212	3228
				$6 \cdot h^{-1}$	$1702 \cdot h^{-1}$	$538 \cdot h^{-1}$

[a]$PhCH_2OH$ (40 mg, 370 μmol), C_6D_6 (0.5 mL), 24°C, anaerobic (air-free) conditions (3.3×10^{-9} mol CdS-M 2.9×10^{-9} mol $CdS_{0.4}Se_{0.6}$-M). [b]Metal particles per rod. [c]Turnover numbers (TON) (±8%) and TON/h are two run averages; Products were quantified using NMR (organics) and GC (organics and H_2).

Photocatalytic experiments were also carried out inside a fan-cooled Rayonette® photoreactor. Unlike the intermittent and cyclical nature of direct sunlight illumination, lamp irradiation provides a constant stream of photons for a more controlled photocatalytic environment. Photoreactor also better mimic the higher intensity conditions more likely to be used in some industrial photocatalysis technologies, for example those using solar concentrators. Measured intensities in a 16×12-in lamp reactor were 136 W/m^2 for 350 nm lamps and 43.6 W/m^2 for 575 nm lamps. This is 5-to-2 times stronger than the daily zenith (max.) intensity of 26 W/m^2 recorded under direct sunlight in Ames, IA (Jan.-Jul., 42°2'5"N Lat., 294 m altitude).

Photocatalytic experiments run under 350 nm lamp illuminations for CdS-M or under 575 nm lamp illumination for $CdS_{0.4}Se_{0.6}$-M (M = Pt, Pd) greatly increased the rates of product formation by a factor of 10-to-15 (entries 7-8, 9-10, Table 1). In the case of CdS-Pd,

switching from sunlight to 350 nm lamp illumination also altered relative distribution of PhCHO, $PhCH_3$ and H_2 products from 1:3:0 to 1:2:2, respectively (entries 2 vs. 6, Table 1, Figure 2). We believe this is a consequence of the interplay between the rates of charge transfer (redox) involved in the two photocatalytic reactions and the rate of exciton generation and trapping by different M "islands" on the SC surface. In the case of $CdS_{0.4}Se_{0.6}$-M (M = Pt, Pd) heterostructures, the main product remained $PhCH_3$ regardless of M or light source used (entries 6-10, Table 1).

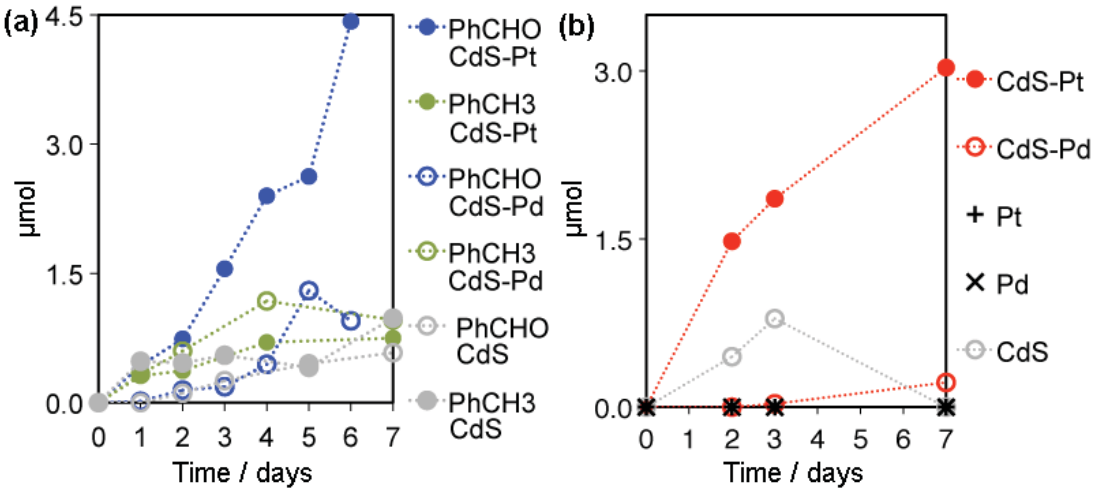

Figure 1. Photo-production of (a) PhCHO, $PhCH_3$, and (b) H_2 from $PhCH_2OH$ with CdS-M catalysts under sunlight illumination (air-free, 3.3×10^{-9} mol SC-M, 0.5 mL C_6D_6, 24°C).

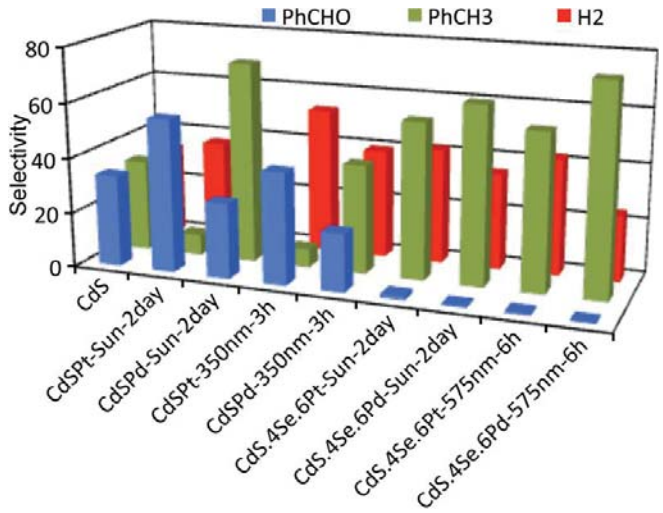

Figure 2. Product selectivity (normalized to 100% products) of SC and SC-M photocatalysts for PhCHO, $PhCH_3$, and H_2 under different photochemical conditions (air-free, 3.3×10^{-9} mol SC-M, 0.5 mL C_6D_6, 24°C).

Critically, SC-M heterostructures are much more stable photocatalysts compared to unmodified SC nanorods. Figure 3 shows UV/Vis absorption and TEM data obtained before and after photocatalytic runs with CdS-Pt and CdS. Under continuous illumination, CdS-Pt heterostructure solutions retained their activity and color for several days; in contrast, CdS nanorod solutions became inactive, their color bleached, and completely faded away within a few days (Figure 3a-b). This is evident in the sharp drop in H_2 photo-production for pure CdS after 3 days in Figure 1b. Transmission electron microscopy (TEM) revealed CdS-Pt heterostructures roughly retained their overall morphology and composition (Figure 3c, e), while CdS nanorods quickly dissolved and etched away during the same period (Figure 3d,f). Thus, the presence of surface-bound M (Pt, Pd) "cocatalyst" particles not only enhances photocatalytic activity and determines product selectivity, but it also greatly stabilizes SC (CdS) nanorods against photo-induced etching and degradation. We believe this behavior is due to major electronic structure differences between SC-M and SC photocatalysts. UV-Vis absorption shows the fine structure of CdS disappears upon Pt loading (Figure 3a vs. 3b, red traces). This behavior is similar to chemically and electrochemically-induced 1*S* peak "bleaching",[34,35] and is consistent with a significant degree of electron transfer between Pt and CdS.[36,37,38] II-VI SC photoetching under photocatalytic conditions is thought to stem from anion (S^{2-}) oxidation. Therefore the observation that CdS-Pt is less susceptible to photoetching compared to CdS could in principle be explained by electron injection from the Pt islands into the conduction band of CdS, effectively creating an n-doped SC. However, more research is needed to confirm or refute this hypothesis. Other known SC photocatalyst stabilizers include sacrificial hole scavengers such as Na_2S/Na_2SO_3. These additives enhance

the population and lifetime of trapped electrons, resulting in faster H_2 evolution rates (from water).[39]

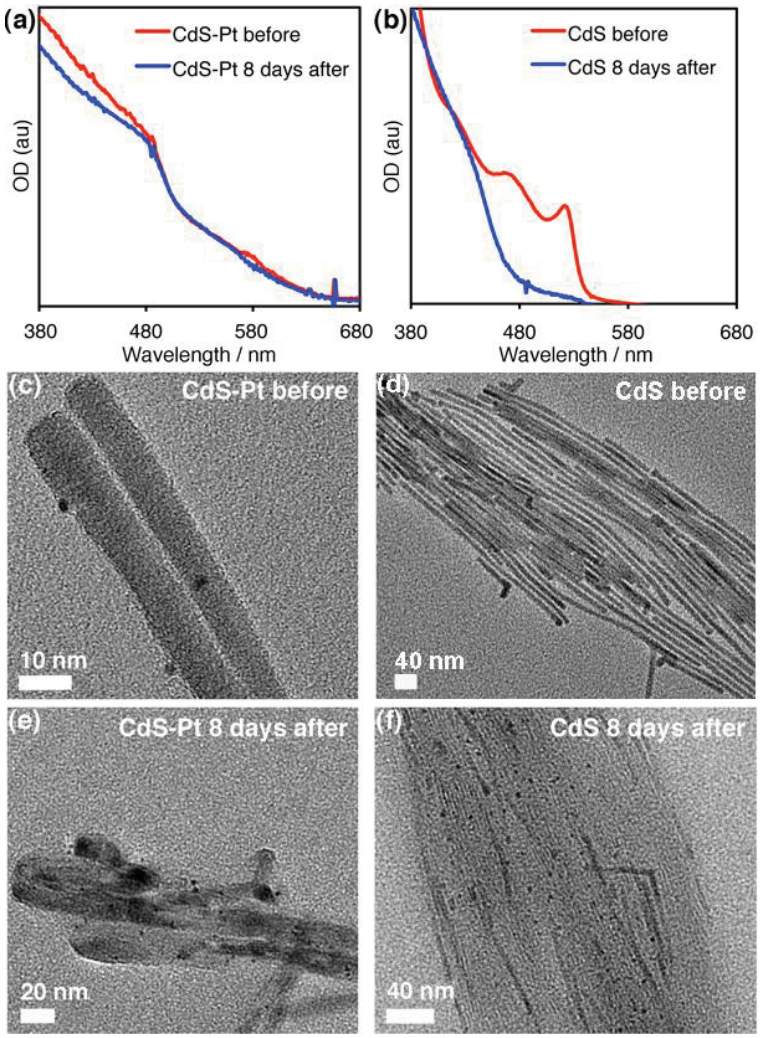

Figure 3. Monitoring stability of SC-M and SC photocatalysts by UV-Vis absorption (a,b) and TEM (c-f): CdS-Pt heterostructures (left) retain their color (a) and overall morphology (c,e); in contrast, CdS nanorods (right) get bleached (b) and photoetched (d,f).

The precise amount of M loading has a major effect on photocatalytic activity. Under direct sunlight illumination for 2 days, decreasing M loading from 2.9±1.5 to 1.6±0.8 Pd particles per CdS nanorod[29] increased the amounts of PhCHO and $PhCH_3$ produced by 4 and 660 times, respectively (a 1-3 order of magnitude enhancement!) (entries 2-3, Table 1 and

Figure 4). This agrees with prior literature observations for water photosplitting,[40-42] where excess metal cocatalyst loading is actually detrimental to photocatalytic activity.

As shown in Scheme 2c, our combined results strongly indicate the existence of two photocatalytic pathways starting from benzyl alcohol. One pathway favors alcohol dehydrogenation and produces benzaldehyde, PhCHO and molecular hydrogen, H_2; the other pathway favors alcohol hydrogenolysis and produces toluene, $PhCH_3$ and molecular oxygen, O_2. Both pathways are thermodynamically uphill but also much less energetically demanding compared to water photosplitting (Scheme 2c). Production of $PhCH_3$ (hydrogenolysis) is easier (requires less energy) starting from PhCHO (69 kcal/mol) than from $PhCH_2OH$ (135 kcal/mol) (Scheme 2c). Evidence to support a two-step dehydrogenation-hydrogenolysis pathway for toluene formation stems from mechanistic experiments. Using isotopically-labeled benzyl alcohol-α,α-D_2, $PhCD_2OH$ as a photocatalysis substrate leads to formation of deuterated benzaldehyde-D, PhCDO, as observed by ^2H (D) NMR. Also, heating $PhCH_3$ in presence of SC-M heterostructures and air (O_2) to 50°C in the dark for 8 h gave both $PhCH_2OH$ and PhCHO, which corresponds to the thermal reverse of hydrogenolysis and dehydrogenation reactions (Scheme 2c).[43] Additional reactions occur during certain conditions: For example, pinacol coupling products (PhCOCOPh) were observed by GC-MS and may account for the excess H_2 relative to PhCHO produced with $CdS_{0.4}Se_{0.6}$-M (entries 7-10, Table 1).

We explain the different selectivity between SC-Pt (favors H_2) and SC-Pd (favors $PhCH_3$) based on the known reactivity of Pt and Pd surfaces. Pd is known to strongly adsorb hydrogen atoms ("protons") and promote reduction reactions.[44] Thus, H_2 gas produced during dehydrogenation quickly adsorbs onto the Pd surface, forming Pd-H reduction sites

for the conversion of benzaldehyde (PhCHO) to toluene ($PhCH_3$). Our initial photocatalytic studies were conducted under anaerobic (air-free) conditions to avoid potential oxidation (combustion) of H_2 in the presence of O_2 from air (thermal oxidation to water is downhill: ΔG_{RT} = -210 kJ/mol, Scheme 1a).[15, 45-47] Photocatalytic runs under aerobic conditions, *i.e.* in presence of O_2, did not significantly change the relative amounts of PhCHO and $PhCH_3$ produced; however no H_2 was detected in those cases. This is consistent with SC-M heterostructures being active in reversible H_2 oxidation and water splitting. Additionally, we qualitatively observed much higher O_2 levels in hydrogenolysis (toluene-forming) photoreactions with CdS-Pd.

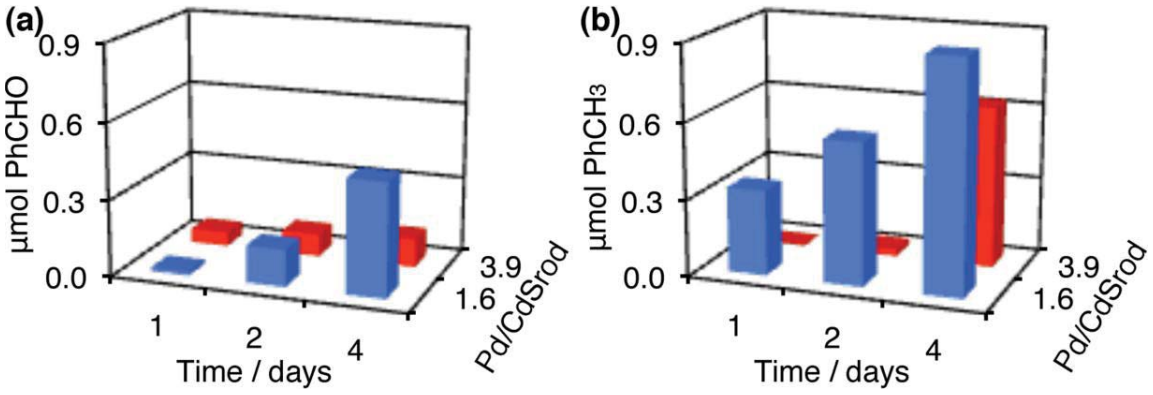

Figure 4. Effect of Pd loading on photocatalytic activity of CdS-Pd heterostructures under direct sunlight. Conditions: Anaerobic, 3.3×10^{-9} mol SC-M, 0.5 mL C_6D_6, 24°C.

An additional opportunity arising from the chemistry demonstrated here is to use H_2 formed upon alcohol dehydrogenation to perform other chemical transformations. We have successfully tested this idea by adding glyceraldehyde, $HOCH_2CH_2OHCHO$ (Scheme 3) to $PhCH_2OH$ during photocatalytic runs. The amount of PhCHO produced in this case was extremely high, with up to 18% $PhCH_2OH$ consumed when CdS-Pd was used. Interestingly, this transfer hydrogenation reaction does not proceed in the absence of light, strongly

suggesting that glyceraldehyde is reduced by photogenerated H_2 or Pd-hydride equivalents on the SC-Pd surface. This opens new avenues for the discovery and development of light-induced, tandem catalytic transfer dehydrogenation reactions.

Scheme 3. Photo-induced transfer hydrogenation

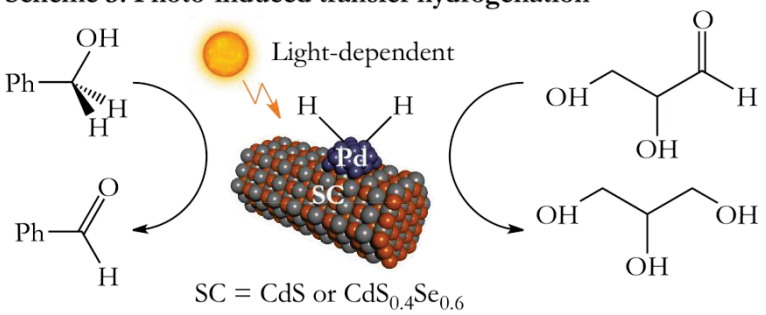

Conclusions

In summary, we have shown semiconductor-metal (SC-M) heterostructures are active catalysts for room temperature, photochemical dehydrogenation and hydrogenolysis of an alcohol. These reactions produce hydrogen and alkane, are only driven by light, and proceed with TONs upwards of 10,000. The precise photocatalyst structure and composition determine activity and selectivity. Under selected conditions, CdS-Pt favors dehydrogenation (H_2) over hydrogenolysis (toluene) 8:1, whereas $CdS_{0.4}Se_{0.6}$-Pd favors hydrogenolysis over dehydrogenation 3:1. Critically, a few metal (M = Pt, Pd) islands on the SC surface significantly enhance activity and selectivity, and greatly stabilize the SC against photo-degradation. This all-inorganic, additive free approach may make industrial-scale photocatalytic conversions possible. Photochemically generated, surface-adsorbed SC-Pd-H equivalents are useful synthetic intermediates in tandem catalysis via transfer hydrogenation. We are now investigating photocatalytic biomass conversions in flow. We expect this work

will lead to new paradigms for sunlight-driven conversions of biomass into useful renewable fuels and chemicals.

Experimental Section

Synthesis of CdS-Pt and CdS-Pd Hybrid Heterostructures. *CdS Nanorods.* CdS nanorods (154.1±30.4 nm length, 5.6±0.8 nm diameter) were prepared according to the method reported in chapter 2.The CdS nanorods were found to have a wurtzite (hexagonal) crystal structure. CdS nanorods were dissolved in toluene to give an optical density (OD) of 1.2 at 470 nm. A 2 mL volume of this solution was degassed, refilled with dry argon, and stored in the dark for 12 h in a resealable Schlenk tube. Under a dry atmosphere, dimethyl(1,5-cyclooctadiene)platinum(II) (CODPtMe_2) (28 mg, 0.08 mmol) for CdS-Pt or cis-dimethyl-(N,N,N′,N′-tetramethylene-diamine)palladium(II) (TMEDAPdMe_2) (28 mg, 0.1 mmol) for CdS-Pd was dissolved in anhydrous toluene (1 mL), mixed with triethylamine (0.5 mL, used as a terminal electron donor), and added to the CdS nanorod solution via syringe. The deposition reaction was then carried out for 1-3 h in the case of Pt deposition and 1-3 h in the case of Pd deposition by photochemically, under illumination at room temperature (21-24 °C) in a fan-cooled Rayonet photoreactor containing a set of 16 side-on 420 nm fluorescent lamps total intensities: 136 and 16.6 W/m2, respectively). Longer irradiation times lead to the deposition of more metal particles per nanorod. The nonvolatile products were purified by precipitation with a 1:1 mixture of acetone and methanol (30 mL) and centrifugation (4200 rpm for 10 min).

Synthesis of $CdS_{0.4}Se_{0.6}$-Pt and $CdS_{0.4}Se_{0.6}$-Pd Hybrid Heterostructures. Axially anisotropic $CdS_{0.4}Se_{0.6}$ nanorods having a “drumstick”-like morphology (59.3±8.0 length, 17.8±2.4 nm “head” diameter, 5.6±0.8 nm “tail” diameter) were synthesized by a modified

procedure recently reported in chapter 2. Briefly, CdO (105 mg, 0.81 mmol), TOPO (1.375 g, 3.56 mmol), and ODPA (535 mg, 0.94 mmol) were weighed onto a three-neck round-bottomed flask. The flask was fitted with a glass-coated magnetic stir bar, condenser, and stainless steel thermocouple. The apparatus was sealed and brought onto an Schlenk line. Using a heating mantle, the mixture was heated to 100 °C and evacuated under vacuum for 15 min, and then it was refilled with argon and heated to 320 °C to form a completely colorless solution. The solution was then allowed to cool to 120 °C and evacuated under vacuum for 15 min, and then refilled with argon and heated back to 320 °C. When the temperature reached 300 °C, TOP (1.20 mL, 2.7 mmol) was injected into the flask. When the temperature reached 320 °C, a solution containing an air-free mixture of 2.25 M TOPS (0.90 mL, 2 mmol) and 2.25M TOPSe (0.10 mL, 0.2 mmol) was rapidly injected, causing a gradual color change. Upon injection, the temperature was allowed to equilibrate at 315 °C and kept constant for a total reaction time of 85 min. The reaction mixture was then removed from the heating mantle and allowed to cool to room temperature. After dilution with toluene (5 mL), the nanorods were isolated by the addition of a 1:1 v/v iso-propanol/nonanoic acid (24 mL) mixture, followed by centrifugation (5000 rpm for 10 min). The $CdS_{0.4}Se_{0.6}$ nanorods were found to have a wurtzite crystal structure.

Axially anisotropic $CdS_{0.4}Se_{0.6}$ nanorods were dissolved in toluene to give an optical density (OD) of 1.3 at 630 nm. A 2.0 mL volume of this solution was degassed, refilled with dry argon, and stored in the dark for 12 h in a resealable Schlenk tube. Under a dry atmosphere, (TMEDA)$PdMe_2$ (30 mg, 0.1 mmol) was dissolved in anhydrous toluene (1 mL), mixed with triethylamine (0.5 mL, used as terminal electron donor), and added to the $CdS_{1-x}Se_x$ nanorod solution via syringe. The deposition reaction was then carried out for 1 h

for Pd and 3 h for Pt photochemically under illumination at room temperature (21-24 °C) in a fan-cooled Rayonet photoreactor containing a set of 16 side-on 420 nm fluorescent lamps. Longer irradiation times lead to the deposition of more metal particles per nanorod.[2] The nonvolatile products were purified twice by precipitation with methanol (30 mL) and centrifugation (5000 rpm for 10 min).

Photocatalytic experiments. For each catalytic run, to a clean oven-dried NMR tube inside the glove box benzyl alcohol (40 mg), CdS (3.3×10^{-9} mol), CdS-M (3.3×10^{-9} mol) or $CdS_{0.4}Se_{0.6}$-M (2.9×10^{-9} mol) and C_6D_6 (0.5 ml) were added. The NMR tube was sealed using a septum and sealed with Parafilm® to prevent air leakage. The NMR tube was placed under direct sunlight or kept inside a photoreactor to carry out the photocatalysis. After a certain time, a definite amount of gas from the headspace was withdrawn using a microliter air-tight syringe. Gas samples were analyzed using a GC with a thermal conductivity detector. Liquid fractions were analyzed using GC, GC-MS and ^{1}H NMR.

Acknowledgement

We thank Conoco Phillips (alcohol dehydrogenation) and the U.S. Department of Energy, Office of Basic Energy Sciences, Division of Chemical Sciences, Geosciences, and Biosciences through the Ames Laboratory (1D semiconductor photocatalysts) for support. Ames Laboratory is operated for the U.S. Department of Energy by Iowa State University (ISU) under Contract No. DE-AC02- 07CH11358. The document number assigned to this thesis/dissertation is IS-T 3100. We thank ISU, Ames Lab Royalty Account, and Institute for Physical Research and Technology (IPRT) for laboratory startup funds (J.V.), and Bob

Angelici, Edgar Lotero, and Scott McQueen for useful discussions. Dedicated to the enduring scientific legacy of Prof. Victor S.-Y. Lin (1966-2010).

References

[1] Maeda, K.; Teramura, K. *Nature* **2006**, *440*, 295-295.

[2] Maeda, K.; Domen, K. *J. Phys. Chem. Lett.* **2010***, 1,* 2655-2661.

[3] Reber, J. F.; Rusek, M. *J. Phys. Chem.* **1986**, *90*, 824-834.

[4] Harbour, J. R.; Wolkow, R.; Hair, M. L. *J. Phys. Chem.* **1981***, 85,* 4026-4029.

[5] Silva, C. G.; Juárez, R.; Marino, T.; Molinari, R.; García, H. *J. Am. Chem. Soc.* **2011**, *133*, 595-602.

[6] Corma, A.; Iborra, S.; Velty, A. *Chem. Rev.* **2007**, *107*, 2411-2502.

[7] Chheda, J. N.; Huber, G. W.; Dumesic, J. A. *Angew. Chem. Int. Ed.* **2007**, *46*, 7164-7183.

[8] Montini, T.; Gombac, V.; Sordelli, L.; Delgado, J. J.; Chen, X.; Adami, G.; Fornasiero, P. *ChemCatChem* **2011**, *3*, 574-577.

[9] Gombac, V.; Sordelli, L.; Montini, T.; Delgado, J. J.; Adamski, A.; Adami, G.; Cargnello, M.; Bernal, S.; Fornasiero, P. *J. Phys. Chem. A* **2010**, *114*, 3916-3925.

[10] Blount, M. C.; Buchholz, J. A. Falconer, J. L. *J. Catal.* **2001**, *197*, 303-314.

[11] Maijenburg, A. W.; Rodijk, E. J. B.; Maas, M. G.; Enculescu, M.; Blank, D. H. A.; Elshof, J. E. *Small* **2011**, *7*, 2709-2713.

[12] Su, F.; Mathew, S. C.; Mohlmann, L.; Antonietti, M.; Wang, X.; Blechert, S. *Angew. Chem. Int. Ed.* **2011**, *50*, 657-660.

[13] Ruther, T.; Bond, A. M.; Jackson, W. R. *Green Chem.* **2003**, *5*, 364-366.

[14] Navarro, R. M.; Sánchez-Sánchez, M. C.; Alvarez-Galván, M. C.; Del Valle, F.; Fierro, J. L. G. *Energy Environ. Sci.* **2009**, *2*, 35-54.

[15] Angelici, R. J. *ACS Catal.* **2011***, 1,* 772-776.

[16] Cortright, R. D.; Davda, R. R.; Dumesic, J. A. *Nature* **2002**, *418*, 964-967.

[17] Vispute, T. P.; Huber, G. W. *Green Chem.* **2009**, *11*, 1433-1445.

[18] Huber, G. W.; Chheda, J. N.; Barrett, C. J.; Dumesic, J. A. *Science* **2005**, *308*, 1446-1449.

[19] Taher, D.; Thibault, M. E.; Mondo, D. D.; Jennings, M. M.; Schlaf, M. *Chem. Eur. J.* **2009**, *15*, 10132-10143.

[20] Petrus, L.; Noordermeer, M. A. *Green Chem.* **2006**, *8*, 861-867.

[21] Johnson, T. C.; Morris, D. J.; Wills, M. *Chem. Soc. Rev.* **2010**, *39*, 81-88.

[22] Cozzoli, P. D.; Pellegrino, T.; Manna, L. *Chem. Soc. Rev.* **2006**, *35*, 1195-1208.

[23] Amirav, L.; Alivisatos, P. *J. Phys. Chem. Lett.* **2010**, *1*, 1051-1054.

[24] Shemesh, Y.; Macdonald, J. E.; Menegen, G.; Banin, U. *Angew. Chem. Int. Ed.* **2011**, *50*, 1185-1189.

[25] Bao, N.; Shen, L.; Takata, T.; Domen, K. *Chem. Mater.* **2008**, *20*, 110-117.

[26] Che, X.; Shen, S.; Guo, L.; Mao, S. S. *Chem. Rev.* **2010**, *110*, 6503-6570.

[27] Costi, R.; Saunders, A.; Elmalem, E.; Salant, A.; Banin, U. *Nano Lett.* **2008**, *8*, 637-641.

[28] Acharya, K. P.; Khnayzer, R. S.; O' Conner, T.; Diederich, G.; Kirsanova, M.; Klinkova, A.; Roth, D.; Kinder, E.; Imboden, M.; Zamkov, M. *Nano Lett.* **2011**, *11*, 2919-2926.

[29] Alemseghed, M. G.; Ruberu, T. P. A.; Vela, J. *Chem. Mater.* **2011**, *23*, 3571-3759.

[30] Ruberu, T. P. A.; Vela, J. *ACS Nano* **2011**, *5*, 5775-5784.

[31] Fulmer, G. R.; Miller, A. J. M.; Sherden, N. H.; Gottlieb, H. E.; Nudelman, A.; Stoltz, B. M.; Bercaw, J. E.; Goldberg, K. I. *Organometallics* **2010**, *29*, 2176-2179.

[32] Fang, W.; Chen, J.; Zhang, Q.; Deng, W.; Wang, Y. *Chem. Eur. J.* **2011**, *17*, 1247-1256.

[33] Keresszegi, C.; Ferry, D.; Mallat, T.; Baiker, A. *J. Phys. Chem. B* **2005**, *109*, 958-967.

[34] Shim, M.; Guyot-Sionnest, P. *Nature* **2000**, *407*, 981-983.

[35] Wang, C.; Shim, M.; Guyot-Sionnest, P. *Science* **2001**, *291*, 2390-2392.

[36] Shaviv, E.; Schubert, U.; Alves-Santos, M.; Goldoni, G.; Di Felice, R.; Vallée, F.; Del Fatti, N.; Banin, U.; Sönnichsen, C. *ACS Nano* **2011**, *5*, 4712-4719.

[37] Plante, I. J.-L.; Habas, S. E.; Yuhas, B. D.; Gargas, D. J.; Mokari, T. *Chem. Mater.* **2009**, *21,* 3662-3667.

[38] Kamat, P. V. *J. Phys. Chem. Lett.* **2012**, *3,* 3, 663-672.

[39] Frame, F. A.; Carroll, E. C.; Larsen, D. S.; Sarahan, M.; Browning, N. D.; Osterloh, E. *Chem. Commun.* **2008**, 2206-2208.

[40] Song, X.; Yan, H.; Wu, G.; Ma, G.; Wen, F.; Wang, L.; Li, C. *J. Am. Chem. Soc.* **2008**, *130*, 7176-7177.

[41] Hara, M.; Nunoshige. J.; Takata, T.; Kondo, J. K.; Domen, K. *Chem. Commun.* **2003**, *39*, 3000-3001.

[42] Shemesh, Y.; Macdonald, J. E.; Menegen, G.; Banin, U. *Angew. Chem. Int. Ed.* **2011**, *50*, 1185-1189.

[43] Han, M.; Zhang, H.; Du, Y.; Yang, P.; Deng, Z. *Reac. Kinet. Mech. Cat.* **2011**, *102*, 393-404.

[44] Doyle, A. M.; Shaikhutdinov, S. K.; Jackson, S. D.; Freund, H.-J. *Angew. Chem. Int. Ed.* **2003***, 42,* 5240-5243.

[45] Shimizu, K.; Sugino, K.; Sawabe, K.; Satsuma, A. *Chem. Eur. J.* **2009**, *15*, 2341-2351.

[46] Ye, X.; Johnson, M. D.; Diao, T.; Yates, M. H.; Stahl, S. S. *Green Chem.* **2010**, *12*, 1180-1186.

[47] Wang, D.; Villa, A.; Spontoni, P.; Su, D. S.; Prati, L. *Chem. Eur. J.* **2010**, *16*, 10007-10013.

CHAPTER 6

GENERAL CONCLUSION

In summary, we prepared axially anisotropic nanorods with a composition gradient using a single injection of a mixture of TOPS and TOPSe to cadmium precursor solution. The morphology and the exact composition of the nanorods depend on the ratio of S and Se precursor on the injection solution. Axially anisotropic nanorods with a thick head segment and a thin tail segment are obtained when the Se loading is between 5% and 10% of total chalcogenides. The aspect ratio of the nanorods decreases as Se loading increases and optical properties of the nanostructures are tunable with composition.

The absorption band edges of these nanostructures red shift with increasing Se loading. X-ray diffraction and elemental analyses show that the actual Se content in $CdS_{1-x}Se_x$ nanorods is consistently higher than synthetic Se loading. X-ray diffraction data, Vegard's plots, and high-resolution TEM studies confirm that axially anisotropic nanorods possess a graded-alloy structure. Elemental mapping by energy-dispersive spectroscopy and energy-filtered TEM showed the head region of anisotropic nanorods is rich with Se and the tail region is rich with S. Time-dependent evolution studies show that the formation of these nanorods starts with homogeneous nucleation and quick growth of a thick CdSe-rich head, followed by heterogeneous nucleation and slow growth of a CdS-rich thin tail. This anisotropic growth can be attributed to the stability of chalcogenide precursors. TOPSe is less stable and more reactive compared to TOPS.

Based on the observations of the aforementioned work, we studied the effect of phosphine-chalcogenide, R_3PE (E = S or Se) precursor chemistry on the morphology and composition of the nanorods. Computational (DFT), NMR (^{31}P and ^{77}Se), and high-

temperature crossover studies unambiguously confirmed a chemical bonding interaction between phosphorus and chalcogen atoms in all R_3PE precursors. These studies showed phosphinechalcogenide reactivity decreases in the order TPPE >DPPE > TBPE> TOPE > HPTE (E = Se < S). Structural and optical characterization of $CdS_{1-x}Se_x$ nanodots, synthesized by a single high-temperature injection of a R_3PS-R_3PSe mixture to cadmium oleate, reveals their elemental composition and degree of radial alloying depends on relative R_3PS and R_3PSe reactivity. Similarly, structural characterization of CdS, CdSe, and $CdS_{1-x}Se_x$ nanorods, synthesized by high-temperature injection of individual R_3PE or R_3PS-R_3PSe precursor mixtures to cadmium phosphonate, reveals their length-to-diameter (aspect) ratio and a degree of axial alloying (composition gradient) depends on R_3PE precursor reactivity.

After establishing reliable methods for synthesizing semiconductor nanorods, we tried depositing metal nanoparticles on their surface using photochemical methods. We have shown precise lamp wavelength and its irradiance profile are critical in controlling whether metal photo deposition occurs in solution via homogeneous nucleation or on the surface of a colloidal semiconductor via heterogeneous nucleation, leading to freestanding or surface-bound metal nanoparticles, respectively. Using a number of control and metal deposition experiments, we identified three fundamental pathways leading to metal nanoparticle formation. Two of these pathways, thermal and direct photochemical precursor decomposition, lead to homogeneous nucleation of metal nuclei anywhere in solution and result in formation of unbound freestanding metal nanoparticles. A third pathway, semiconductor-mediated photochemical seeding and reduction of the metal precursor, leads to heterogeneous nucleation of metal nuclei at the semiconductor surface and results in formation of surface-bound metal nanoparticles. We have used these observations to

selectively deposit Pt and Pd particles on the surface of CdS nanorods and axially anisotropic $CdS_{0.4}Se_{0.6}$ nanorods as model systems. Furthermore, we have shown specific lamp irradiance profile is critical in controlling specific locale (site-specificity) and overall distribution of Pd nanoparticles deposited on axially anisotropic $CdS_{0.4}Se_{0.6}$ nanorods.

Finally, we have shown that semiconductor-metal nano-heterostructures are active catalysts for room temperature, photochemical dehydrogenation and hydrogenolysis of benzyl alcohol as a model substrate. These reactions produce hydrogen and alkane, are only driven by light, and proceed with high turnover numbers upwards of 10,000 within a sealed system. The precise photocatalyst structure and composition is critical in determining activity and selectivity. Under select conditions, CdS-Pt favors dehydrogenation (H_2) over hydrogenolysis (toluene) 8:1, whereas $CdS_{0.4}Se_{0.6}$-Pd favors hydrogenolysis over dehydrogenation 3:1. Critically, the presence of a few metal (M = Pt, Pd) islands on the SC surface significantly enhances activity and selectivity, and also greatly stabilizes the SC against photo-induced etching and degradation. This all-inorganic, additive free approach may help in making industrial-scale photocatalytic conversions possible. Photochemically generated, surface-adsorbed SC-Pd-H equivalents are a useful synthetic intermediate in tandem catalysis, for example via transfer hydrogenation.